FACULTY OF ARTS AND PHILOSOPHY

Measuring the past: New methods in analysing ancient figurative 'art'.

From the Mediterranean, Cyprus and the Near East.

Vanessa Vandenbussche
Student number: 01604178

Supervisors: Prof. Dr. Joachim Bretschneider, Prof. Sorin Hermon

A dissertation submitted to Ghent University in partial fulfilment of the requirements for the degree of Master of Archaeology

Academic year: 2019 – 2020

GHENT UNIVERSITY

FACULTY OF ARTS AND PHILOSOPHY

Measuring the past: New methods in analysing ancient figurative 'art'.

From the Mediterranean, Cyprus and the Near East.

Vanessa Vandenbussche
Student number: 01604178

Supervisors: Prof. Dr. Joachim Bretschneider, Prof. Sorin Hermon

A dissertation submitted to Ghent University in partial fulfilment of the requirements for the degree of Master of Archaeology

Academic year: 2019 – 2020

GHENT UNIVERSITY

Preface and Acknowledgements

When studying archaeology for the last four years, I have learned that it is composed of different point of views. There is the excavation, where you unearth the aspects of 'ancient' human life (how did they live, what were their ideologies, what type of materials did they produced, what is their social status etc.). This is often interpolated to a more global perspective where the excavation site will be interpreted in terms of the events from the region (if this is possible). Then there is the literary study and other forms of documentation. These can either be to learn about the history, social, religious, political or economic aspects from a certain period or area or the paperwork that is necessary nowadays to conduct archaeological research. Then there is the scientifical assessment were the excavated artefacts or architecture will be analysed to gain more information about their function, manufacturing processes, revealing hardly visible details, reconstruct fragments or using geophysical processing techniques to evaluate terrains of their archaeological potentials. The latter part, with the exception of the geophysical surveys, is not highly represented except the basic ideas and their usefulness and applicability. This thesis is written to acquire information about the scientific techniques available to analyse figurative 'art' in the Mediterranean, Cyprus and the Near East.

This was only possible thanks to my promotor **Professor Joachim Bretschneider** of the University of Ghent who gave me the idea and trusted me to research this topic. I am greatly thankful for his support and guidance. I would also like to say my deepest gratitude and appreciation for the help and his valuable suggestions and comments of my co-promotor **Professor Sorin Hermon** of the Cyprus Institute. I would also like to say my gratitude to all the professors I came across for their encouragements throughout the years. I am also indebted to my family and friends, who have been there for me since the start and were able to endure me when I was stressed. Last but not least, I would also like to say thanks to those who have taken their time to read this, it has given the written words more value!

Table of Contents

Wordcount: 30844

List of Abbreviations and Acronyms

1D	One-dimensional
2D	Two-dimensional
2B-PLS	Two block partial least squares
3D	Three-dimensional
3DHTD	3D Hough Transform descriptor
AGMT3-D	Artifact geomorph Toolbox 3D
CCD	Charged-coupled device
CNN	Convolutional neural network
CVA	Canonical variation analysis
DFA	Discriminant function analysis
DFT	Discrete fourier transform
DMD	Discrete modal decomposition
EDM	Euclidian distance matrix
EDMA	Euclidian distance matrix analysis
EFA	Elliptic fourier analysis
EFD	Elliptical Fourier descriptor
ELAS	Efficient large-scale stereo matching
EM	Electromagnetic
EMPA	Electron microprobe analysis
EOF	Empirical orthogonal functions
FESA	Finite-element scaling analysis
FM	Form matrix
FPP	Fringe pattern profilometry
FORS	Fibre optics reflectance spectroscopy
FT	Fourier transform
FTIR	Fourier transform infrared spectroscopy
FTP	Fourier transform profilometry

GCP	Ground control points
GPA	Generalized procrustes analysis
GPR	Ground penetrating radar
GRF	Generalized resistant-fit
HOS	High order statistics
HSH	Hemispherical harmonics
ICP	Iterative closest point
IR	Infrared
IRR	Infrared reflectance
IRT	Infrared thermography
ISO	International Organisation of Standardization
LASER	Light Amplification and Stimulated Emission of Radiation
LS	Laser scanning
LSCM	Laser scanning confocal microscopy
MEMS	Micro-electromechanical system mirrors
MPT	Miniature projection technique
MRM	Morphological residual method
MVS	Multiview stereoscopie
NAA	Neutron activation analysis
OPA	Ordinary procrustes analysis
OSR	Optical surface roughness
PC	Principal component
PCA	Principal component analysis
PCT	Principal component thermography
PCOORD	principal coordinates analysis
PIXE	Proton induced X-ray emission
PTM	Polynomial texture mapping
PPT	Pulsed phase thermography
PSP	Phase-shift profilometry

Ra	Arrhythmic average
ReLU	Rectified linear activation function
Rq	Roughness
RTI	Reflectance transformation imaging
Rz	Average peak-to-valley profile roughness
S_0	Ground state
S_1	First singlet state
SEM	Scanning electron microscope
SfM	Structure from motion
SIFT	Scale-invariant feature Transform
SL	Structured light
SVD	Singular value decomposition
T_1	First triplet state
TPS	Thin-plate splines
TSR	Thermographic signal reconstruction
UV	Ultraviolet
UVf	Ultraviolet fluorescence
UVL	Ultraviolet induced visible luminescence
UVR	Ultraviolet reflectance
V-PTM	Virtual polynomial texture mapping
VIL	Visible induced luminescence
Vis	Visible
VIVL	Visible induced visible luminescence
VR	Virtual reality
XRD	X-ray diffraction
XRF	X-Ray Fluorescence

List of figures

List of tables

Abstract

English:

In this thesis an attempt has been made to demonstrate the relevance of a multidisciplinary study in the field of figurative art from the Mediterranean, Cyprus and Near East using new techniques with similar and different applications. Since many techniques are available, they are critically tested against a few parameters to clarify for which information a particular method can be used in relation to time, cost, efficiency and user-friendliness. Hypotheses regarding available information, repeated patterns, trade networks, manufacturing techniques, use of color and use of local or other sources can be answered. The various techniques their theory, advantages and disadvantages and field of application in archeology are described as a result of a literature study and case studies. It can be concluded that, despite the required knowledge necessary to understand them and "high" cost, these techniques offer a significant value when they are used in the same pipeline.

Key words: multidisciplinary study – figurative art – critical evaluation – scientifical techniques – Mediterranean, Cyprus and the Near East.

Nederlands:

In deze uiteenzetting is er gepoogd om de relevantie van een multidisciplinair onderzoek in functie van figuratieve kunst uit het Mediterraans en Cypriotisch gebied en in het Nabije Oosten aan te tonen door gebruik te maken van nieuwe technieken met gelijkaardige en verschillende toepassingen. Aangezien er veel technieken voorhanden zijn, worden ze kritisch getoetst aan enkele parameters om duidelijk te maken voor welke informatie een bepaalde methode gebruikt kan worden in relatie met tijd, het kostenplaatje, efficiëntie en gebruiksvriendelijkheid. Hypotheses met betrekking tot de beschikbare informatie, herhaalde patronen, handelsnetwerken, vervaardigingstechnieken, kleurgebruik en gebruik van lokaal of andere bronnen kunnen beantwoord worden. Door middel van een literatuur onderzoek en case studies worden de verschillende technieken hun theorie, voor -en nadelen en toepassingsgebied in de archeologie beschreven. Als conclusie kan er gesteld worden dat deze technieken ondanks hun vereiste kennis en 'hoge' kost een grote meerwaarde bieden, wanneer ze in eenzelfde pijplijn gebruikt worden.

Kernwoorden: multidisciplinair onderzoek – figuratieve kunst – kritische evaluatie – wetenschappelijke technieken – Mediterraans en Cypriotisch gebied en Nabije Oosten

I. Introduction

1. Benefits of a multidisciplinary approach

The aim of this thesis is to demonstrate in what manner new scientific methods can contribute to the study of figurative art from the Mediterranean, Cyprus and the Near East. The research question is a threefold and each part shall be explained in the following passages.

1.1. New scientific methods

Archaeological science, better known as **Archaeometry** became an important additional field in archaeology in the second half of the twentieth century. This resulted in several movements since the 1960s by the processual archaeology (new archaeology) and the 1980s by the post-processual archaeology (interpretive archaeology). Both movements underline respectively the theoretical and atheoretical aspects of Archaeometry. The latter state that a more objective position needs to be acquired and that the individual is driven by their own ideology. Here a bit of both movement their statements and understandings will be adopted to combine the best of both worlds.

Since Archaeometry consists of different fields, it might be too overwhelming to know what kind of analyse is the best for answering the research question. In general, Archaeometry can be divided into the following fields:

- Chemistry and physics: dating techniques (carbon, dendrochronology, thermoluminescence), petrographic and provenance studies (X-ray fluorescence (XRF), neutron activation analysis (NAA), X-ray diffraction (XRD)), archaeometallurgy, spectroscopic studies (absorption and emission spectroscopy, Raman spectroscopy, laser-induced breakdown spectroscopy);
- Biology: zooarchaeology, anthropology, palynology and paleoethnobotany;
- Mathematics: geometry, statistics;
- Environmental studies: Laser imaging detection and ranging, ground penetrating radar (GPR), electromagnetic induction, magnetometry and geology;
- Conservation.

To choose in the variety of available techniques it is necessary to start with a couple of simple questions: What type of material is the object made of?, How is it made (manufacturing process)?, What is it used for (religious, domestic, utility, decoration)? and When is it made?. For each of these questions, different methods can be adopted and might be used in a complementary way.

First, it is convenient to determine how in-depth the analysis is going to be, is only the macroscopic property important (studying the object *an sich*) and/or are the microscopic properties essential (studying the small details or the composition of the material). Then it is necessary to know the principles of the techniques, whether the processing time, the cost of the equipment and software and the quality of the images or data are manageable and efficient in comparison to one another. As previously said, it might be possible that multiple techniques need to be combined when the limitations of one cheaper technique can be accompanied with the advantages of a more complicated and higher cost technique and vice versa. The latter is the main goal of this thesis, to try to show how much information can be collected when several (possibly similar) techniques are used, in other words, multidisciplinary research through literature study.

To evaluate between the methods the following aspects will be addressed and be put in a summary table for easy access:

- The type of materials;
- The need for contact;
- The requirement of samples and scale or destructive character;
- The degree of difficulty in theoretical principle;
- The accuracy;
- The type of information given;
- The safety of the technique;
- The overall cost (software, equipment);
- The overall duration (data acquisition versus data processing);
- The accessibility of the software;
- The used apparatus;
- The complexity of the data processing;
- The ability of measuring complex shapes or objects;
- The degree of compatibility with other techniques.

To have a sort of clear structure the techniques are arranged in terms of the physical properties (figure 1): geometric, thermal, reflective (optical or non-optical) and transmissive properties. Since colour is widely used the techniques involving their examination will be mentioned as well.

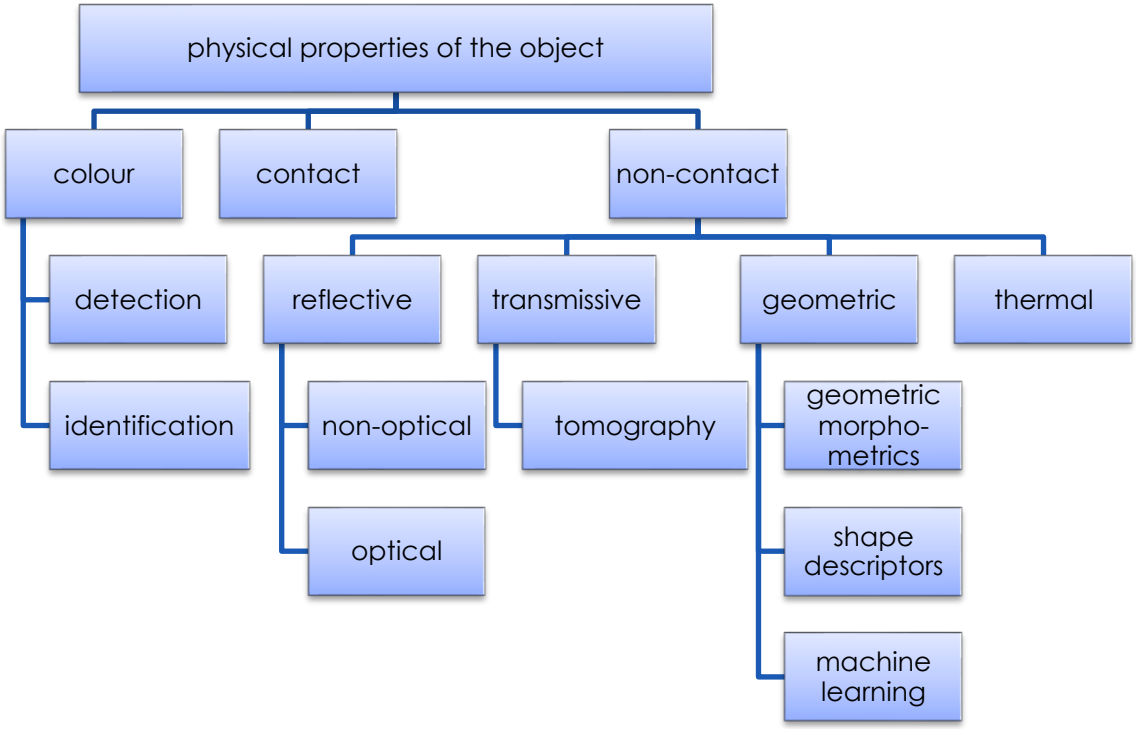

Figure 1: Taxonomy of the various techniques addressed in this thesis.

The term 'new' is more problematic to define since most of the time the theoretical framework already existed in the 20th century and some even in the 19th century and they were used in other research fields beside archaeology. Here the techniques which have been used since approximately 2015 are considered new, especially when it has not been widely used for figurative art or in the geographical context. When there is a new software developed and it seems that it has large applicability for figurative art it is included.

With this in mind, a lot of techniques are not going to be included since they are not considered new, but are frequently used in the study of figurative art. These are often chemical techniques used to define the composition of the material and determine its provenance. These include isotope analysis, optical microscopy, XRD, XRF, proton-induced X-ray emission (PIXE), voltammetry, scanning electron microscopy (SEM), electron microprobe analysis (EMPA), etc. By studying the provenance interesting aspects about the economics, politics and trade networks emerge and can tell something about the ideology and role of the site. Metal fragments are highly influenced by the atmosphere and are often corroded. Similar techniques can be used to determine the type of corrosion and patina and some techniques makes it possible to try and look beneath this layer. Some interesting research for the reader:

- D. Attanasio et al. (2020, 1): discovering of the provenance of white marble and black stone of Göktepe and comparison with the already existing data.
- F. Antonelli, F. Colivicchi and L. Lazzarini (2017, 9-10): Analysing seven Hellenistic white marble funerary stelae from Naples are examined to learn more about its provenance and the role of these Hellenistic style in perspective of the status of Naples.
- F. Fulminante and M. Unavane (2020, 7-9): 44 Archaic anthropomorphic figurines from Umbrian and Latin votive deposits are analysed to determine the metal composition. Both stylistic and metallurgical aspects are considered when discussing their role in a broader context to identify possible shared practices.
- A. Perea, P. Gutiérrez-Naira and A. Climent-Font (2018, 3; 13-14): A golden funerary belt from the Early Hellenistic period is analysed to discover its provenance. It shows various anthropomorphic and zoomorphic iconography such a Ram's head, palmette, the face of a man (presumably Alexander the Great) and a woman and a funerary libation scene. Again stylistic and metallurgical aspects are used. They point the direction towards either Babylon or Afghanistan.

1.2. Ancient figurative art

The second part of the research question revolves around ancient figurative art. The first thoughts which come to mind when thinking of ancient figurative art are not so different when looking at modern figurative art. The meaning of the word figurative links the real world with the constructed body, but this can also be done with an abstracted view, when only geometric shapes are used or when there is a different vision of the real world due to cultural influences.

In this perspective, almost everything can be seen as figurative art, but with the cultures and geographical context in mind the following cases are seen as figurative art:

- Figurines: humans, anthropomorphic representations, deities or animals;
- Statues or sculptures;
- Relief scenes or steles: low-, mid-, sunk-, or high relief;
- Seals;
- Pictorial elements;
- Frescoes and wall paintings.

When addressing all the techniques and their applicability in studying figurative art it can be observed that a certain type of figurative art or type of material is underrepresented in such investigations.

1.3. Mediterranean, Cyprus and the Near East

The last part of the research question involves the geographic context. The choice of this large area is firstly based on my own interest and secondly based on their diversity in figurative art.

Each of these regions has their own specialisation and availability of resources when looking at the materials used for their art, but similarities exist: bronze and marble in the Mediterranean, limestone in Cyprus and clay or terracotta in the Near East.

Other types of materials are:

- Organic material: wood, bone, clay, amber;
- Processed material: glass, metal (bronze);
- Minerals: marble, alabaster, limestone, sandstone;
- (semi-) precious stone: gold, lapis lazuli, carnelian.

When studying the type of art and used material, certain elements may be recurrent in the Mediterranean, Cyprus and the Near East. This can be due to trade routes or similar vision or even coincidence. By analyzing the *chaîne d'opératoire* and extrapolate the findings, trends might appear. Precautions are always necessary for such interpretations.

2. The structure

In section 3 of this chapter, some basic principles will be explained which might help to understand the principles of the analytical techniques. This is because most of them have a similar central fundamental.

In chapters II to V the different techniques used to measure the physical properties of the object will be discussed. For each of them, the theoretical principle, advantages and limitations and some case studies to address its use in archaeology will be given.

Chapter VI revolves around the detection and identification of the polychromy present on the figurative art. As well as with the previous techniques shall the theoretical principle, advantages and limitations and some small case studies be given.

Chapter VII deals with the results. Here it will be made clear that depending on the research question, certain techniques can be combined. This evaluation will be done on three levels: based on the techniques their applicability, based on the type of figurative art and based on the geographical context. This evaluation makes it possible to highlight underrepresented studies.

Chapter VIII forms the conclusion of this thesis.

3. Basic principles

Since there are several analytical techniques, where each of them offers a set of advantages and limitations, the same material or object can be studied by a various range of them functioning at a specific energy, working with a specific resolution, limits of detection, sensitivity, accuracy and spatial scale. To choose between them, it is necessary to have a broad understanding of the available techniques and their theoretical background as well. Therefore, some basic principles are given.

3.1. The electromagnetic spectrum

The electromagnetic (EM) spectrum (figure 2) shows the range of lights expressed in wavelength, energy or frequencies from gamma rays to radio waves. In the light of this paper the following spectral ranges are commonly used:

- Infrared (IR) radiation: 1 mm – 750 nm;
- Visible light (Vis): 750 nm (red) – 350 nm (purple);
- Ultraviolet (UV) radiation: 350 nm – 10 nm;
- X-ray: 10 nm – 10 pm.

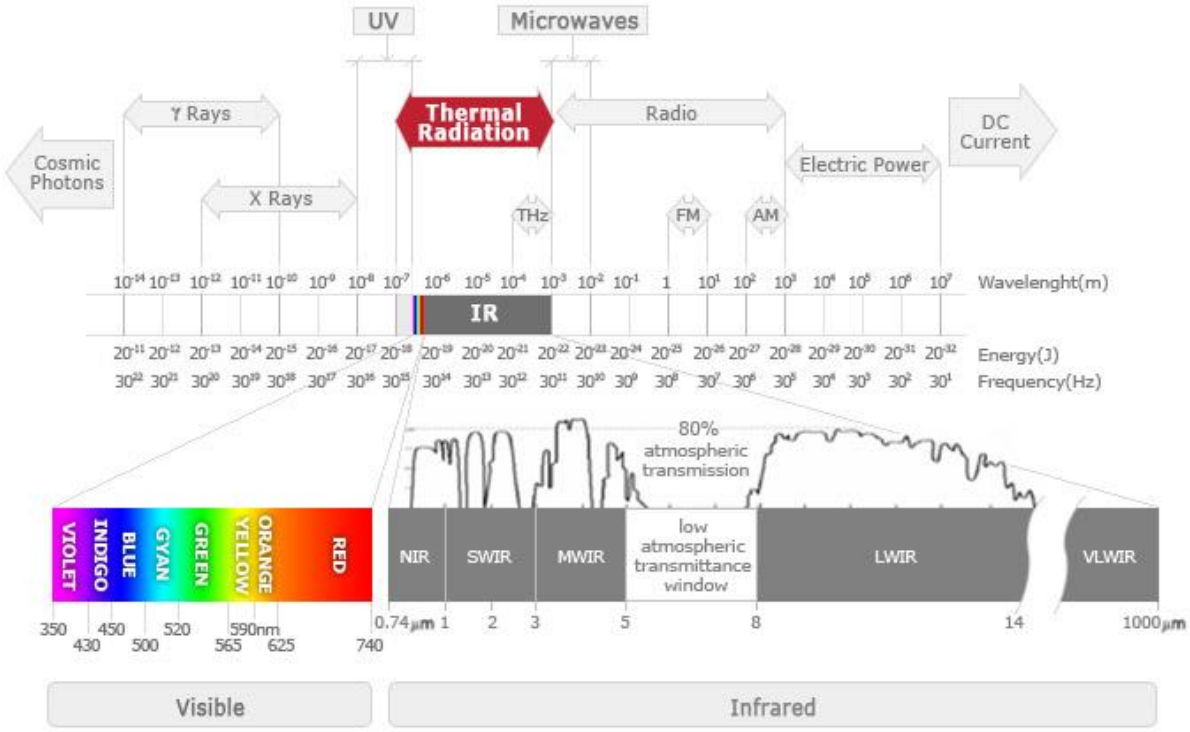

Figure 2: The electromagnetic spectrum (Cox Thermal imaging cameras 2015, Infrared Thermography s.p.).

The relationship between wavelength, frequency and energy is described in the following equation (Kable 2019, 6):

$$E = hf \quad \longleftrightarrow \quad c = f\lambda \quad \longleftrightarrow \quad E = \frac{hc}{\lambda}$$

Where:

- E = energy of the photon (Joule or electronvolt);
- h = Planck's constant = $6{,}626.10^{-34}$ Joule seconds;
- f = frequencies (hertz);
- c = speed of light = 299 792 458 meter per second;
- λ = wavelength (meter).

High-energy bands (gamma rays or the left side of the spectrum illustrated in figure 2) have shorter wavelengths and higher frequencies, while lower-energy bands (radiowaves or the right side of the spectrum illustrated in figure 2) have longer wavelengths and lower frequencies. When one parameter is known, the other one is easily calculated.

These different types of EM radiation examine particular parts of the material, through the interaction of the incident beam with the molecules or atoms which the studied material is composed of and the detection of the (narrow selection of) re-emitted radiation. There are a couple of ways of interaction between the incident beam and the molecules or atoms of the material (figure 3):

- Transmission or **transmittance**: the EM radiation of the incident beam goes through the medium;
- (specular) **Reflection**: the incident beam is reflected on the surface so that the angle between the incident beam-surface normal and the surface normal-reflected beam is the same;
- **Diffusion** or scattering: the incident beam is reflected in many directions;
- **Absorption** (figure 4-left): the transformation of EM energy into a different type of energy (such as heat) due to the absorption of the energy (excitation from the ground state to excited state);
- **Emission** (figure 4-right): released energy when an electron falls back to the ground state.

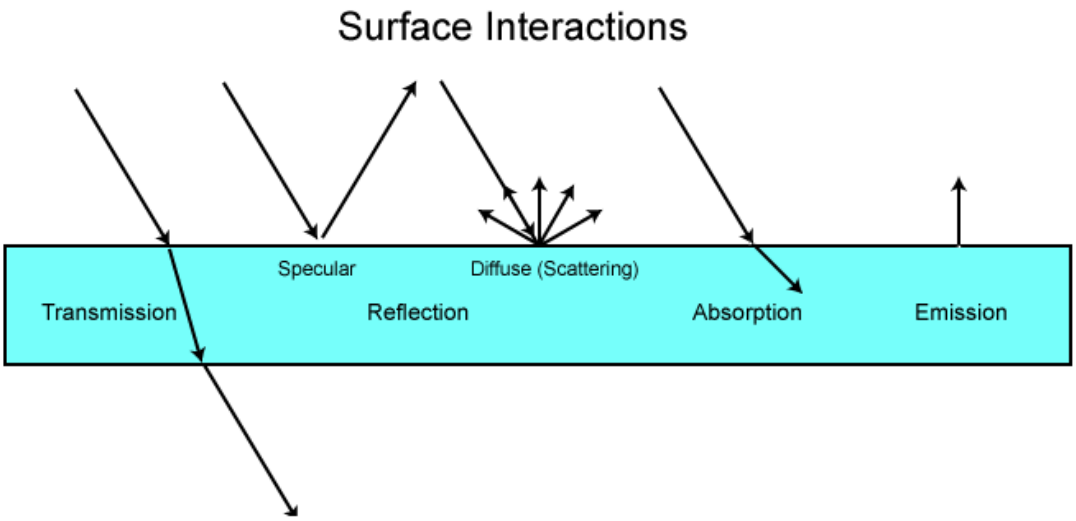

Figure 3: Different interactions between the incident beam and the surface (Zaboli 2019, s.d.).

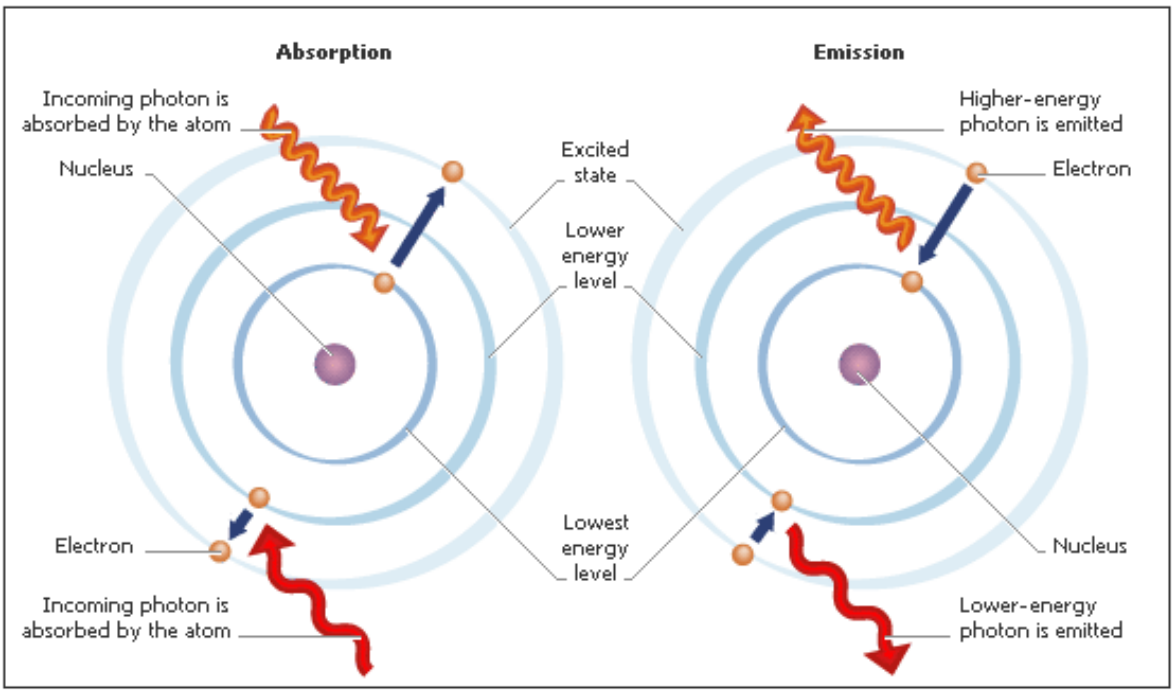

Figure 4: Absorption and emission (Konstantakopoulos 2002, s.p.).

3.2. Luminescence

Luminescence is the process of light emission and consists of five groups: chemiluminescence, thermoluminescence, electroluminescence, radioluminescence and photoluminescence. The latter is the most applicated in the study of figurative art.

- Chemiluminescence is the emission of light triggered by a chemical reaction. When living organisms or enzymes are used, the process is called bioluminescence;
- Thermoluminescence light occurs when an object is subjected to heat exposure and the high-energy electrons are released and light is produced. This is used in archaeology for dating;
- Electroluminescence uses an electric current or field to emit light;
- Radioluminescence is where light is produced after the surface is subjected to ionizing radiation or high-energy particles (Föll 2015, types of luminescence, s.p.).

Photoluminescence is the emission of light (with different wavelengths) triggered by light in the UV-Vis-NIR spectral region. Fluorescence and phosphorescence are both types of photoluminescence (figure 5). Until singlet excited state 1 (S_1) the principle is the same: A light is absorbed, this results in an electronic excitation where the electrons move from the ground state (S_0) to (in this example) S_2. This is an unstable state and the electron relaxes (after several seconds) back to the ground state by several mechanical steps:

- When the energy is dissipated without going to another excited state (or ground state) this is called **vibrational relaxation** (indicated as a curved orange arrow). This dissipated energy is kinetic and non-radiative.
- When there is an overlap in vibrational and electronic energy, the excited electron can transition to a vibration level of a lower electronic state (S_2 to S_1). This is called **internal conversion** (indicated as a curved purple arrow) (Kable, 2019, 8-10).

The observation of **fluorescence** (indicated by the straight green arrow) occurs when the electron relaxes from S_1 to S_0. This results in the emission of a photon with lower energy and a longer wavelength (because it has lost some due to vibrational relaxation and internal conversion). Important to know is that the electron spin is the same during all the transitions and the light is only visible when a light source is switched on. This is different from phosphorescence (Kakoulli et al. 2017, 105; Nocerino et al. 2018, 774; Kable 2019, 13-14).

Phosphorescence (indicated with a straight red arrow in figure 5) happens when an electron relaxes from a triplet state (T_1) to S_0. This triplet state lies energetically between S_1 and S_0. In order, an electron can transition from a singlet state to a triplet state the process of intersystem crossing has to take place (indicated by the curved pink arrow). As with internal conversion, it is enhanced when the vibrational levels of two different states overlap with each other. In contradiction to internal conversion, a spin reversal (going from ↑↓ to ↑↑) occurs. When an electron relaxes the electron spin shifts back (from ↑↑ to ↑↓) and a photon is emitted. This process is slower than those of fluorescence and therefore the energy or light is trapped longer which results in a slower release. This light is only visible as an "afterglow" when the light is switched off (Kable 2019, 14-15).

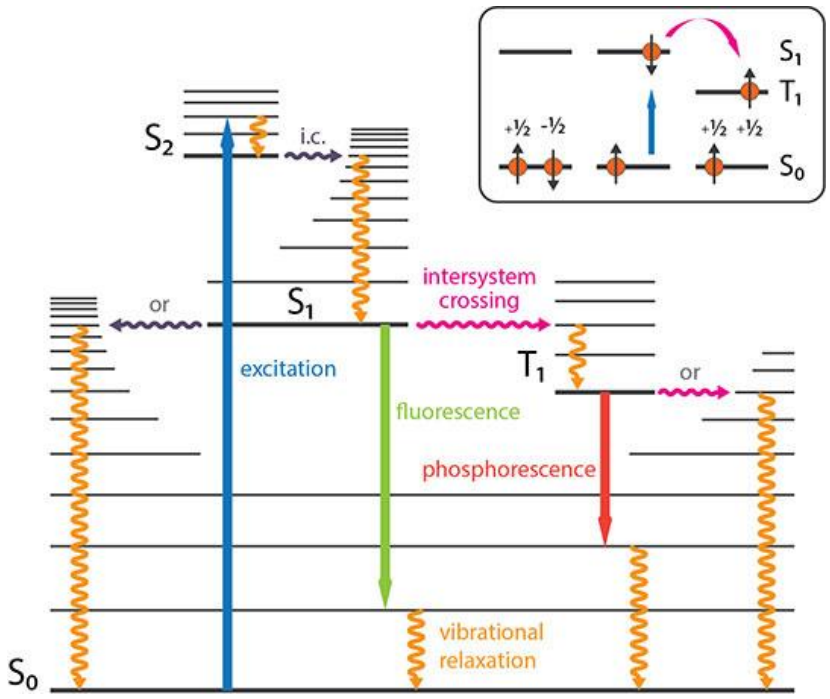

Figure 5: Jablonski Diagram showing principles of fluorescence and phosphorescence (Pohl 2019, Fig 1, s.p.).

3.3. Waves

A wave transfers energy and can be divided into two categories: electrical waves, such as EM-waves and mechanical waves, such as sound. It is characterized by the following elements:

- Amplitude: the maximal displacement from its equilibrium (figure 6A)
- Wavelength (λ in meter): the length between one maximum or minimum to another maximum or minimum when measured over distance (figure 6B);
- Time period (T in seconds): the length between one maximum or minimum to another maximum or minimum when measured over time (figure 6B);
- Frequency (f in Hz): the duration of time for one cycle/wave (Fischer-Cripps 2020, 19-26).

The relationship between the elements is: $f = \frac{1}{T}$ and $\lambda = \frac{v}{f}$, where v is speed ($\frac{m}{s}$). The higher the frequency, the shorter the wavelength (Fischer-Cripps 2020, 23).

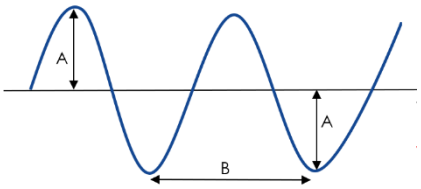

Figure 6: The elements of a wave.

To understand the role of waves in certain principles (here most often Fourier transform and phase-shift) trigonometric ratios and their relation with a unit circle are often applied (Fischer-Cripps 2020, 27). Briefly, a circle can be expressed with coordinates of certain points expressed in radius or degrees (figure 8). For instance π = 180° = (-1, 0) or $\frac{\pi}{4}$ = 45° = $(\frac{\sqrt{2}}{2}, \frac{\sqrt{2}}{2})$.

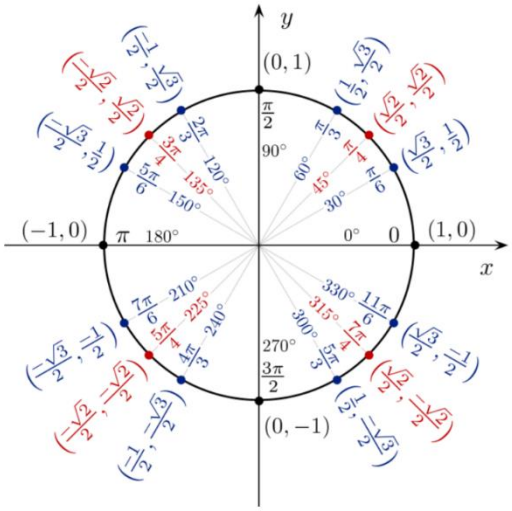

Figure 7: The unit circle with coordinates and their spatial angles (Lumen Learning 2017, Trigonometric Functions and the Unit Circle, s.p.).

II. Geometrical methods

In this section, the techniques relying on the geometrical aspects of an artefact will be explained. These aspects can be approached through morphology, where the form or shape of an object is the key element. The study of the contour or defining points or lines is frequently used for obtaining typologies for relative dating of ceramic and lithic materials. The following techniques will show that figurative art or pictorial elements can be used for variation between and within groups or for pattern recognition.

1. Morphometry

Morphometry has a close affiliation with the term 'morphology' and therefore related to the external form and shape of an artefact. In morphometry, the appearance and characteristics will be measured with quantitative analyses. Its origin lies in the field of biological shape analysis from the 20th century onwards, more precise the ecological and evolutionary biology. The researchers used this method to determine the phenotype, skeletal analyses, the functional importance of certain features, comparing anatomical features, mutations in genes, within-species variations, etc. (Adams, Rohlf, Slice 2004, 5; Slice 2007, 262; Lawing, Polly 2009, 1;5).

It gained much interest in the study of lithic materials, but not for figurative art, with exception of an anthropomorphic figurine from Mexico and a figurine from the Allier and Loire valleys of France. Mexico and France are not a part of the geographical area of the Mediterranean, Cyprus and Near East, but the applicability of this technique has to be mentioned.

There are two main fields in morphometry (figure 8): traditional morphometrics, which is also the oldest method and geometric morphometrics. The main distinction between both fields is the type of parameters used to identify the external characteristics of an object. In traditional morphometry distances, such as length, ratios and widths are measured on the object itself. These are significant to determine the size of the studied artefact. Since non-homologous points are used, the necessity of size correction and the event where different forms can have the same distances, the need for a new approach was essential, because these problems cause a tremendous loss of the

geometry of the artefact. The alternative method in traditional morphometrics uses angles since these are not dependent on location, orientation (such as distances) and size (Adams, Rohlf, Slice 2004, 6; Buxeda I Garrigós, Gordaliza 2011, 2; Herzlinger, Goren-Inbar, Grosman 2017, 165).

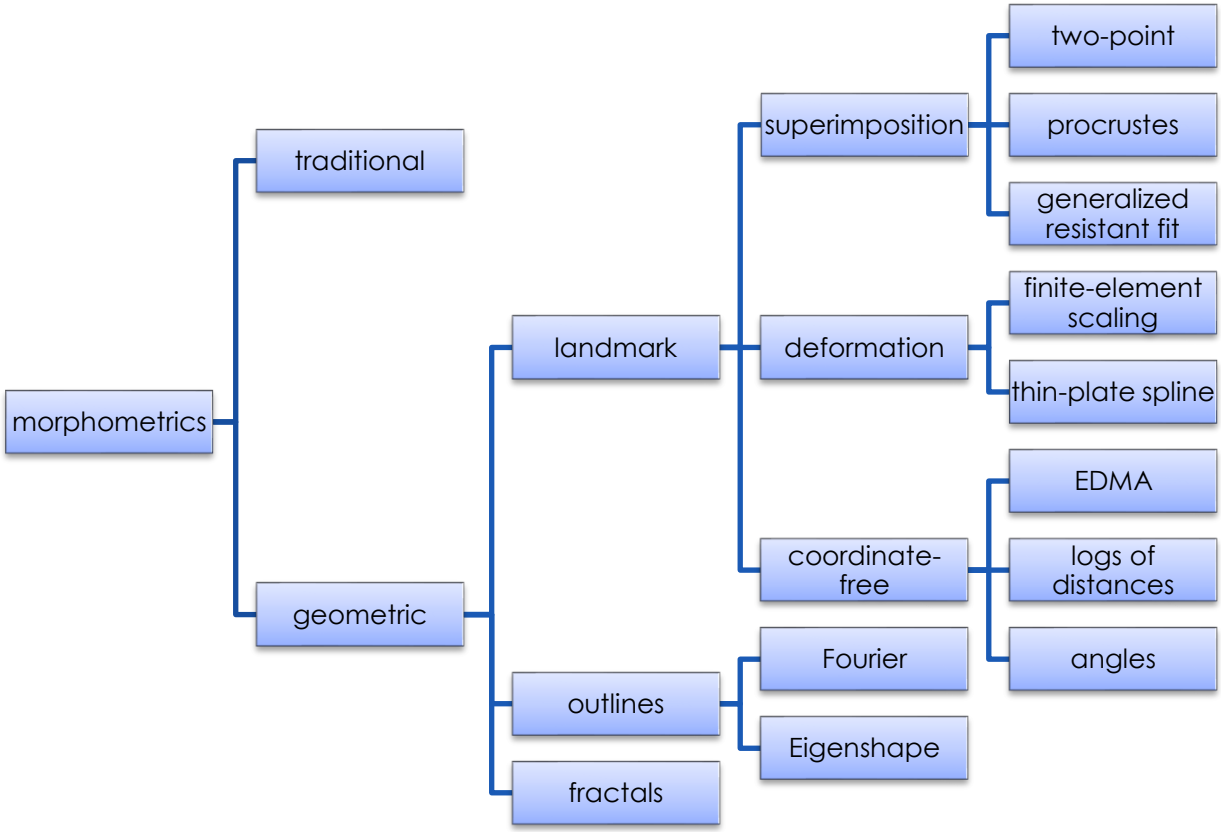

Figure 8: The different fields of morphometrics.

Geometric morphometry uses three ways of measuring the shape of an artefact: landmarks or coordinates (with exception of the coordinate-free methods), outlines or coefficients of mathematical functions and fractals. In the following paragraph, the theory behind these methods will be explained shortly, for the mathematical background the corresponding references will be given (Slice 2007, 262; Lawing, Polly 2009; Herzlinger, Goren-Inbar, Grosman 2017, 165).

1.1. Theoretical principle

Whereas the traditional morphometry generates a loss in geometry and is not used as much, the following section will be focused on geometric morphometry. Here the shape is the central highlight and it is necessary to define it. The shape of an object is the external outline or surface and can be points, lines, circles, polygons and three-dimensional structures. It has all the geometrical information independent to orientation, size or scale and rotation (also called nuisance parameters). The phenomenon of shape is important to understand the culture, the manufacturing processes, the trade process, the vision and understanding of the studied artefact (Lawing, Polly 2009, 1; Buxeda, Garrigós, Gordaliza 2011, 2; Dumoncel 2017, 55-56).

As been said above shape is interpreted in three ways: landmarks, outlines and fractals. The result of these methods is more or less the same, namely shape variables, but the process to acquire them differs (figure 8 and 9). The first step will consist of constructing these shape variables. In the second step, the obtained shape variables will be statistically tested and in the final step, a graphical representation will be made if possible. Where the first step alters, the second and final step is principally the same for each method.

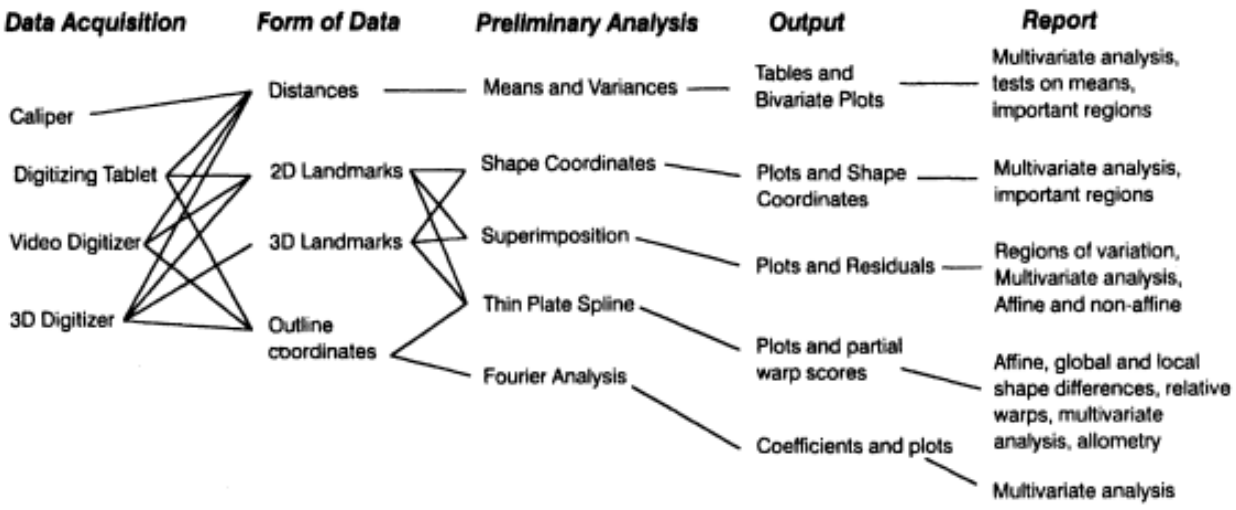

Figure 9: Some methods applicable in geometric morphometrics (Marcus, Corti 1996, 9, Fig. 1).

Landmarks are anatomically interesting points of precise locations on the surface of an artefact. Between two or more artefacts these chosen points match. The locations can be expressed in a two- (2D) or three-dimensional (3D) coordinate system. In this way, the shape is expressed by points in a Cartesian space model, where it is possible to form a map of the relative locations of the chosen landmarks (Slice 2007, 262; Buxeda, Garrigós, Gordaliza 2011, 8; Herzlinger, Goren-Inbar, Grosman 2017, 164).

There are different classification of landmarks produces by Bookstein (1991) Dryden and Mardia (1998) and Lele and Richtsmeier (2001), summarised in table 1 (the cells in every row does not correspond with the same classification).

Table 1: The classification of landmarks

Bookstein (1991)	Dryden and Mardia (1998)	Lele and Richtsmeier (2001)
Type I: mathematical homologous point	Semi-landmarks: points at an interval along a curve	Homologous
Type II: mathematical homologous point supported by geometry	Pseudo-landmarks: self-constructed points on artefact/object	Functional corresponding
Type III: Mathematical point with one deficient coordinate dependent on location and orientation	Mathematical landmarks: locating with mathematical or geometrical assets	Structural corresponding
	Anatomical landmarks: points with biological significance	Developmentally corresponding

Outlines or contours are 2D representations of the edges of the artefact and coincide with the perimeter of the structure (Lele, Richtsmeier 2001, 29). In contradiction to landmarks, the curvature and the underlying structure of the artefact can be preserved and observed, whereas the six landmarks (now not homologous) are the same. This can be seen in figure 10. From the curvature the curve coefficient can be calculated, which will be used as the shape variable (= different with landmarks). Afterwards, these mathematical functions of open and closed outlines can be produced and used in the multivariate analysis (Adams, Rohlf, Slice 2004, 6; Slice 2005, 10; Buxeda, Garrigós, Gordaliza 2011, 4).

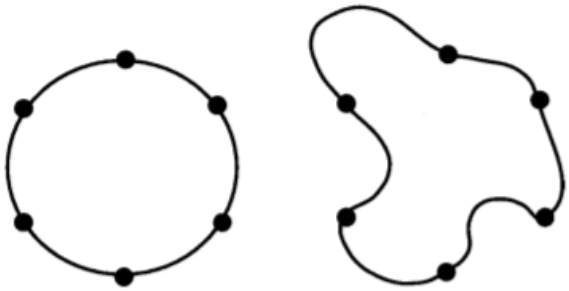

Figure 10: The main advantage of the use of outlines (Lele, Richtsmeier 2001, 30, Fig. 2.2.).

Fractals are used when an object its structure is too complex by irregularities that it cannot be described by Euclidean geometry. These objects have the same geometrical structure on each scale of magnification. Fractal dimensions will be used to estimate the surface of an object (Prossinger 2005, 168; Martin-Garin et al. 2007, 542; Pérez-Rodríguez, Jovani, Stevens 2017, 7).

1.1.1. Step one: constructing shape variables in case of landmarks

To obtain shape variables (vectors) or coordinates (which are invariant to translation, rotation and scale) in this case three different mathematical procedures can be used (Figure 1 and 2): the superimposition methods (A-C), deformation methods (D-E) and coordinate-free methods (F-G). For each of these methods, the basic principles will be explained, the more elaborated explanations can be found in other related papers and the given references.

A. Two-point registration

Also known as base-line registration or edge matching of 2D data is developed by Fed L. Bookstein. The position and size are characterised by the coordinates of a landmark, while the orientation and scale are characterised by the baseline or 'distance' between two points. After the removal of location, the baseline is orientated so that the x-axis contains the coordinates of two of the three landmarks (in case of using only three landmarks as in figure 11) which are located at the origin (0,0) and (0,1) or (1,0). The last coordinates contain information about the shape (Marcus, Corti 1996, 3; Slice 2005, 12;14).

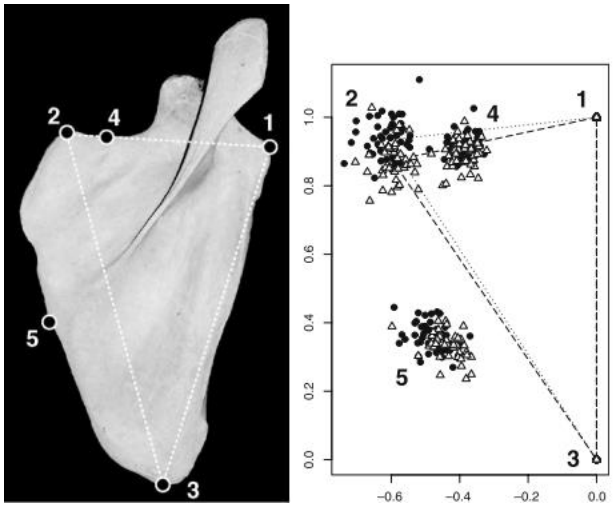

Figure 11: An example of two-point registration (Slice 2005, 13, Fig. 3).

B. Procrustes Analysis or Procrustes superimposition

This least-squared method helps to determine if two artefacts have an equal shape and/or can measure the difference between two shapes, i.e. to quantify the shape variations. Pioneers in this study are David G. Kendall, Fred L. Bookstein, Dennis E. Slice, Christopher G. Small, F. James Rohlf and many more. There are different 'morphospaces', where one space can be evolved in another space when subjecting it to different processes which eliminate each one of the nuisance parameters (translation, rotation and orientation).

In the initial space, the size and shape of the object maintain and are called the **figure space**. To make it more approachable the chosen landmarks can be positioned in a corresponding arbitrary coordinate system, where a k x p matrix of coordinates of an object can be considered. K represents the number of landmarks and p the number of dimensionalities of the physical space. Thus, a shape can be represented as a matrix with 'kp' columns and 'n' rows. The landmarks are then translated (= the movement of all the points by an equal distance) and centred (figure 12 second column), so they have the same centroid size or log-transformed centroid size (Klingenberg 2016, 115; Polly, Motz 2016, 72; Tatsuta, Takahashi, Sakamaki 2018, 167).

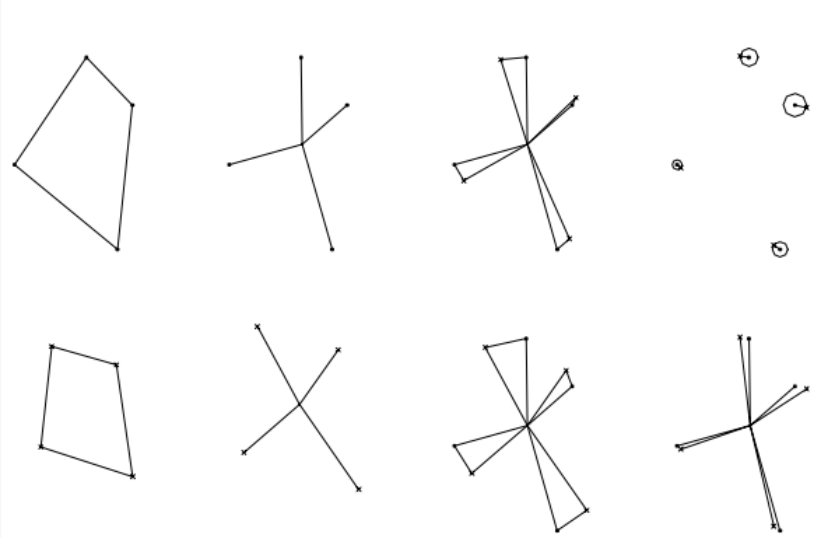

Figure 12: The steps for losing the nuisance parameters (Bookstein 1996/7, 227, Fig. 3).

According to Bookstein (1991, 94), Slice (2005, 17) and others, the centroid size is the square root of the total of squared distances from all the landmarks to the centroid of the configuration. This makes it possible to work with a standard size variable (scaling factor) and generates a loss of location. The configuration now lies in the **pre-form space**.

From this point of view, two pathways can be taken, but the one most used is the following: the configuration will be scaled independently to a unit size (by dividing the landmark coordinates by their centroid size) where it now lies in a **pre-shape space**. As can be seen in figure 13, the pre-shape space is a hemisphere. At coordinates (0,1) the mean reference shape (O) is positioned. In this hemisphere, the geometrical points lie on a surface of a dimensional manifold of kp – p – 1. The size of the landmark configuration has been reduced to cos (ρ). Cos (ρ) is also called the partial chord Procrustes distance (Dp) and is the Euclidian distance from a shape position (point Tp) to the reference shape, position (0,0). ρ is the smallest great circle and is the angle between the line from the centre of the hemisphere (0,0) to the reference shape (0,1) and the line from (0,0) to another shape (point Tp). The maximum value is $\frac{\pi}{2}$ between two shapes (Rohlf 1999, 199; Tatsuta, Takahashi, Sakamaki 2018, 167).

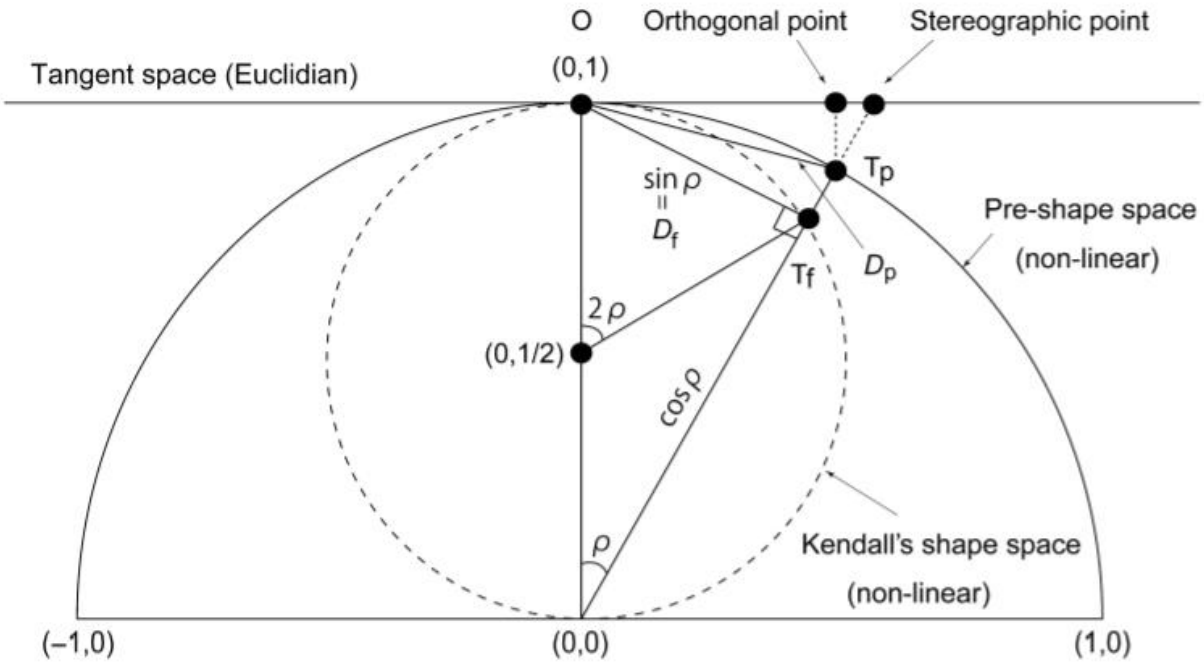

Figure 13: The three morphospaces (Tatsuta, Takahashi, Sakamaki 2018, 168, Fig. 3).

After scaling, the configuration will be rotated (figure 12, third column) so that there will be a minimal sum of squared distances (figure 12, fourth column) between the reference and target landmark configuration. Because the partial chordal Procrustes distance is not the shortest distance between the two shapes, there needs to be a rescaling, by again minimising the distance by changing the centroid size of the target shape (now Tf). By doing so the configurations "enters" a new space, named the **Kendall shape space**. In contrary to the previous space this is a sphere with radius ½ and dimensionality of (kp – k – 1 – k x (k – 1))/2. The distance of the reference shape (0,0) to the other shape (point Tf) is now called the full chordal Procrustes distance (Df) or sin (ρ) (Rohlf 1999, 203-205; Tatsuta, Takahashi, Sakamaki 2018, 167).

A final step removes the degrees of freedom from the landmarks. This step is important for statistical analysis. The degrees of freedom is related to the nuisance parameters dependent on the dimensions. For 2D data, the degrees of freedom are one of scaling, two for translation and one for rotation, which gives a total degree of freedom of 2*p* – 4. For 3D data the degrees of freedom are one of scaling, three from translation and three from rotation, given a total degree of freedom of 3*p* – 7 (Rohlf, Corti 2000, 744; Slice 2005, 9; Polly, Motz 2016, 76).

The spaces explained above are curved (non-linear), but Euclidean, linear spaces need to be considered as well. This can be done in a **tangent projection** of the surface of the sphere (figure 13). Two types of projections can be done for creating a tangent space: a stereographic projection resulting in stereographic shape coordinates (figure 13) or a projection of the pre-shape hemisphere perpendicular to the direction of the axis of the hemisphere resulting in Kendall tangent space coordinates. The latter coordinates can be converted to shape coordinates using **partial warp scores or PC scores** (Rohlf 1999, 207; Tatsuta, Takahashi, Sakamaki 2018, 168).

The obtained landmark coordinates are used as shape variables (without the nuisance parameters) and subjected to multivariate statistical tests (figure 14, C), which will be explained in the second step (Buxeda I Garrigós, Gordaliza 2011, 8; Klingenberg 2016, 115; Tatsuta, Takahashi, Sakamaki 2018, 167).

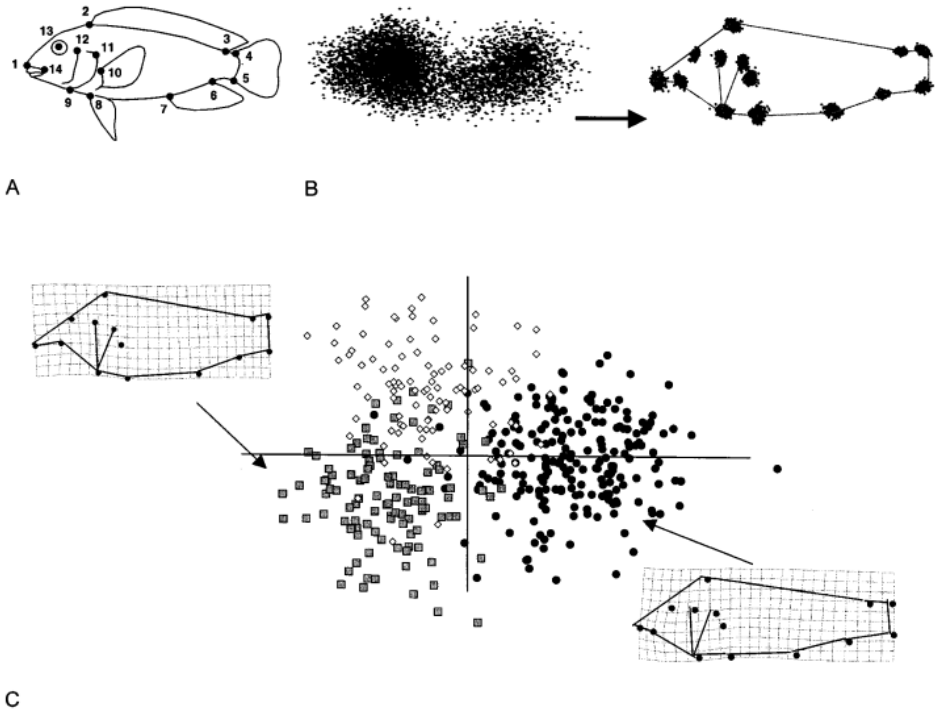

Figure 14: The different steps of a GPA (Adams, Rohlf, Slice 2004, 8, Fig. 2).

The method explained above is also called Ordinary Procrustes Analysis (OPA), which is normally done for one or two samples. When more than two samples are compared, it is called Generated Procrustes Analysis (GPA, figure 14). Here the sample (or landmark configurations) will be fitted on a repeated computed mean (Slice 2005, 18; Tatsuta, Takahashi, Sakamaki 2018, 168).

C. Generalized resistant-fit (GRF)

GRF estimates the local differences. The angle and scale will be rotated according to their medians and translated with a simple coordinate-wise median. This method won't need any statistical analysis afterwards (Adams, Rohlf, Slice 2004, 7; Slice 2005, 19).

D. Finite-element scaling analysis (FESA)

FESA can be best explained in figure 15. First, the landmark points are located either in 2D- or 3D-coordinates both for at least two samples (a and b). Then both configurations are superimposed (c). This can be done by the two-point registration (see A from this section) or by fixating one point and one coordinate (Vogl 1993, 342). Now it is possible to construct vectors in the form of displacements in x-, y- and z-coordinates between the two samples (d). To create finite elements, the displacements are interpolated. Finite elements (e) form elementary geometry of the larger sophisticated structures or in case of homologous points, a mathematical function maps the position of the homologous points correlating to each finite element in both samples and this is rather difficult. In the final step (f) strains (triangles or tetrahedron) will be calculated. These are first-order spatial derivates of the displacements of (d). This technique is highly criticized in Bookstein (1991, 254) (Marcus, Corti 1996, 5; Richtsmeier, Deleon, Lele 2002, 78-79; Adams, Rohlf, Slice 2004, 7).

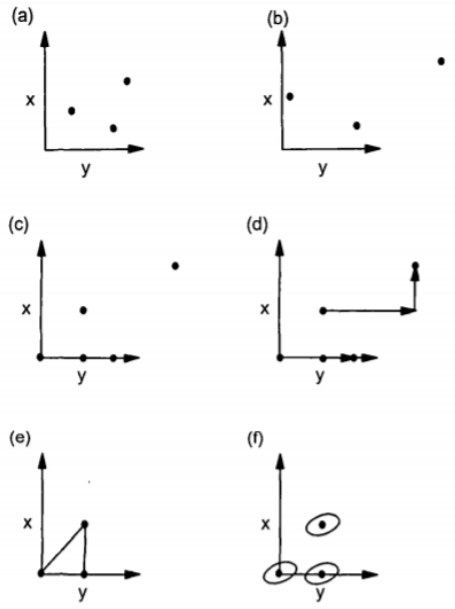

Figure 15: The principle of FESA (Vogl 1993, 342, Fig. 1).

E. Thin-plate splines

Thin-plate splines (TPS) is a deformation method (figure 16) used to visualise the tangent space, firstly presented by D'Arcy Wentworth Thompson in 1917. It is a smooth interpolation function that models the variation in shape between several landmark configurations by minimizing the bending energy necessary to deform the grid of a reference object to a target object (Richtsmeier, Deleon, Lele 2002, 79; Adams, Rohlf, Slice 2004, 7; Cooke, Terhune 2015, 8).

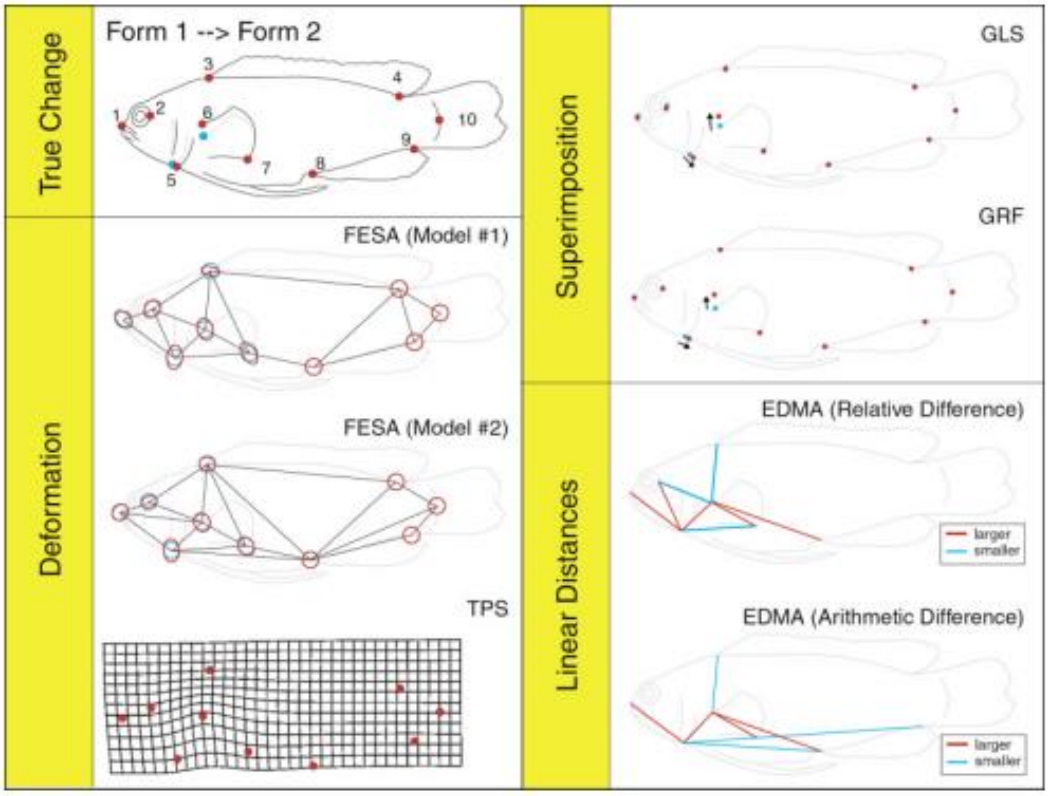

Figure 16: The three main groups of landmark-based methods (Richtsmeier, Deleon, Lele 2002, 79, Fig. 10).

The deformation can be expressed by six uniform or affine shape components and non-uniform or non-affine shape components: translation along a vertical and horizontal axis, shearing, rotation, scaling and compression or dilation (Tatsuta, Takahashi, Sakamaki 2018, 169).

The coefficients are known as partial warps of the TPS are used in statistical analyses (Adams, Rohlf, Slice 2004, 7; Monteiro et al. 2004, 339; Tatsuta, Takahashi, Sakamaki 2018, 168-170).

F. Euclidian distance matrix analysis (EDMA)

EDMA is a frequently used method in a coordinate-free model and three or more landmarks can be processed. Coordinate-free models can remove any influence of the nuisance parameters of translation and rotation (Lele, Richtsmeier 2001, 160; Adams, Rohlf, Slice 2004, 9; Slice 2005, 35).

By taking landmarks with a higher ratio of variance into account, a matrix of their inter (linear)-distances is formed, called a Euclidean Distance Matrix (EDM) or Form Matrix (FM). The ratios of the distances (figure 16) are compared between different samples, where a constant ratio equals a similar shape (Slice 2005, 36; Lawing, Polly 2009, 2-3; Buxeda, Garrigós, Gordaliza 2011, 4;8).

G. Size corrected logs of distances and angles of landmarks

These two coordinate-free methods are not used very often. Either the matrices of logs of distances are being compared between samples or the inferior angles are used. Both distance and angle are invariant to location reflection and orientation, but angles are also invariant to size. So there is no need for a superimposition step (Adams, Rohlf, Slice 2004, 9).

1.1.2. Step one: constructing shape variables in case of outlines

Outlines can be analysed with four types of analyses: Fourier analysis (A), Eigenshape analysis (B), as a function and when approached as semi-landmarks (C) with Procrustes superimposition (explained above). These can be used for closed or open outlines.

A. Fourier analysis

Elliptic Fourier analysis (EFA) is described in the 1980s' by Kuhl and Giardina and is used for analysing 2D closed outlines. The main principle of EFA is a deconstruction of the curve into one or more harmonic ellipses made out of sine and cosine waves. This deconstruction is possible by approximating the contour as a chain code (figure 17).

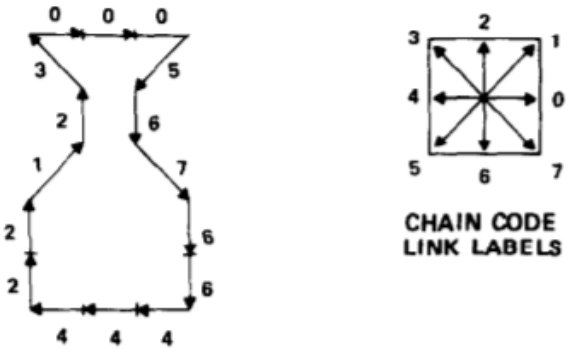

Figure 17: The usage of a chain code in Elliptical Fourier analysis (Kuhl, Giardina 1982, 237, Fig. 1b).

This is a series of directions according to one of the values which are appointed to this direction, called link labels. When looking at figure 17 the following code can be received, when starting at the bottom left corner: 2212300056766444. This code is afterwards converted to elliptical Fourier descriptors (EFD) and the latter can then be converted to harmonic coefficients. These coefficients can recreate the shape of the original object. The more harmonic ellipses are employed (figure 18), the more details are added, the better it represents the original and the sum of harmonics is a degree of fidelity (Baylac, Frieß 2005, 151; Slice 2005, 37; Krieger 2010, 34-35; Tatsuta, Takahashi, Sakamaki 2018, 173):

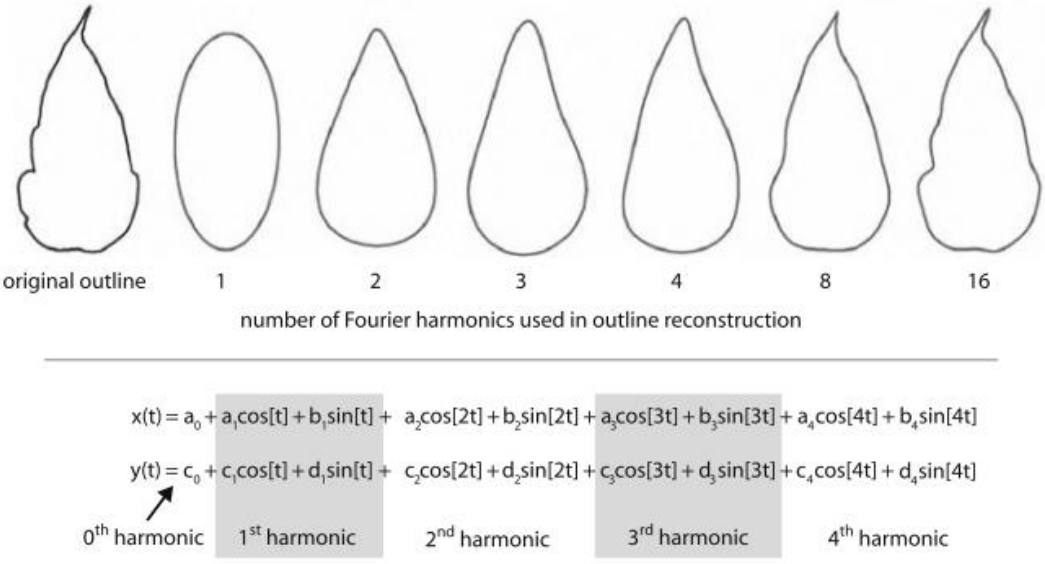

Figure 18: The Elliptical Fourier Analysis with parametric equations for x and y (Krieger 2010, 34, Fig. 3.4).

Each harmonic function has four parameters, as can be seen in the parametric equations for x and y: a_i, b_i, c_i, d_i. In this way, the outlines can be reconstructed based on these coefficients which are later be used as inputs for the statistical analysis, mostly principal component analysis (PCA) (Baylac, Frieß 2005, 151; Slice 2005, 37; Krieger 2010, 34-35).

Another type of Fourier analysis is the discrete cosine transform (DCT), which is a Fourier-related method for 2D and 3D open outlines (Dommergues, Dommergues, Verrecchia 2007, 2; Tatsuta, Takahashi, Sakamaki 2018, 174).

B. Eigenshape analysis (ES)

ES is a linear function of observed data across one or more objects. In this case, shape is been represented by angles with x and y coordinate data. It can be used for closed and open outlines. Usually, this method has four steps (figure 19) and is described by Lohmann (1983):

- The description of shape in the form of the x and y coordinates;
- The aligning of the objects is done by converting the data into phi functions. This allows the removal of the nuisance parameters. The coordinates are changed to the alteration of the angle needed to follow the outline;
- Deconstruction into orthogonal functions is where a singular value decomposition (SVD) is constructed of covariance matrix or correlation matrix;
- Modelling or visualization of the shape in morphospaces (Krieger 2010, 37-39; Reyment 2010, 17).

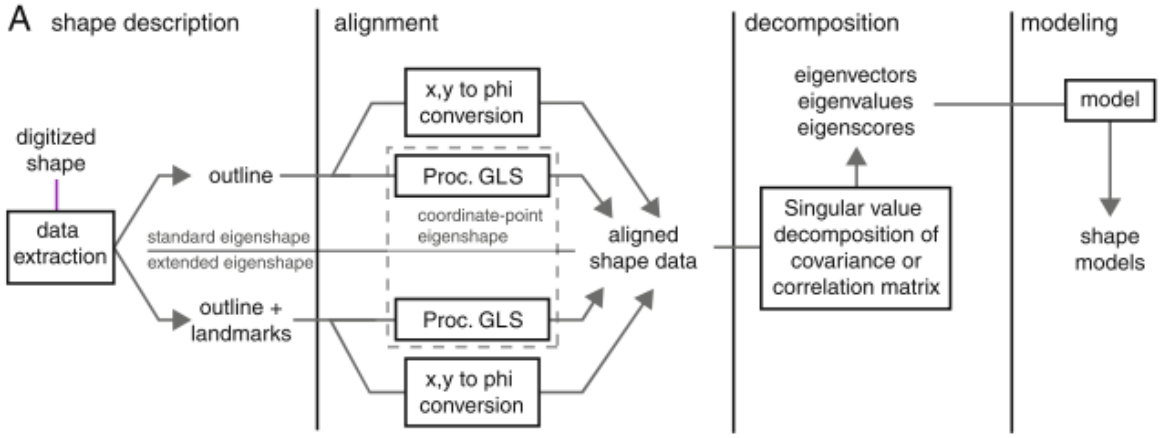

Figure 19: Eigenshape analysis (Krieger 2010, 38, Fig. 3.5).

As can be seen in figure 19 the analyses of outlines or semi-landmarks can be done by phi functions and with Procrustes superimposition for aligning 2D or 3D outlines or semi-landmarks (Lawing, Polly 2009, 3; Krieger 2010, 39).

C. Semi-landmarks

Semi-landmarks are points lying along a curve between two landmarks. They are treated the same as landmarks and submitted to GPA to remove the nuisance parameters (Slice 2007, 271; Polly, Motz 2016, 74).

This method can be optimized by using sliding semi-landmarks. The points are slid (in a tangential plane) following the curve until they roughly match the position of the corresponding point in the reference configuration. There are two ways of sliding a point along an outline. The first one is the minimum bending energy, which can be related to THS (figure 20a). The second method is the minimum Procrustes distance (figure 20b). Here the tangential direction is estimated, and semi-landmarks are aligned at the curve perpendicular to the points of the corresponding reference configuration (Adams, Rohlf, Slice 2004, 10-11; Perez, Bernal, Gonzalez 2006, 770-771).

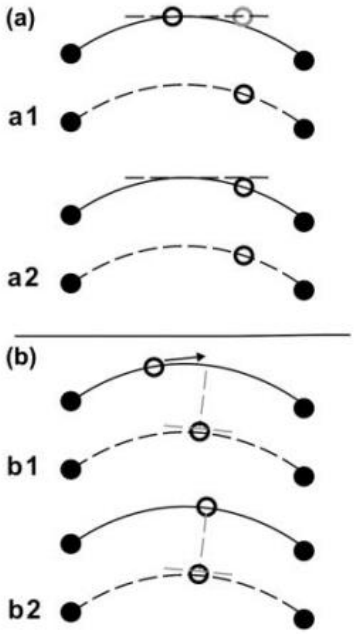

Figure 20: Two ways of sliding a semi-landmark along a curve (Perez, Bernal, Gonzalez 2006, 770, Fig. 1).

1.1.3. Step one: constructing shape variables in case of fractals

The box-counting method is one of the easiest methods available to measure fractals. It is related to the perimeter measuring methods but here a square mesh grid of various sizes and number of boxes is used to cover an image. How smaller the boxes the more accurate the structure of the pattern will be. In this case, the surface is seen as a unit of measure. Three types of fractals are recorded:

- δ_B represents the boxes filled by the object;
- δ_W represents the boxes not filled by the object;
- δ_{BW} represents the boxes partially filled by the object. This one contains the most information about the irregular outlines (Martin-Garin et al. 2007, 542-545; Falconer 2014, 31; Pérez-Rodríguez, Jovani, Stevens 2017, 7).

A bivariate plot or Richardson is created where the relation between the logarithm of the number of boxes necessary to cover the pattern and the logarithm of the sizes. The slope of the resulting curve represents the fractal dimension. In case, of a linear correlation, the slope shows a lower value and corresponds with fewer details. When inflexion points or abrupt shifts appear in the curve, in other words, a higher slope value, the complexity increases with decreasing box size. These fractal dimensions can be used as an indication of similarity in complexity (Martin-Garin et al. 2007, 544; Barceló 2010, 113).

1.1.4. Step one: constructing shape variables in case of 3D structures

Since 3D models are easily created through photogrammetry, laser scanning, structured light and tomography, more attention is given to the analysation of 3D-structures of artefacts. Because homologous points cannot be distinguished (unless when studying humans or representatives of humans) semi-landmarks and landmarks are combined used.

To position (semi-)landmarks on a 3D-model, an orthogonal deformed grid is created. The number of latitudes and landmarks per latitude needs to be defined and consistent per artefact. The more (semi-)landmarks are used the higher the accuracy but the longer the processing time. The data acquisition can be based on GPA,

Eigensurface or spherical Fourier harmonics (similar to Fourier analysis of outlines) (Herzlinger, Goren-Inbar, Grosman 2017, 164-167; Herzlinger, Grosman 2018, 2-5).

Recently a new software program for archaeological purpose is constructed based on the programming language of Matlab ® by Herlinger and Grosman (2018), called Artifact GeoMorph Toolbox 3D (AGMT3-D). This software program makes the data acquisition process automatic and conducts the statistical procedures as well (Herzlinger, Grosman 2018, 2-5).

1.1.5. Step two: multivariate statistical analyses

In the **second step** will the acquired shape variables or coordinates statistically be tested. This is possible with the following techniques:

- Lining the different object along axis of shape variation to investigate the relationship between variables with PCA;
- Testing the correlation between shapes of different structures with two-block partial least squares (2B-PLS);
- Differentiation between datasets and reducing the data with PCA, canonical variates analysis (CVA) and discriminant function analysis (DFA);
- Testing three differences of group means with Hotelling's T^2-test and multivariate analysis of variance (MANOVA);
- And many more (Lawing, Polly 2009, 4; Cooke, Terhune 2015, 8-9; Polly, Motz 2016, 76).

1.1.6. Step three: visualization

In this final step, a graphical representation will be made. This can be done by various programs and depends on the hypothesis of the research. Often the PC-scores or partial warp scores are used to see differences within and between groups. Cluster analysis can be applied to group a larger data set based on their similarities. A difference-vector diagram can be created, which has a similar role as PC-scores but with vectors instead. (Slice 2007, 266; Polly, Motz 2016, 79)

1.2. Advantages and limitations

Since geometric morphometrics consists of various techniques it is crucial to assess beforehand which technique will give the best results for a certain type of research question. Each one of them has its own advantage and limitation.

Except of 3D-models, most analyses are based on 2D images of the object. These will always have a certain degree of distortion due to deformation or the angle of where the picture is taken and needs to be considered when interpreting the results. When there is no ambiguity in type of landmarks the data is easy to collect and analyse since it is almost fully automated. Three main advantages of landmark coordinates are:

- The study on the artefact an sich or its 2D (x and y coordinates) or 3D (x, y and z coordinates) images with special software;
- The chance to study triplets of points (characterised by the already mentioned parameters location, orientation and size);
- The representation of shape in the form of dimensions (example for two dimensions: $2p - 4$, where p are the number of points) (Slice 2005, 9).

But in case of archaeological objects often semi-landmarks are used and when assessing a big collection these points must be identical with each object. This can be time-consuming. Other advantages are the efficiency of linking data sets with compositional data analysis or with PCA and the fact that almost all software (both data acquisition and processing) is free (Rohlf 1996, 120; Lele, Richtsmeier 2001, 30; Lawing, Polly 2009, 1-3; Buxeda I Garrigós, Gordaliza 2011, 4-7; Falconer 2014, 27; Polly, Motz 2016, 79; Herzlinger, Grosman 2018, 3-5).

1.3. Its practice in archaeology

Geometric morphometrics has primarily been used in evolutionary biology for studies regarding shape variability between and within groups. In archaeology it is frequently used for the study of lithic tools, defining cut marks and to describe shape variance in different assemblages. Recently the same is been done for ceramics (Selden Jr, Perttula, O'Brien 2014, 64) but figurative art is an understudied field. Until now only a couple of studies has been carried out on figurative art.

1.3.1. Anthropomorphic figurines from Mexico

In this study, anthropomorphic figurines from Teotichuacán-Mexico, which portray humans are examined using morphometry to see if there is a connection between the artistic production (since there is archaeological evidence of different levels of specialization), the time frame and space (Buxeda I Garrigós, Gordaliza 2011, 4). A total of 39 figurines are analysed, from whom the context is either unknown or from the Feathered Serpent Pyramid (150-250 AD) (Buxeda I Garrigós, Gordaliza 2011, 5). To reduce the total number of landmarks and the matrix (figure 21), two different case studies are made: one where the general appearance is been studied and another where only the shape of the face is observed. The two matrices used for EDMA are respectively 39 x 28 (with landmarks 3, 4, 5, 9, 17, 19, 23, 26) and 39 x 21 (with landmarks 5, 6, 8, 9, 10, 11, 13).

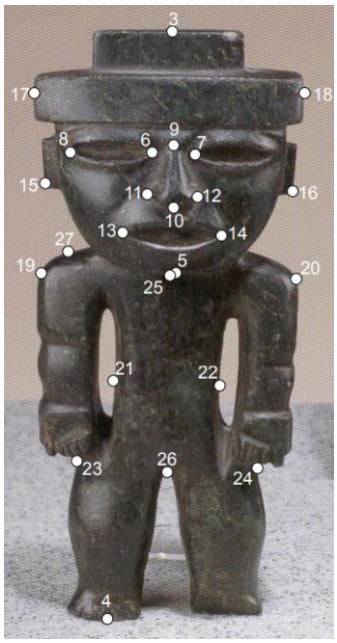

Figure 21: The used landmarks codes (Buxeda I Garrigós, Gordaliza 2011, 7, Fig. 3).

To visualize the dataset evenness graphs and clusters are created. Evenness compares the degree of uniformity in a population. This means when the evenness increases the diversity or variation in shape increases as well. Figure 22 shows the two evenness graph plotted for the general appearance (left) end the face (right).

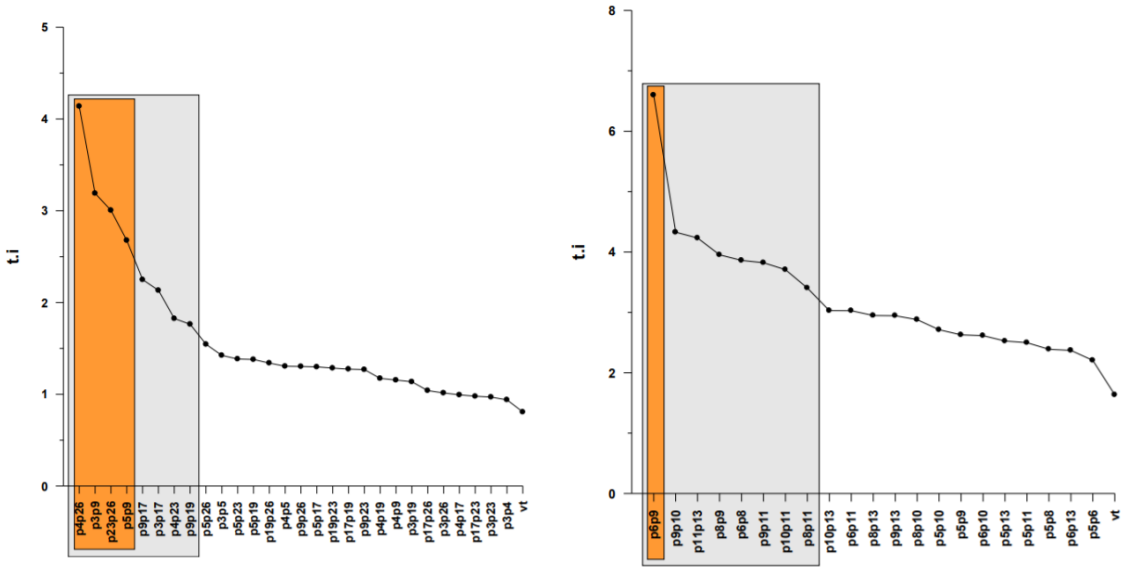

Figure 22: Two evenness graphs (Buxeda, Garrigós, Gordaliza 2011,14-16, Fig. 9 and 12).

In the case of the general appearance 8 out of 28 (orange and grey marking) are responsible for the total variation. When comparing this graph with the graph of the face it is visible that the second graph shows a greater influence of the variation between the different objects (Buxeda I Garrigós, Gordaliza 2011, 13;15).

From this data cluster analyses were performed, the results are shown in figure 23 with the dendrogram of the general appearance on the left and of the face on the right.

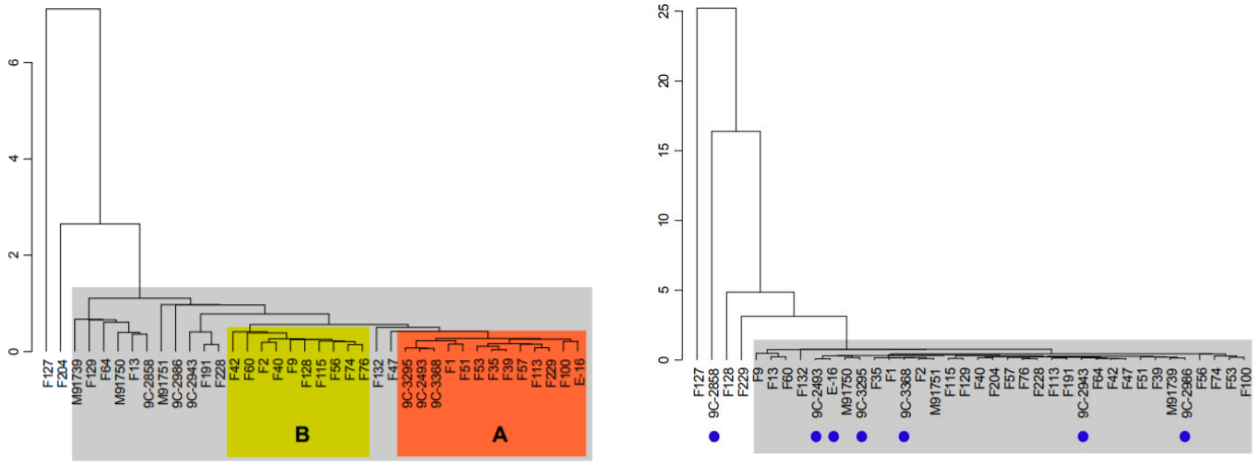

Figure 23: Two dendrograms (Buxeda, Garrigós, Gordaliza 2011,15-17, Fig. 10 and 13).

As shown in figure 23, the dendrogram of the general appearance contains two groups (A and B). When looking at the different objects it can be seen that there is a main distinction between the first two objects (F127 and F204). Object F127 comes from the Museo Nacional de Antropología de México, whereas object F204 is located in the Israel Museum of Jerusalem. The dendrogram of the face landmarks shows a different configuration. 35 objects show a somewhat higher similarity with one another, but four shows rather distinct character: F127, 9C-2858, F229 and F128. Another observation made by the researchers is the distribution of the figurines with a possible provenance of the Feathered Serpent Pyramid (blue dots on the dendrogram). These objects are more dispersed, but since these objects are quite small, the researchers think their height might be a limitational factor and this more in the production rather than the coordinate system (Buxeda I Garrigós, Gordaliza 2011, 13;15).

This study is still an ongoing project, but so far the researchers believe that the differences in shape are related to different traditions ((Buxeda I Garrigós, Gordaliza 2011, 18).

1.3.2. Terracotta figurine with Down syndrome-Mexico

A terracotta figurine from the Tolteca culture (Mexico) is studied by Starbuck in 2014. The facial morphology of this figurine appears to have a close approximation with Down syndrome or trisomy 21. By using geometric morphometrics based on 24 landmarks, the facial appearance of the figurine is compared with those of Down syndrome (images of 32 individuals of different origins and sex) and those of without Down syndrome or euploid (images of 32 individuals of different origins and sex) (Starbuck 2014, 500).

Three types of analysis are practised on these three groups: EDMA, PCA and principal coordinates analysis (PCOORD) all with an 85%-confidence interval, where a significant result relates to dissimilarity between the landmark configuration and no significant result relates to a resemblance of the landmark configuration.
EDMA is applied to search for similarities in facial morphology between the three sample groups. A total of 276 linear distances are used for this analysis. The following results are obtained (Starbuck 2014, 501; 503):

Table 2: the significance of two groups.

	Down syndrome – euploid	Figurine - euploid	Figurine – Down syndrome
Significance	Present	Present	**Failed**

PCA is applied to investigate what combination of linear distances is best used for a higher separation between the different groups. The results are that larger distances correlated with positive correlations and lower distances with a negative one. The PC's are visible on figure 25, where the circles represent the 85% confidence interval of either the euploid sample group or the one of Down syndrome. figure 25A shows the form analysis of PC1 and PC2 and describe 40,6% of the shape variance. Even though both confidence intervals overlap the figurine lies **within** those of Down syndrome. B shows the form analysis of PC2 and PC3 and describe 30,5% of the shape variance. Again both confidence intervals overlap but the figurine lies **within** those of Down syndrome (Starbuck 2014, 501-503).

In general, PC1 tells more about variation in the width of the face and nose and elevation of the eyes, lips and bridge of the nose (figure 24C), PC2 gives more information about changes in the lower part of the nose, the height of the lips and the width of the face (figure 24D). PC3 informs more about the variance in chin width and height and is a more vertical profile of the face (Starbuck 2014, 502-503).

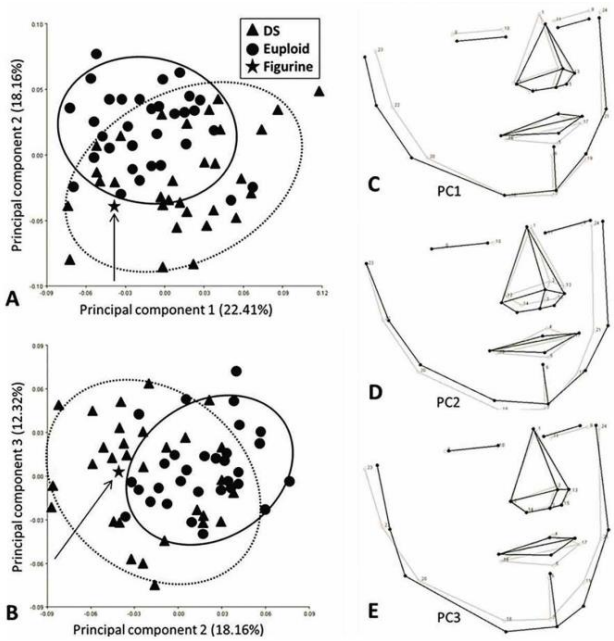

Figure 24: PCA results from the three groups (Starbuck 2014, 504, Fig. 3).

PCOORD is an extension of EDMA and used to localize highly differentiated facial linear distances. Axis 1 represents the variation describes for PC1, axis 2 for PC2 and axis 3 for PC3. Figure 25A describes 36,7% of the shape variations and while the two sample groups overlap, the figurine is located in the region of variations related to Down syndrome. Figure 25B describes 31,3% of the shape variations, the figurine is located outside both sample groups but is closer to those of variations related to Down syndrome (Starbuck 2015, 503-505).

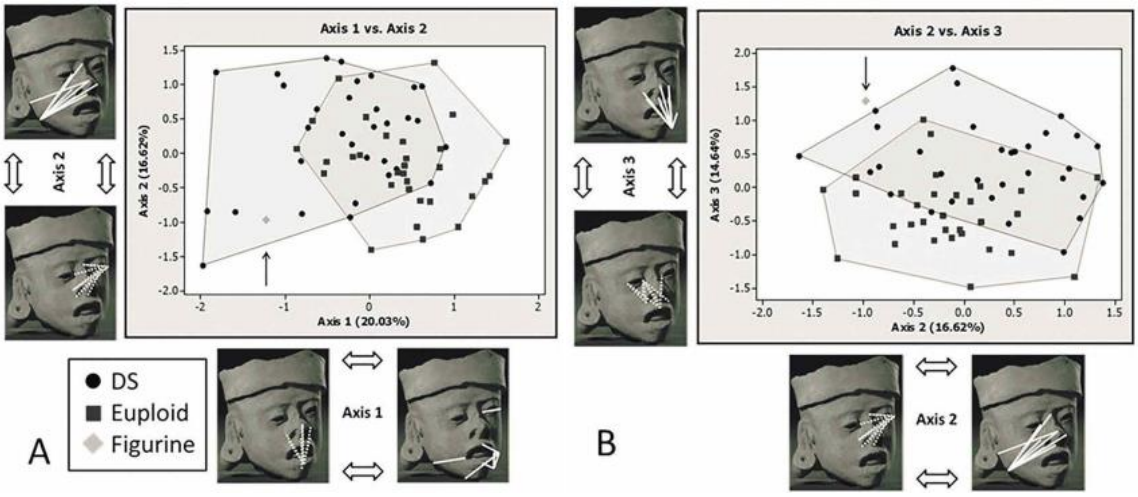

Figure 25: The PCOORD analysis of the three groups (Starbuck 2014, 505, Fig. 4).

Based on these three different types of analysis the figurine represents a person with Down syndrome. If this was the intention of the sculptor is a different story and possibly unanswerable because it depends on many factors such as social structure, religion, artistic view, skill, etc. (Starbuck 2014, 506-507).

1.3.3. Clay figurines-France

In the study of A. Bourdeu and D. Pitzalis (2010, 25-29), 29 faces of white clay figurines of Gallo-Roman origins from five locations in France (Alise-Sainte-Reine, Laignes, Saint-Pourçain-sur-Besbre, Vichy and Toulon-sur-Allier) are analysed with GPA and PCA to evaluate the correlation between these figurines. The results have shown that some faces appear to be a close resemblance with one another, especially between Laignes and Alise-Sainte-Reine (figure 26).

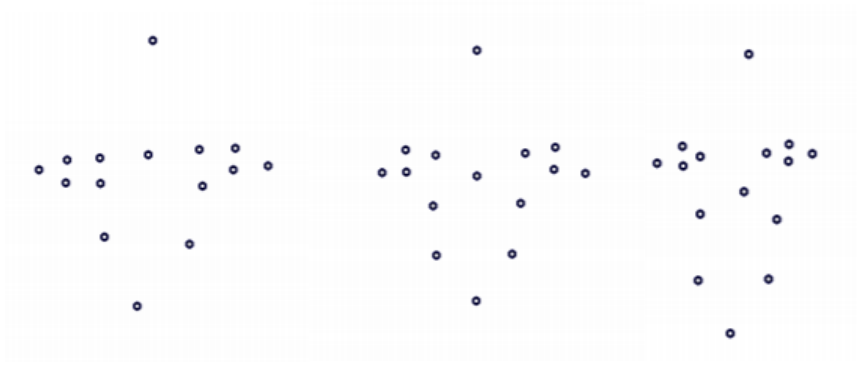

Figure 26: the mean configuration of Alise-sainte-Reine (left), Toulon-sur-Allier (middle), Vichy (right) (to: Bourdeu, Pitzalis 2010, 31, Fig. 8).

1.3.4. Rock art-Australia

Cobden et al. (2017, 96; 98;106) tried to identify extinct megafauna through rock art by using landmarks located on the beak. They used three species for their study: the emu, the magpie goose and *Genyornis newtoni*. The rock art is located in Arnhem Land in the northern part of Australia. A combination of landmarks and semi-landmarks were applied and analysed with GPA, PCA and canonical variations. As a result, the rock art matches more with the anatomical features of *Genyarnis newtoni*.

It is clear that for figurative art a lot more studies need to be done, but it has potential especially for the study of repeatability in symbology, usage of the same stamp or mould or variance within and between groups.

2. Shape descriptors

Shape descriptors are algorithms which represent a shape. They can describe the contour (boundary points), the region (interior points), 2D images and 3D models. There are a lot of classifications present in the literature: global, local, structural, statistical, graph-based, distribution-based, view-based etc. It is not possible to explain every type of shape descriptor. The following literature can be used as additional information:

- 3D Shape Analysis by Hamid Laga, Yulan Guo, Hedi Tabia, Robert B. Fisher and Mohammed Bennamoun (2019);
- Digital Image Processing. An Algorithmic Introduction Using Java by Wilhelm Burger and Mark J., Burge (2016);
- Document Image Analysis. Current Trends and Challenges in Graphics Recognition by K.C. Santosh (2018);
- Survey on 3D Shape Descriptors by Lisha Zhang, Manuel João da Fonseca and Alfredo Ferreire (2004);
- Comparative analysis of shape descriptors for 3D objects by Graciela Lara López, Adrianna Negrón, Angélica Jiménez, Jaime Rodríguez and Ricardo Paredes (2017).

In the following part, only the shape descriptors used in archaeological context will be explained.

2.1. Theoretical principle

A shape descriptor is generated by applying a certain mathematical equation onto a shape signature. These shape signatures represent unique areas or outlines. Possible examples are curvature, centroid distance, eccentricity, central moments, area, bounding box, etc.

2.1.1. Spherical harmonics transform

Since certain objects have a more complex outline spherical harmonics transform descriptors can be used. An example is already explained in geometric morphometrics (Fourier).

2.1.2. 3D Hough transform descriptor (3DHTD)

The 3DHTD relies on the accumulation of points in a set of planes located in a 3D space. Each plane is characterized by a triplet (s, θ, φ), where s is the distance from the plane to the origin of the coordinate system, θ is the azimuth (= the angle between the vector and a point perpendicular onto a reference plane in a spherical coordinate system) and φ is the angle of the elevation. It detects profiles by using different algebraic functions or in a more basic version lines and circles (Zhang, João da Fonseca, Ferreira 2004, 17; López et al. 2017, 7003).

2.1.3. Scale-invariant Feature Transform (SIFT)

SIFT is a region-based feature descriptor and takes the internal and outline information in account. The object will be divided into smaller key local feature vectors (significant for the object). These local feature vectors are called SIFT keys. They are used to identify possible similar points on other images (Kazmi, You, Zhang 2013, 4-5; López et al. 2017, 7011).

2.2. Advantages and limitations

Shape descriptors are a fast way of recognizing patterns between different objects, but they are quite complicated (López et al. 2017, 7003). Another approach might be to invest in deep learning or machine learning where a computer works with certain algorithms (see further).

2.3. Its practice in archaeology

The main application of these descriptors is to find similar elements in a large dataset. By doing this it can be possible to detect continuities of decorative elements or style in different context and information about chronology and trade networks might be recovered. It does not always mean that there is a connection. Additional analysis such as textual sources and archaeological excavation reports needs to be consulted before making conclusions.

2.3.1. Decorative elements on ceramic-unknown

Hough transform is used in a study of Romanengo, Biasotti and Falcidieno (2020) to analyse geometric decorative elements. The Hough Transform for a geometrical petal is (Romanengo, Biasotti, Falcidieno 2020, 406):

$$\rho_p = A + B \cos 2\pi \varphi_p$$

Where:

- ρ_p and φ_p are polar coordinates;
- A and B are real numbers.

This six-petal shape is used on different samples (figure 27) and in result, four fragments show a similar stylistic character (Romanengo, Biasotti, Falcidieno 2020, 410).

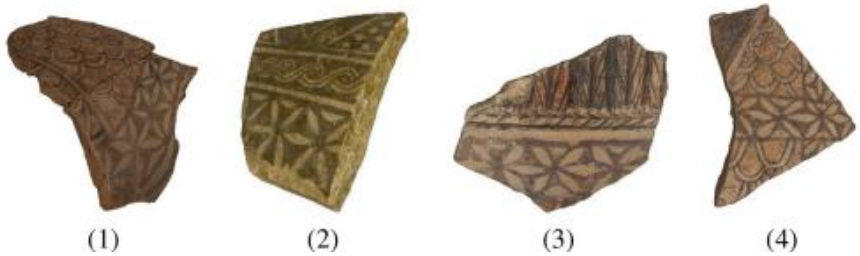

Figure 27: Similar stylistic characters between four fragments (Romanengo, Biasotti, Falcidieno 2020, 411, Fig. 12a).

2.3.2. Terracotta fragment-Salamis

In the study of Torrente, Biasotti and Falcidieno (2016), Hough Transform is used in the identification and comparison of the eyes and lips between different statues. As a reference a scanned terracotta fragment of Salamis from the STARC archive (Torrente, Biasotti, Falcidieno 2016, 5).

The point cloud of the eye (figure 28) is largely fitted with the best algebraic equation, in this case, a geometrical petal with equation (Torrente, Biasotti, Falcidieno 2016, 8):

$$y = a + b \cos^{2n}\theta$$

Where:

- a, b: the coefficients;
- n: the integer number;
- θ: the angle.

Here b is equalized to -a and a cartesian equation is passed and elaborated along the x-axis since most eyes are longer in the length. The Hough transform descriptor is then (Torrente, Biasotti, Falcidieno 2016, 8):

$$g(x, y) = (cx^2 + y^2)^{2n+1} - a\,[(cx^2 + y^2)^n - c^n x^{2n}]^2$$

Where:

- c: positive real coefficient.

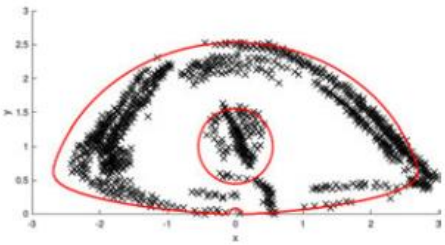

Figure 28: The refitted shape of the eyes and lips (Torrente, Biasotti, Falcidieno 2016, 11, Fig. 11a).

The following step is the extraction of the fitted curves and corresponding parameters from a different set of eyes and lips from fragments of both STARC and Shape Repository. These parameters can then be compared to see which artefacts have high similarity. The results are given in the following table (Torrente, Biasotti, Falcidieno 2016, 12):

Table 3: The parameters of the equation of different fragments.

Artefact	Radius	n	a	c
Reference	0,55	78	2,5331	0,8162
A-right	3,633	NA[1]	31	0,23
A-left	3,661	NA	30	0,23
B-right	NA	50	308,25	1,4484
B-left	NA	50	245	0,7503
C-right	NA	45	1115	0,6738
C-left	NA	45	993	0,7334
D-right	NA	75	3,12	0,5855
D-left	NA	75	3,05	0,8306
E-right	0,3	75	1,08	0,6675
F-right	NA	75	1,08	0,7141

[1] Not applicable

Figure 29 shows the different artefacts and their representative Hough transform:

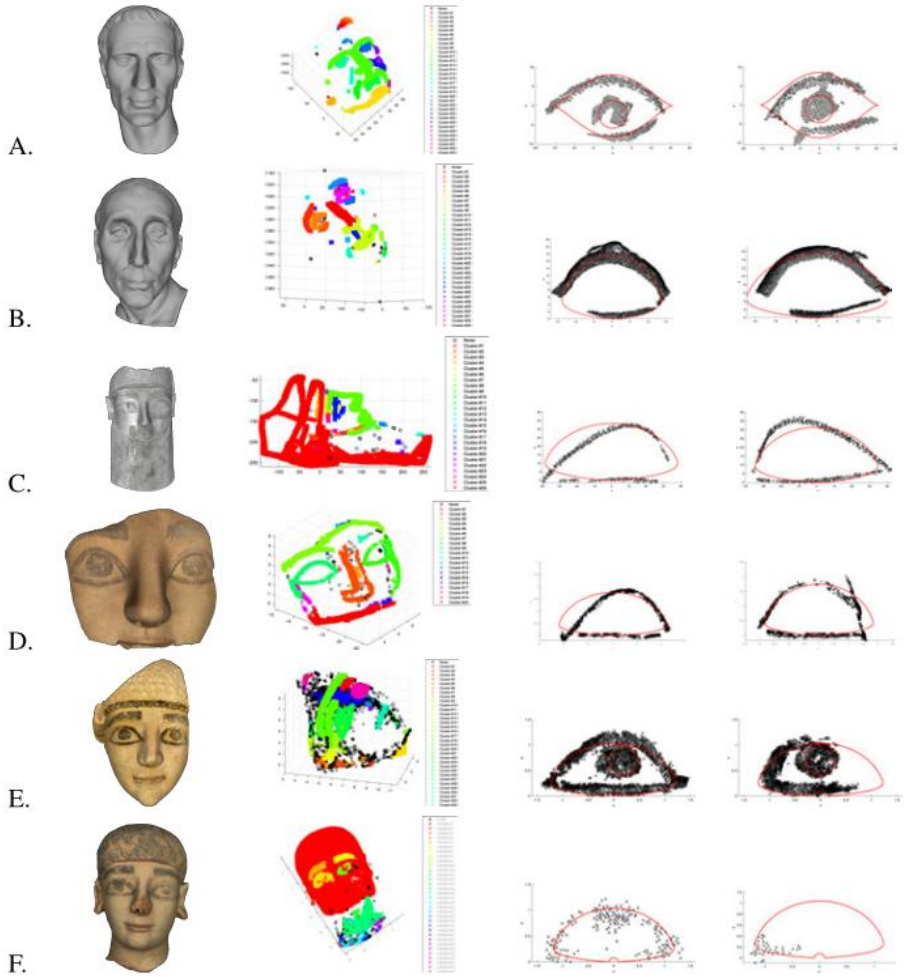

Figure 29: The contours of the eyes of different artefacts (Torrente, Biasotti, Falcidieno 2016, 13, Fig. 12).

From these results the following assumptions can be made (Torrente, Biasotti, Falcidieno 2016, 12;14):

- The eyes of A are quite similar to each other;
- The eyes of E and F are almost the same, which might tell something about the used style;
- The eyes of the reference sample and D show a small difference.

3. Machine learning

3.1. Theoretical background

Machine learning is a form of artificial intelligence. By training the data the machine or software can predict trends or classify objects into different categories. There are numerous models, but those used for a pattern or object registration are based on artificial neural networks (deep learning) and support vector machines. There are many types of machine learning and deep learning algorithms but the convolutional neural network (CNN) is the best and frequently used for archaeological purposes.

3.1.1. Artificial neural network

Artificial neural network (figure 30) consists of three layers: input – hidden – output. The input layer contains images with a set of pixels (width x height). Each pixel serves as an input for the neurons of the input layer (X_n). The connection of the input layer with the first hidden layer has a certain weight. The input of these neurons corresponds with a certain bias (= (X_1 x weigth$_1$ + X_3 x weight $_3$) + B_1) and an activation function determines on this number whether or not the neuron will be activated. This continues until the output layer and is called forward propagation. Weight and bias determine the accuracy of the result. To improve the accuracy of the network a process called training is applied, by using a lot of references until the error on the score in the output layer is as low as possible (Kim 2017, 19-33; Lecoutre, Negrevergne, Yger 2017, 332-334).

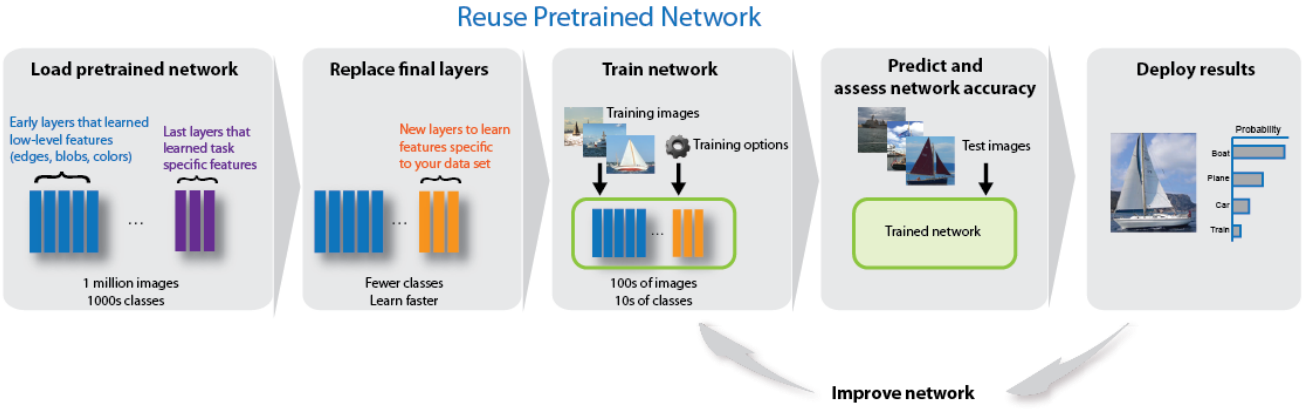

Figure 30: the pipeline of neural networks (MathWorks 2020, Train Deep Learning Network, s.d.).

3.1.2. Convolutional neural network

CNN (figure 31) does not differ much from artificial neural network. It consists of an input layer, a convolution layer, an activation layer, a pooling layer and the output layer. When studying an image as an input layer, the different neurons of the convolutional layers contain filters or kernels of learnable weights and biases (matrices) of local features (for instance a bird). Each filter or kernel detects the image for this bird and creates feature maps. The more filters are used the higher-levelled features are produced (so at the first level only the contour is detected and by the end the feathers and details). As with the artificial neural network, only some neurons will be activated. This is done by ReLU (Rectified Linear Activation function). This is a non-linear function and dismisses all negative values located in the feature map (normalizes the 3D models = invariant to rotation and size). Afterwards, a pooling layer is used (which has the same application as a PCA) to reduce the dimensionality, to clear the data of noise and focuses on the relevant patterns. This step is important to reduce the processing time. These three steps are repeated (with other data) so that fewer errors are obtained in the final step. To make neural understand the pattern and classify them into different categories a fully connected layer is attached at the end of the network and gives a score. The higher the score the more it relates to a certain category. Examples of CNN-networks are VGG-16, VGG-19 and Alex Net (Bengio, Goodfellow, Courville 2015, 297-308; Kim 2017, 124-130; Li, Zeng, Gong 2019, 51; 53; Kanaan, Behrad 2020, 346).

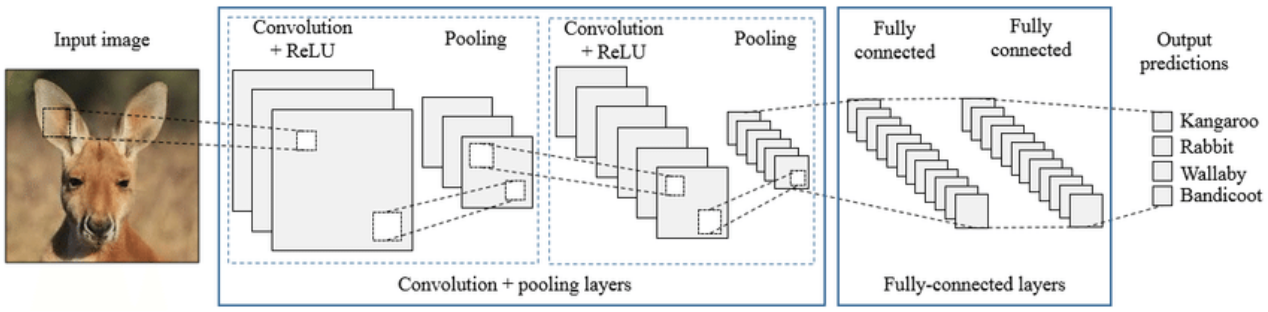

Figure 31: the pipeline of CNN (Nguyen et al. 2017, 43, Fig.3).

3.2. Advantages and limitations

These algorithms can be used to recompose missing parts of statues or paintings and can even be used with other methods such as shape descriptors, mineral identification and profilometry (Elgammal et al. 2018, 2187; Mantovan, Nanni 2020, 36; Zeng, Gong, Zeng 2020, 159). Both images as point clouds can be used as input data (Grilli, Özdemir, Remondino 2019, 448)

Besides the many potentials of certain algorithms there are some pitfalls:

- This type of artificial intelligence needs a good processor which can handle large dataset and this comes at a price;
- CNN works only when small datasets are used;
- To train such a neural network can take hours even months (DiLudovico 2018, 95; Li, Zeng, Gong 2019, 53; Kanaan Behrad 2020, 345).

3.3. Its practice in archaeology

3.3.1. Cylinder seals-different locations

In the study of di Ludovico (2018) artificial neural networks and hierarchical classification algorithms (based on textual data) are used to classify scenes from 425 cylinder seals. Reference points are chosen so that their understanding is not questionable, here the first figure and inscription line. The other elements are described by their characteristics and spatial relationship in the form of labels (di Ludovico 2018, 92). The distribution of the geographical contexts is given in figure 32, wherein the left diagram the unknown site is integrated.

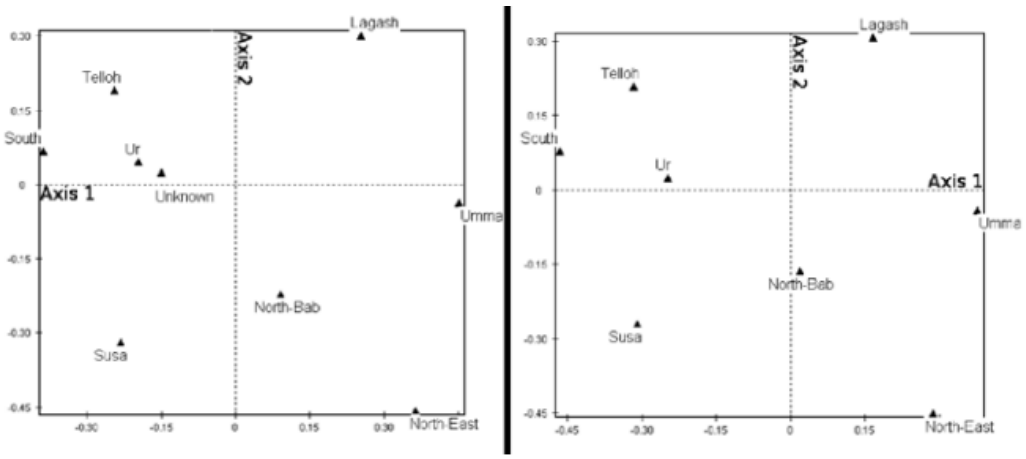

Figure 32: Distribution of the different sites based on toponyms (di Ludovico 2018, 99, Fig. 3.3).

Axis one corresponds with the treatment, while axis two is about the chronological differences. For example the scenes of the seals from Ur, Telloh and South depicts more iconographical elements of earlier periods (throne, hairstyle and divine headgear) (di Ludovico 2018, 100).

III. Thermal methods

In this chapter, the method for analysing the thermal property of an object will be explained.

1. Thermal imaging methods

Thermal imaging also known as infrared thermography (IRT) detects the transmitted temperature at the (sub-)surface of an artefact or organism. For artefacts, it is possible to locate connection points or small adaptations in the finishing process of mostly metalworking, but inhomogeneities or defects can be detected in other types of materials too. As well as with most morphological methods has this method a non-destructive character (Orazi et al. 2018, 1; Orazi et al. 2019, 116).

Thermal imaging is most often used in a military context (surveillance) and in the study of human and animal's body temperature (figure 33) because warm objects (with colours purple to yellow) are distinguishable from their colder background (green to black colours) or vice versa and healthcare (cancer or inflammation). In the cultural sector, It is widely used for conservation of paintings and buildings (Živčák et al., 2013, 7-29; Soroko M., Howell K., 2018, 90; Zhang et al. 2019, 64-65).

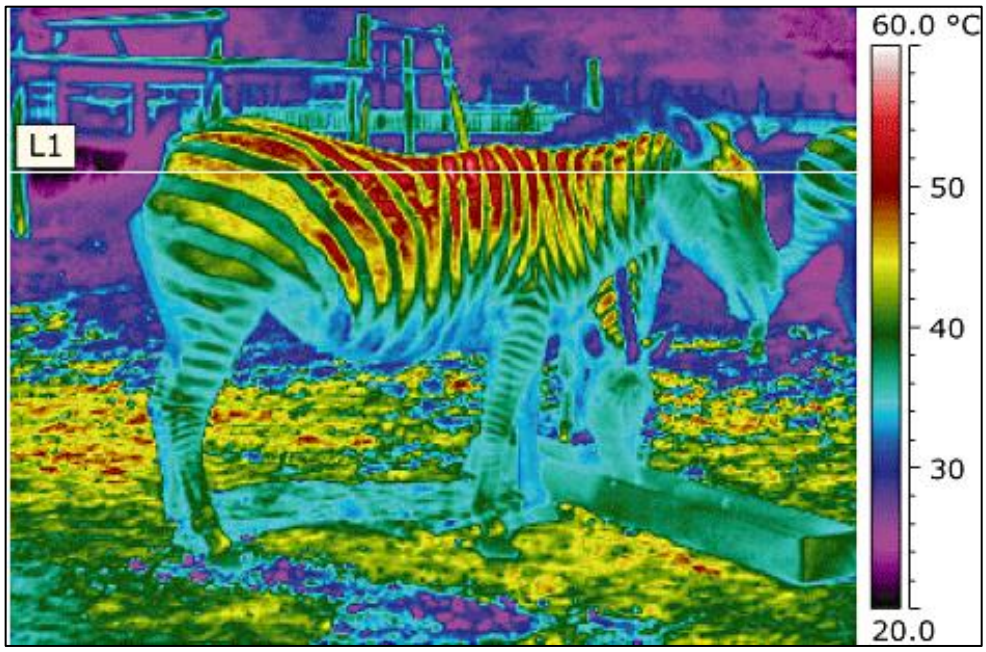

Figure 33: An example of a thermal infrared image (McCafferty 2007, 208, Fig.1).

1.1. Theoretical principle

IRT is a photothermal technique based on the thermal transport properties or heat diffusion of the studied artefact, were at the end of the process the emitted distribution of the IR radiation occurring at the surface will be recorded with an IR camera. This emitted IR energy will be converted to their respective temperature and images (figure 33) of these temperature gradients are created (Mercuri et al. 2018a, 54; Orazi et al. 2018, 2; Orazi et al. 2019, 116). Noticeable on figure 2 is that IR is not visible for the human eye because it has longer wavelengths (0,78 µm to 1 mm) than visible light (400 – 750 nm) and is EM radiation.

To evaluate the thermal transport properties of the artefact, the object's natural temperature is analysed, called passive IRT, or the artefact will be subjected to an external thermal stimulus, called active IRT. Any kind of light source can be used for the stimulation of thermal differences. Most often flashlights or lamps are used, but natural sources such as the sun or acoustic waves will suffice as well. Radiant heat sources are used cause they are restricted to a certain wavelength range and they have a low energy level so atomic bonding cannot break (Di Tucchio 2015, 1; Hidalgo-Gato et al. 2015, 192, 1; Mercuri et al. 2018a, 54; Orazi et al. 2018, 2; Orazi et al. 2019, 116).

Optical IRT (figure 34) is frequently used in archaeology and therefore the focus of this chapter. There are three ways of heating the object can be applied. Either the thermal wave is induced by a short pulse (pulsed thermography), by a continuous wave (step heating thermography) or by a periodic wave (lock-in thermography). With active IRT different heat transfer mechanisms have an important influence: heat radiation or thermal emission, heat convection and heat conduction.

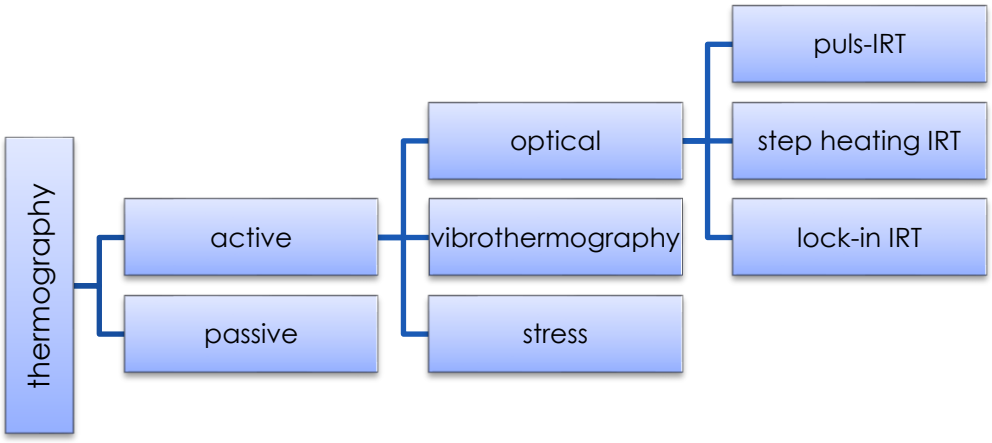

Figure 34: Diagram of thermography

When an energy source is used (natural or induced), the molecules in the surface of the artefact absorbs the light, which establishes a shift in their rotational and vibrational movements. The higher the temperature, the faster their movements will be and the infrared energy can be absorbed, transferred or emitted (Figure 2). In case of a blackbody, the absorbed and re-emitted energy is kept at a thermodynamic equilibrium. This is explained by Max Planck. In the following equation the relationship between the spectral radiance emittance of a blackbody and the wavelength for a certain temperature (Živčák et al., 2013, 46; Morello De Capua 2016, 27; Sfarra et al. 2017, 5):

$$L(\lambda,T) = \frac{2\pi hc^2}{\lambda^5\left(e^{\frac{hc}{\lambda kT}} - 1\right)} \text{ (Watt per m}^2\mu\text{m)}$$

Where:

- λ: emitted wavelength (μm);
- T: temperature of a black body (Kelvin);
- h: constant of Planck = 6,62607 x 10^{-34} $\frac{m^2 kg}{s}$;
- c: speed of light = 299 792 458 $\frac{m}{s}$;
- k: constant of Boltzmann = 1,380 648 x 10^{-23} $\frac{Joule}{Kelvin}$;
- $2\pi hc^2$ = first radiative constant = 3,741 x 10^{-16} $\frac{Watt}{m^2}$;
- $\frac{hc}{k}$ = second radiative constant = 1,438 x 10^{-2} m Kelvin.

This means that the emission of the IR radiation is dependent of the initial temperature, and as well to the emissivity of the artefact and the thermal transport properties (and these are again dependent on the sub-surface features). Therefore it is important to know the emissivity or emitted energy of the studied artefact. This can be calculated with the following equation (Garrido, Lagüela, Arias 2018, 3):

Emitted energy[2] = 1 – transmitted energy – reflected energy

In case of a real body (such as the archaeological artefacts) the amount of absorbed and re-emitted energy differs, within result a low-energy emittance. This is described in the Stefan-Boltzmann law (Morello, De Capua 2016, 27; Sfarra et al. 2017, 5; Garrido, Lagüela, Arias 2018, 3):

$$E = \varepsilon \sigma T^4$$

Where:

- T: temperature of a real body (Kelvin)
- σ: constant of Stefan-Boltzmann = 5,6696 x 10^{-8} $\frac{\text{Watt}}{\text{m}^2\text{K}^4}$
- ε: emissivity
- E: radiated energy of a real body (Watt m²)

A last important parameter of the thermal properties of an object is thermal diffusivity. Thermal diffusivity is related to the transfer of heat in material and therefore to the density, specific heat capacity and thermal conductivity of the material. Thus in general, it is variant to the thermal, geometric (thickness, curvature) and optical (reflectivity) parameters (Scudieri, Mercuri, Volterri 2001, 309; Mercuri et al. 2017a, 200):

$$D = \frac{k}{\rho\, c}$$

Where:

- D: thermal diffusivity ($\frac{m^2}{s}$);
- k: thermal conductivity ($\frac{W}{mK}$);
- ρ: density ($\frac{kg}{m^3}$);
- c: specific heat capacity ($\frac{J}{kg\ K}$).

[2] According to Kirchhoff's law

To understand the influences of D and its parameters a **homogeneous** sample is considered. When this sample has a finite thickness and absorbs light uniformly at the surface (x = 0) an one-dimensional (1D) heat diffusion equation can be solved (Scudieri, Mercuri, Volterri 2001, 309; Mercuri et al. 2017a, 200; Mercuri et al. 2017c, 3; Orazi 2020, 283):

$$\Delta T\ (x, t) = \frac{Q}{e} \cdot \frac{\sqrt{D}}{L} \cdot \left[1 + 2 \sum_{n=1}^{\infty} \cos\left(\frac{n\pi x}{L}\right) \exp\left(-\frac{n^2\pi^2}{L^2} Dt\right)\right]$$

Where:

- ΔT = temperature changes (K);
- x = depth (m);
- t = time (s);
- Q = absorbed heat per surface ($\frac{J}{m^2}$);
- e = thermal effusivity = $\sqrt{\rho k c}$;
- L = thickness (m).

The configuration of the set-up makes it possible to detect the change in temperature and thermal diffusivity. When the heating source and detection system both are on the same side of the object the reflected thermal wave is higher in temperature at the location of a defect (called front face heating mode). When the heating source is positioned at the opposite side of the heating source, the transmissive thermal wave is lower in temperature at the location of a defect (called rear face heating mode) (Castelli et al. 2017, 52; Yao et al. 2018, 144).

A qualitative result is obtained by thermograms. These are the visual representations, where a darker or colder colour usually corresponds with a low temperature and a brighter or warmer colour with higher temperatures. Besides the visual image, the local IR energy represented as a relation between the temperature signal and time can be studied as well. This is useful to make an assessment on the used repairing method and even tell whether or not the sample bears subsurface inhomogeneities or different compositions of alloys are present. These repairs are necessary when there is a fault in the casting (in case of bronze) such as porosities when the metal sets back in or when air is present and cracks due to thermal stress. Repairs can consist of a mechanical plug, fillings or patches. On figure 35 two types of behaviours are shown. Either the

sample is homogeneous and overlaps with the $t^{1/2}$ or the sample is inhomogeneous and forms a shoulder-like profile. This is also the result of residual air (Ibarra-Castanedo et al. 2007, 10; Mercuri et al. 2011, 476; Mercuri et al. 2018b, 33; Mercuri et al. 2020, 4; Orazi 2020, 281-282).

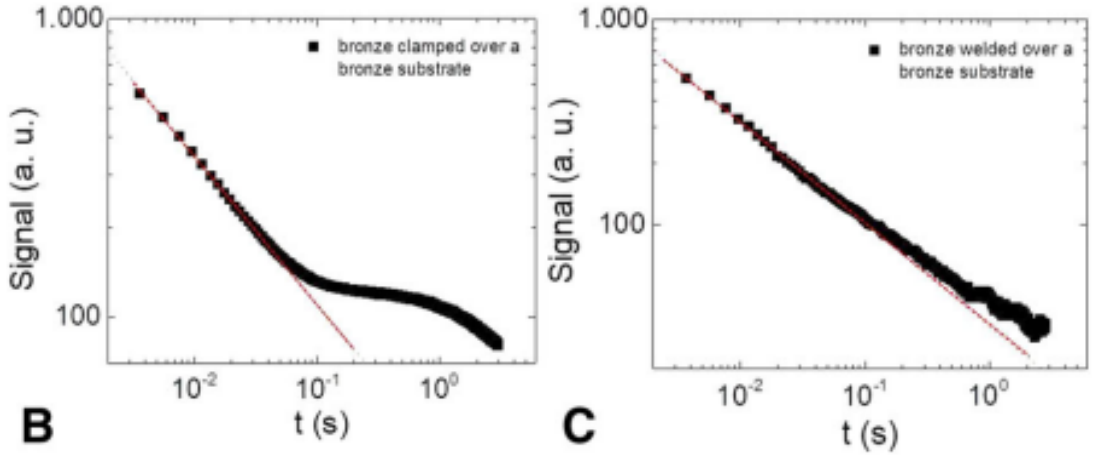

Figure 35: Thermographic signal time dependence with (left) a shoulder-like slope and (right) a similar slope as that of the half-life (red line) (Orazi et al. 2018, 4, Fig. 2B and C).

1.1.1. Pulsed IRT

Here short exposure times (milliseconds) of a high energetic light source are used to heat the object. After the pulse, the temperature will decay due to radiation and convection losses and diffusion. When a defect is present in the surface or subsurface an abnormal pattern of the temperature is formed and influences the thermal diffusivity (Hidalgo-Gato et al. 2015, 192; Sirikham et al. 2020, 2).

When in the 1D heat diffusion equation x is substituted 0 the solution for **front face heating** mode is retrieved, with the following equation as result (Mercuri et al. 2017a, 201; Mercuri et al. 2017c, 3; Sirikham et al. 2020, 2):

$$\Delta T\,(0, t) = \frac{Q}{e} \cdot \frac{\sqrt{D}}{L} \cdot \left[\, 1 + 2 \sum_{n=1}^{\infty} \exp\left(-\frac{n^2 \pi^2}{L^2} D t \right)\right]$$

To evaluate D or L in the front face heating mode, a double logarithmic plot (figure 36) is created where the relationship between the decay of the surface temperature and time is shown and calculated for a specific D and different L. Visible on this graph are two types of behaviours of the time-dependences, one at short time measurement and one at a longer time measurement. The former is defined by a slope line of $t^{-1/2}$

corresponding to the heat diffusion solution of a semi-homogeneous material (Scudieri, Mercuri, Volterri 2001, 310; Mercuri et al. 2017a, 201; Mercuri et al. 2017c, 3; Orazi 2020, 283; Sirikham et al. 2020, 2):

$$\Delta T\ (0,\ t)_{L=\infty} = \frac{Q}{e} \cdot \frac{1}{\sqrt{\pi t}}$$

The latter occurs when the heat diffusion 'hits' the opposite surface and further diffusion is prevented by poor thermal properties of air and a constant temperature is achieved (Scudieri, Mercuri, Volterri 2001, 310; Mercuri et al. 2017a, 201; Mercuri et al. 2017c, 3; Orazi 2020, 283):

$$\Delta T\ (0,\ \infty) = \frac{Q}{e} \cdot \frac{\sqrt{D}}{L}$$

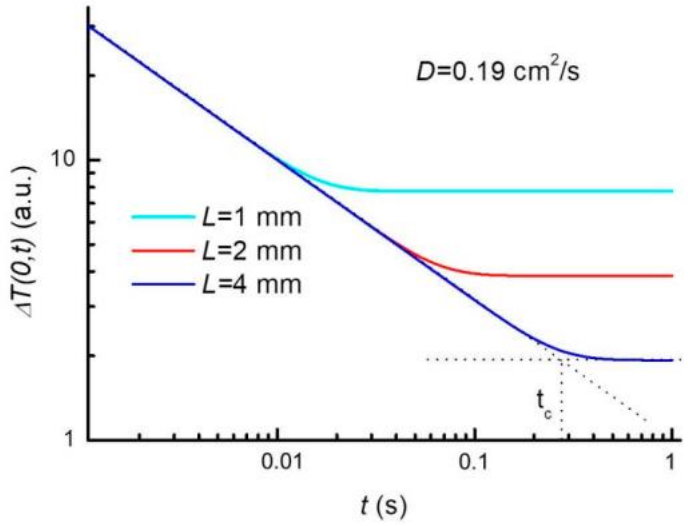

Figure 36: Log-log plot of temperature change over time (Mercuri et al. 2017c, 4, Fig. 1).

The transitional stage (in other words right before the equilibrium is reached) or t_c is related to D by the following equation (after combining the previous equations). In case D is known L can be calculated and vice versa (Scudieri, Mercuri, Volterri 2001, 310; Mercuri et al. 2017a, 201; Mercuri et al. 2017c, 4):

$$D = \frac{L^2}{\pi t_c}$$

When x is substituted by L the solution for the **rear face heating** operation mode is obtained with the following equation (Mercuri et al. 2017c, 4):

$$\Delta T\ (L,\ t) = \frac{Q}{e} \cdot \frac{\sqrt{D}}{L} \cdot \left[\ 1 + 2 \sum_{n=1}^{\infty} (-1)^n \exp\left(-\frac{n^2 \pi^2}{L^2} Dt \right)\right]$$

To evaluate D or L in the rear face heating mode, a semi-logarithmic plot (figure 37) is created where the relationship between the normalized transient temperature rise and time is shown and calculated for a specific D and different L (Mercuri et al. 2017a, 200; Mercuri et al. 2017c, 4; Orazi 2020, 283).

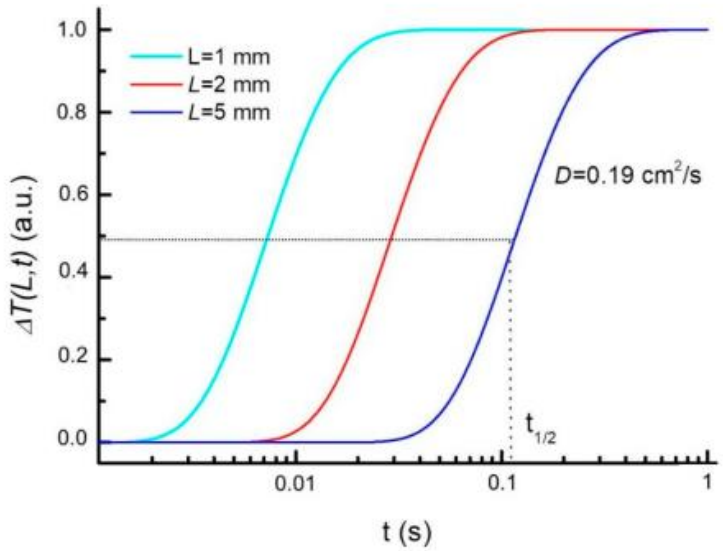

Figure 37: Semi-logarithmic plot of temperature change over time (Mercuri et al. 2017c, 5, Fig. 2).

D can be measured when the temperature reaches half of its maximum value ($t^{1/2}$). Again in case D is known L can be measured or vice versa (Mercuri et al. 2017a, 200; Mercuri et al. 2017c, 4; Orazi 2020, 283):

$$D = \frac{1{,}38L^2}{\pi^2 t_{1/2}}$$

The raw data obtained from the measurement phase needs to be processed. This can be done in several ways, with the most used explained below:

Pulsed phase IRT (PPT) converts the time domain data to frequency by using 1D discrete Fourier transform (DFT) or fast Fourier transform (FFT) based on lock-in IRT post-acquisition to increase the contrast of the defects and the amplitude and phase values can be calculated. When the phase value is known depth can be measured as well. This embraces the two advantages of both methods (Sfarra et al. 2010, 105; Garrido, Lagüela, Arias 2018, 6; Duan et al. 2019, 5)

Thermographic signal reconstruction (TSR) converts the time domain data to a logarithmic form of the 1D heat solution. On this double logarithmic function an polynomial function is fitted:

$$\ln(\Delta T) = a_0 + a_1 \ln(t) + a_2 \ln^2(t) + \ldots + a_n \ln^n(t)$$

Where:

- a: polynomial functions;
- n: degrees.

The number of degrees is related to the accuracy of the result (signal to noise ratio). Usually, five degrees are used (Bendada et al. 2010, 3; Sfarra et al. 2010, 105; Garrido, Lagüela, Arias 2018, 6-7; Sfarra et al. 2017, 6).

Principal component thermography (PCT) uses SVD to form empirical orthogonal functions (EOF) of the time-domain data. In general, the first few EOF's contains the necessary spatial variations and information about the internal defect. PCT can be used to quantify the depth of the defect as well (Sfarra et al. 2017, 6; Garrido, Lagüela, Arias 2018, 6; Duan et al. 2019, 6). Different types of PCT exist: Yousefi et al. (2017, 163) propose an alternative algorithm which gives PCT without calculating a covariance matrix, called candid covariance-free incremental PCT and is much faster. Wen et al. (2019, 2) and Yao et al. (2018, 14) uses edge-group sparse PCT to enhance the visualization of the defect by considering the spatial connectivity between pixel groups of the thermal images. Liu et al. (2019, 2-3) and Yao et al. (2018, 145) uses independent components to decompose thermal images into a set of information. By doing so the defect can be more focused, while the background and noise can be diminished.

High order statistics (HOS) calculates and maps four parameters of the distribution: the mean (average value), the variance (the spreading around the mean), the skewness (as the third central standardized moment measuring the asymmetry) and kurtosis (as the fourth central moment and representing the grade of flatness of the curve) and can be used to extract defects (Bendada et al. 2010, 3; Yao et al. 2018, 150).

1.1.2. Step-heating IRT

A continuous level (several seconds) of heat is generated at the back of the object, while an IR camera measures the temperature at the front of the object, both heating and cooling phase are of interest. A 1D heat diffusion equation is used where the temperature emitted for -non- ideal heat source (for example a halogen lamp, which needs more time to reach a constant intensity) at the front is expressed by (Bendada et al. 2010, 1; Orazi et al. 2015, 3; Mercuri et al. 2017a, 200; Li et al. 2019, 226):

$$T(0, t) = f_1 \left[f_2 t - \frac{1}{6} - p f_2 (1 - e^{\frac{-t}{p}}) - 2 \sum_{n=1}^{\infty} \frac{(-1)^n}{1 - n^2 \pi^2 p f2} \left[\frac{e^{-n^2 \pi^2 f2 t}}{n^2 \pi} - p f_2 e^{\frac{-t}{p}} \right] \right.$$

Where:

- f_1: $\frac{F0\ L}{k}$ and F_0 is the heat flux, L the thickness and k the thermal conductivity;
- f_2: $\frac{D}{L^2}$ and D is the thermal diffusivity;
- p: the necessary time of the heating source to elevate the temperature.

From this equation L and D can be calculated and vice versa.

Data processing methods are usually based on TSR.

1.1.3. Lock-in IRT

Here the surface will be heated in periodical timeframes by thermal waves, mostly sinusoidal waves. When a homogenous sample is measured, there will be no changes in phase or amplitude. In case of internal or subsurface "defects" the thermal wave will be reflected and interferes with the surface wave resulting in an oscillatory interference pattern. This can be explained by the following equation (Ibarra-Castanedo et al. 2007, 328; Mercuri et al. 2011, 477-478; Hidalgo-Gato et al. 2015, 193):

$$T(z, t) = T_0 \exp\left(-\frac{z}{\mu}\right) \cos\left(\frac{2\pi z}{\lambda} - \omega t\right)$$

Where:

- μ: thermal diffusion length (m) = $\sqrt{\frac{D}{\pi f}}$
- λ: thermal wavelength = 2πμ (m);
- ω: modulation frequency = 2πf ($\frac{rad}{s}$).

Depth can be measured when μ is known. The lower the frequencies, the deeper the measurement:

$$z = C_1 \mu$$

Where:

- C_1: constant = 1,82.

There are two ways of processing the data set to extract the amplitude and phase delay. The first one is a DFT, where real and imaginary modes of the transform are used:

$$F_n = \Delta t \sum_{k=0}^{K-1} T\,(k\Delta t)\, exp^{\frac{-j2\pi nk}{K}} = real_n + j\ imaginary_n$$

Where:

- n: frequency increment;
- Δt: sampling interval
- k: number of thermal images;
- K: total number of thermal images;
- j: imaginary number.

It is a slow process but applicable for any type of wave and de-noises the signal. The pixels are stored in a 2D-matrices, which is converted to a greyscale image or phase and magnitude image (Ibarra-Castanedo et al. 2007, 331; Chatterjee et al. 2011,655).

The second way is a four-point method illustrated in the following figure. This method is faster, but has a higher noise and is only applicable to sinusoidal waves (Ibarra-Castanedo et al. 2007, 330).

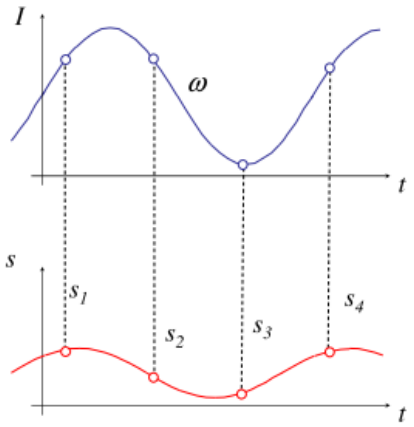

Figure 38: The four-point method, with the input signal on top and the response at the bottom (Ibarra-Castanedo et al. 2007, 330, Fig. 6).

The estimations for the amplitude and phase are given in the following table (Ibarra-Castanedo et al. 2007, 330; 331; Sfarra et al. 2014b, 3468):

Table 4: The estimations of the amplitude and phase for DFT and Four-points method.

	Discrete Fourier transform	**Four-points**
Amplitude	$\sqrt{real_n^2 + imagin_n^2}$	$\sqrt{(S1 - S3)^2 + (S2 - S4)^2}$
Phase	$\tan^{-1}(\frac{imagin_n}{real_n})$	$\tan^{-1}(\frac{S1-S3}{S2-S4})$

1.1.4. 3D-modelling and IRT

Thermal images and point clouds generated from 3D-modelling techniques (see next chapter) can be combined so that the geometric and thermal information is connected (figure 39). To combine both first a geometrical calibration to compute the intrinsic and extrinsic parameters is of order. Afterwards, the data can be fused by integrating several thermograms to the point cloud, aligning the point clouds by iterative closest point (ICP) and then placing both point clouds in the same reference system. The final point cloud consists of geometric accurate images with a texture map generated from the thermograms (Maset et al. 2017, 29-30; Barrile, Fotia 2018, 401; Campione et al. 2020, 3-10).

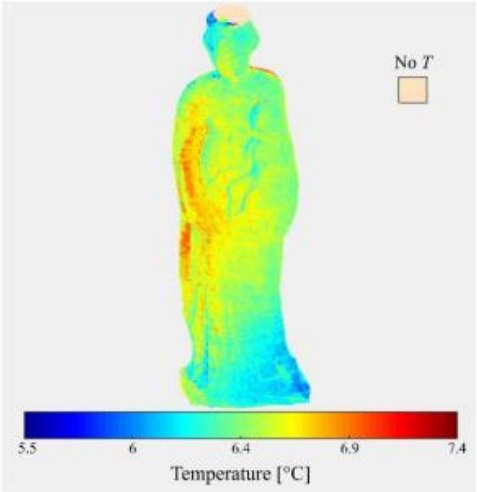

Figure 39: An example of a combined 3D model (Campione et al. 2020, 17, Fig. 17b).

In a recent study, thermal images are mapped straight onto a CAD file by a pose estimation technique and therefore not using any additional hardware or geometric calibration, whereas 3D scanners need them. To map 2D images on 3D models a pixel-wise posterior segmentation technique is applied. This technique can only be used when the contours of the object are visible, but in contrast to 3D scanners highly reflective surfaces can be detected (Sels et al. 2019, 153-154).

1.1.5. Multi -and hyperspectral imaging and IRT

When combining the advantages of IRT (detection of defects or voids, analysis of conservation, painting technique) with those of multi -and hyperspectral imaging (information on composition and drawings) a more exhaustive set of information can be gotten. The two images are taken separately from each other (Laureti et al. 2019a, 2-3; Laureti et al. 2019b, 2).

1.2. Advantages and limitations

The advantages of active IRT are its non-contact and non-destructive characteristic. Pulsed IRT is a rather fast method (few milliseconds), while lock-in and step-heating IRT needs several seconds. Wen lower frequencies are used, deeper measurements can be done (at cost of the resolution). It is affordable. Different areas can easily be detected and compared (Ibarra-Castanedo et al. 2007, 329; 338; Garrido, Lagüela, Arias 2018, 6; Li et al. 2019, 223).

The limitations of active IRT are the probability of eye damage with certain heat sources, the data processing methods are for pulsed IRT more difficult than for lock-in IRT, a lower spatial resolution for larger structures and in comparison with point clouds from 3D-modelling (Ibarra-Castanedo et al. 2007, 332; Barrile, Fotia 2018, 408; Garrido, Lagüela, Arias 2018, 6).

Using the technique with 3D-CAD-files there is no restriction in materials which is a problem when applying SL or LS (Sels et al. 2019, 156).

1.3. Its practice in archaeology

Active IRT is one of the few methods that can be used to analyse the manufacturing process, subsurface defect, damage or decay and details of the construction and composition of metal object, frescoes, wooden object, paintings, stone objects and others.

Active RTI implemented on stone or marble objects are mostly used to analyse their preservation state and analyses the presence of cracks and voids. Bronze statues have been analysed to gain more insights into their manufacturing process and repairs. Paintings or frescoes can be analysed to detect subsurface paintings, defects and to diagnose the state of the monument for conservation. Other applications are the decoration and pictorial elements of manuscripts (Mercuri et al. 2018a, 53), ceramic-coated materials (Duan et al. 2019, 2), glass and some smaller objects such as Phoenician earrings and rings and Roman coins (Mercuri et al. 2011, 480).

1.3.1. Nemrut Dağ Monument-Turkey

The Nemrut Dağ Monument is located in the province of Kahta-Adiyaman, Turkey. It is a combined monument consisting of two lion statues, the head of a king of Commagene, several gods and two eagles all made out of limestone and sandstone. They date from the first half of the first century BC and are built under Antiochus I (Tavukçuoğlu et al. 2011, 204). The sculptures are analysed to map the decay patterns (cracks) of the surface by IRT and ultrasonic testing (Tavukçuoğlu et al. 2011, 212; Tavukçuoğlu 2018, 4).

1.3.2. Ratto delle Sabine-Italy

The Ratto delle Sabine is a marble statue created by Giambologna in the second half of the 16th century in Florence. IRT is used to localize the higher risk areas (cracks) of the statue for eventual future restoration work. Since the statue is composed of different materials (clay, wood, metal, marble), different thermal properties were present (Di Tuccio et al. 2015, 2).

1.3.3. Three bronze statuary-Italy

Passive IRT is used to evaluate the influence of climate (by mechanical stress) of three bronze statuary (Marco Aurelia, Nettuno and Alessandro and Ranuccio Farnese) located in the open air of Rome (Orazi et al. 2020, 284).

1.3.4. Boxer at Rest-Italy

A Hellenistic Greek bronze, called Boxer at Rest is currently located at the Museo Nazionale Romani in Rome and is found in Rome as well. It is made by the indirect lost-wax technique, where afterwards different body parts are welded together. In general, the statue is constructed with an alloy composing of 76% copper,12% lead and 12% tin. Inlaid copper is used to highlighting the stress a boxer underwent (drips of blood, wounds) and some other details (stitches of the gloves, nipples and lips). The artist even used a different alloy (30% lead and 3% tin) to generate the effect of a bruise under the right eye (Mercuri et al. 2018b, 34; Orazi et al. 2019, 117; Mercuri et al. 2020, 6).

Different parts of the statue have been investigated with pulsed IRT. The bruise under the right eye shows (figure 40) brighter on the thermogram than its surrounding and is therefore warmer. The shoulder-like curve corresponds with a non-homogeneous composition due to the lead and tin and poor contact with the surrounding area (Mercuri et al. 2018b, 37; Mercuri et al. 2020, 2).

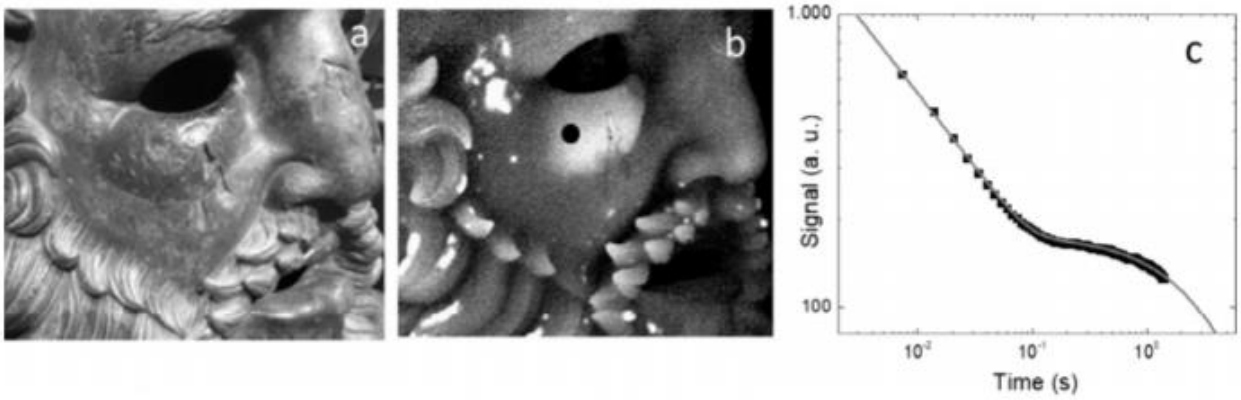

Figure 40: The thermograph of the right eye and its corresponding thermographic signal (Mercuri et al. 2018b, 37, Fig. 8).

The lips (figure 41) appears darker on the thermograph due to a lower emissivity. The curve is slightly non-linear. This tells that the lips were manufactured separately, applied mechanically and it has a different composition, but because there is just a small discrepancy the bond between the lips and the area underneath is very solid (Mercuri et al. 2018b, 38; Orazi et al. 2019, 118).

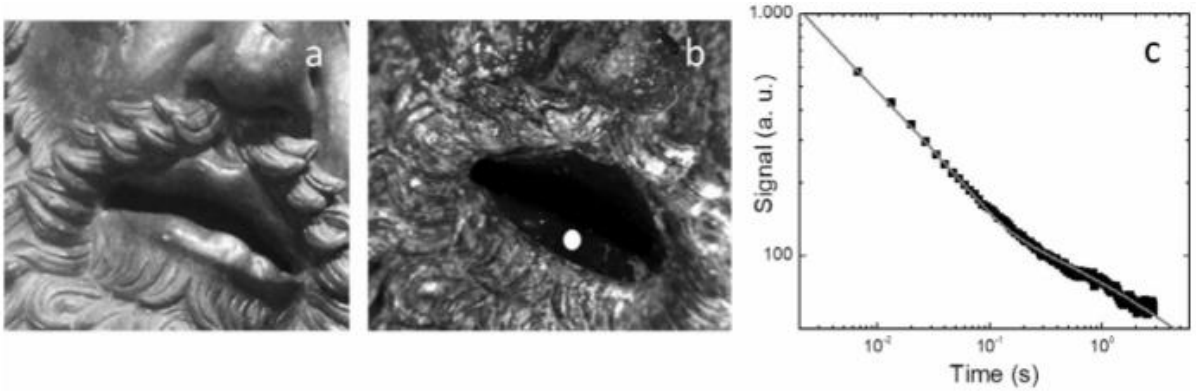

Figure 41: The thermograph of the lips and its corresponding thermographic signal (Mercuri et al. 2018b, 38, Fig. 10).

In the neck (figure 42) several brighter areas can be seen on the thermogram. These are mechanical repairs in the form of patches. The shoulder-type of graph corresponds with an inhomogeneous material used to create these patches. The defects were probably the result of a failure in the lost-wax technique (Mercuri et al. 2018b, 36; Orazi et al. 2018, 6).

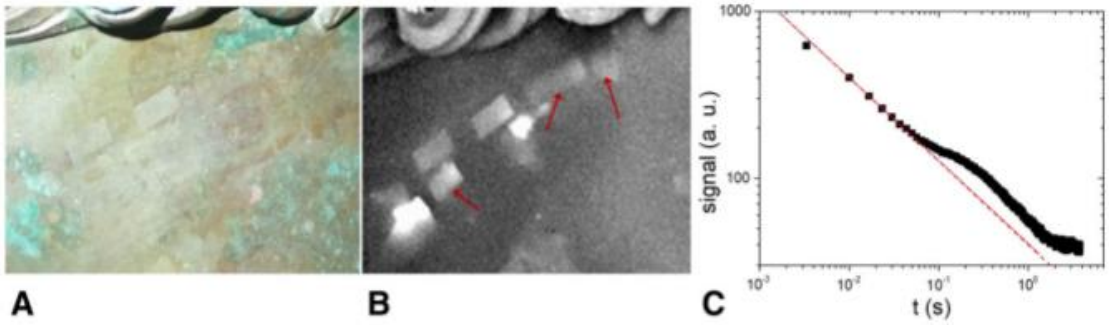

Figure 42: The thermograph of the neck and its corresponding thermographic signal (Orazi et al. 2018, 6, Fig. 7).

The left shoulder and back (figure 43) show the presence of small rectangular patches. Since there is no crack, the patches were probably used to mend surface porosities (Orazi et al. 2019, 118).

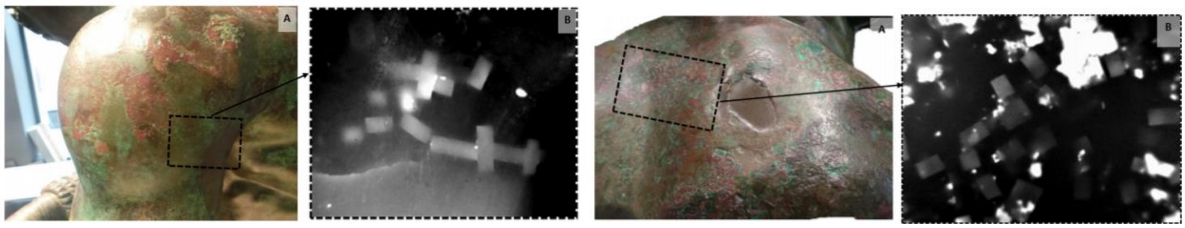

Figure 43: The thermograph of the left shoulder (Orazi et al. 2019, 117 and 119, Fig. 3A and B and Fig. 6A and B).

The left nipple (figure 44) appears darker in the thermogram and shows a shoulder-like curve. This is the same results as for the lips and since both are made out of a similar composition the same explanation can be given (Mercuri et al. 2018b, 38; Orazi et al. 2019, 117).

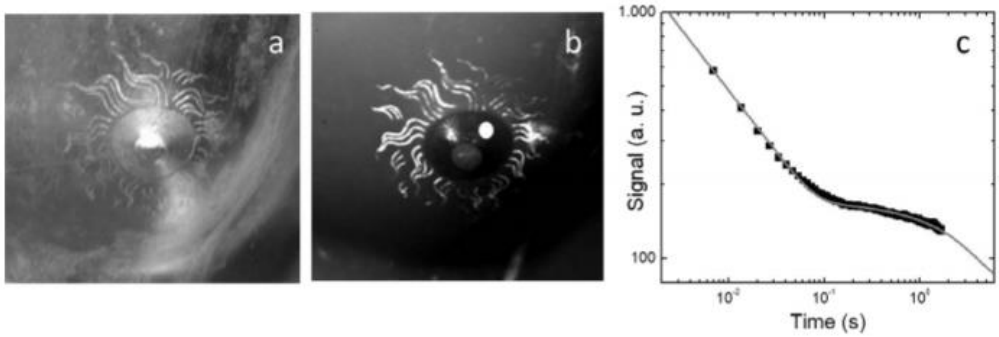

Figure 44: The thermograph of the left nipple and its corresponding thermographic signal (Mercuri et al. 2018b, 37, Fig. 9).

The left leg (figure 45) shows a large crack. To repair them a lot of small patches are used. These appear bright in the thermograph. Since the curve has a shoulder-like type the patches are of different composition and are applied mechanically (Orazi et al. 2019, 118).

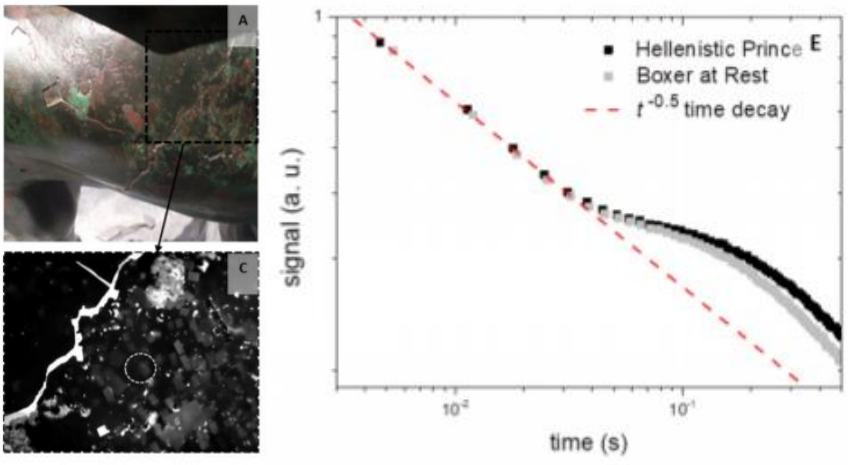

Figure 45: The thermograph of the left leg and its corresponding thermographic signal (Orazi et al. 2019, 119, Fig. 5A, C and E).

1.3.5. Hellenistic Prince-Italy

The bronze statue of the Hellenistic Prince now at the Museo Nazionale Romano is analysed to detect repairs, patches or insertions and defects, but also to check the previous restoration works (Bici et al. 2018, 2; Orazi et al. 2018, 1). Pulse IRT has shown that in contradiction to the statue of the Boxer at Rest, the statue is made out of a single cast (figure 46, a brighter area on the thermogram and a straight line on the graph indicates a homogeneous composition). The rest of the body contains some patches as repairs (located on the shoulder, feet, neck and leg) (Orazi et al. 2018, 7; Orazi et al. 2019, 115; 118-119: Orazi 2020, 287).

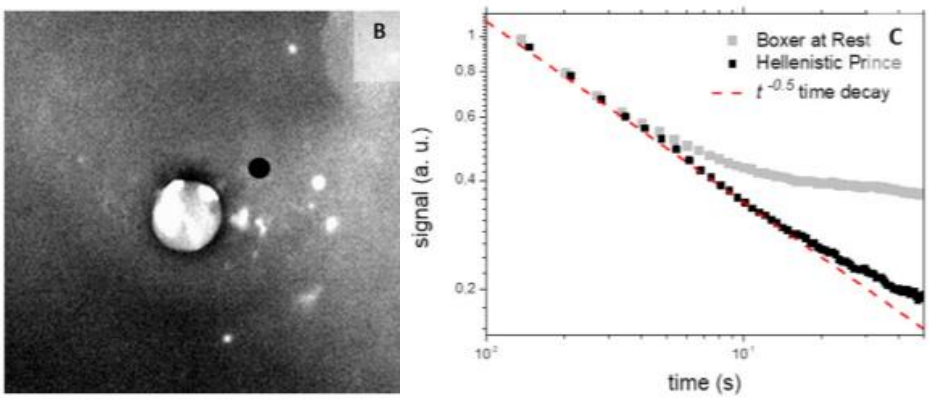

Figure 46: the thermogram of the nipple of the Hellenistic Prince (left) and its correspondent curve (left) (Orazi et al. 2019, 116, Fig. 2B and C).

Computer Aided Engineering is then applied to evaluate the preservation state and previous restoration. Figure 47 shows the inner frame used to support the statue with the ground basement. By analyzing the stress distribution and the cracks it is clear that the high-risk areas are those of the ankles, left arm and thighs (Bici et al. 2018, 3; 9).

Figure 47: The inner frame from a previous restauration phase (Bici et al. 2018, 4, Fig. 1b).

1.3.6. Capitoline She Wolf-unknown

The Capitoline She Wolf is currently located in the Musei Capitoloni in Rome, but its original location is debatable. It represents the wolf who nurtured Romulus and Remus. According to the dating, between the 11th and 12th century AD, the bronze sculpture is an original Medieval bronze statue. Because the iconography shows influences of the Etruscans, it has been seen as a copy of the original Etruscan statue (Mercuri et al. 2017a, 199; Orazi et al. 2018, 2).

During the restoration phase, it has been made clear that the statue has been cast in a single piece by the lost wax method. A representation is shown in figure 48. The bronze is been studied by compositional, petrographic and chemical analysis (XRF and XRD). The inner casting core corresponds to samples from the right side of the Tiber, contains some animal hair and is a mixture of silt, clay and sand. The bronze bulk has a composition of 85,8% copper, 9,2% tin and 5% lead, but slight alternation occurs on both sides in the amounts of lead, iron and tin (Mercuri et al. 2017a, 199-200).

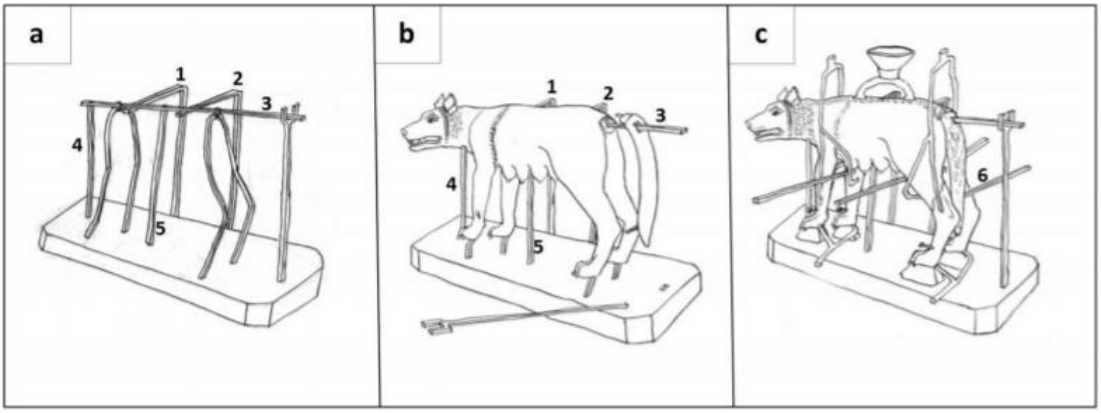

Figure 48: The manufacturing process of the Capitoline she wolf (Mercuri et al. 2017a, 204, Fig. 11).

Pulsed IRT has been used to analyse the repairs, decorations and casting faults. In this case, two flashlights orientated at angles from 45° till 60° and the change is heat is captured with a camera (Orazi et al. 2018, 2).

A total of seven repairs could be detected with pulsed IRT. Three of them were mechanical repairs (located at the pelvis, shoulder and tail), often planned, wedged patches and four are metallurgic repairs (located at the tail, chin and right front paw), usually faults in the original casting (Mercuri et al. 2017a, 199; 201; Orazi et al. 2018, 4-6).

The thermogram of a **mechanical repair** from the shoulder is visualized on figure 49b and the corresponding time dependence of the thermographic signals A, B and C on figure 50. The thermogram shows a patch covering the hole from a scaffolding bar visible by the bright (hot) edge due to a weak thermal contact between the underlying support and the edge of the patch (applied by hammering). Three points are used to measure the time dependency. Point A is located on the bright edge while point B and C are not. The graphs of B and C are similar to each other and the one depicted in figure 20b and show a homogeneous material. The graph of point A depicts a shoulder-like curve, similar to the other examples and this 'abnormality' is the result of a non-homogenous composition possible the presence of tin (Mercuri et al. 2017a, 202; Mercuri et al. 2017c, 6; Orazi et al. 2018, 5).

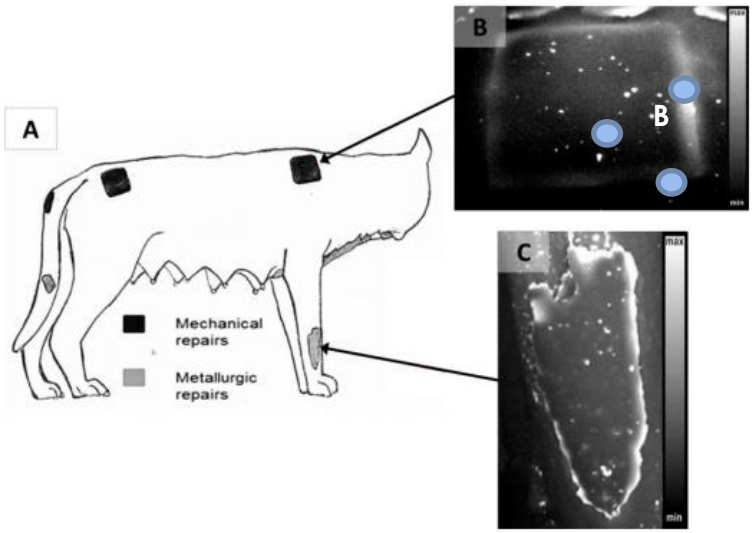

Figure 49: Positioning of the mechanical and metallurgic repairs (to: Mercuri et al. 2017c, 6, Fig. 3).

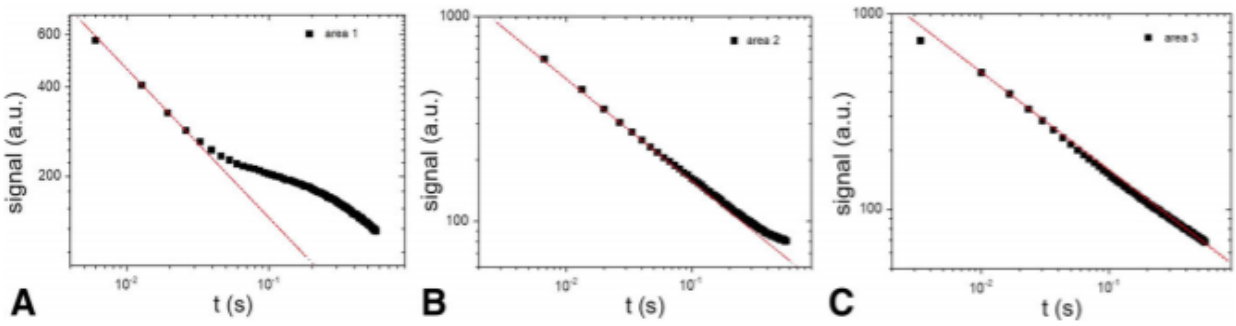

Figure 50: Time dependency of the thermographic signals A, B and C on a mechanical repair (Orazi et al. 2018, 6, Fig. 4)

The thermogram of a **metallurgic repair** from the right front paw is shown in figure 50c. The damage is probably caused by an error in the moulding process due to an insufficient amount of molten metal. The brighter (hot) area near the irregular patch shown a non-ideal thermal contact with the rest of the paw. The darker (cooler) centre of the patch might be thicker than its surrounding (Mercuri et al. 2017a, 203-204; Mercuri et al. 2017c, 6; Orazi et al. 2018, 5-6).

The thermogram of **decorative elements** such as the fur of the wolf is illustrated in figure 51. The brighter (hotter) edges indicate inhomogeneities from the moulding process of the wax model. This might be associated with a non-perfect adhesion of the fur and a mixture with the material of the external covering layer (Mercuri et al. 2017b, 7).

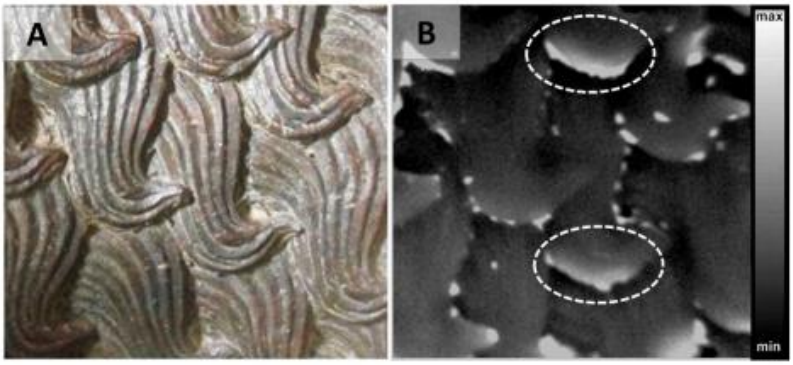

Figure 51: Thermogram of the fur of the Capitoline She Wolf (Mercuri et al. 2017b, 7, Fig. 4).

Casting faults (figure 52) occur in the cool-down process by the small reduction in size or due to a higher porosity and cavity level and might not be visible with the naked eye. Further, it is possible to analyse the depth of shallow errors with the front face heating mode of operation (Mercuri et al. 2017a, 204-206; Mercuri et al. 2017b, 5-6; Mercuri et al. 2017c, 8-9).

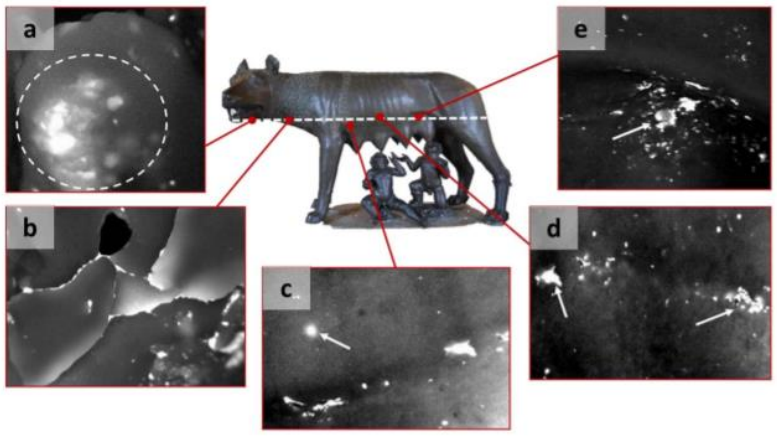

Figure 52: Casting faults on the Capitoline She Wolf (Mercuri et al. 2017a, 205, Fig. 12).

1.3.7. Virgin with Child-Italy

A wooden painting depicting the Virgin with Child made in the second half of the 13th century by presumably Cimabue has been investigated by thermography and reflectography. As a result, underdrawings, structural and superficial features could be recognized. To give some examples: at the drape, a clear *pentimento* appears and hot spots corresponding to reintegrated areas, nails and panels could be localized (Ambrosini et al. 2010, 199; 201-202).

1.3.8. Dancers fresco-Italy

A funerary Dancers fresco, located in the Ruvo's tomb in Apulia is analysed by Carosena Meola, Somone Boccardi and Giovanni Maria Carlomagno in 2016 (11-12). With active IRT they were able to distinguish three-layered horizontal stripes as a border instead of one (zone A in figure 53) and a previous painting (zone B in figure 53).

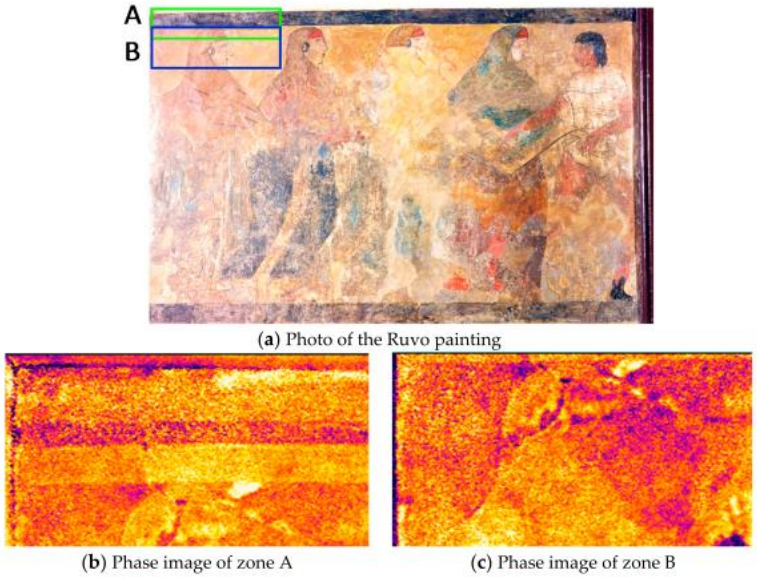

Figure 53: phase images of a fresco (Meola, Boccardi, Carlomagno 2016, 12, Fig. 17).

1.3.9. Frescoes-Italy

Frescoes located in Pompei at the *Domus of Casti Amanti* and the *Domus of C. Iulius Polybius* are analysed with active IRT to monitor detached areas and the influence of climate variations. The protective surface layer applied in a previous restoration made this analysis difficult due to its low emissivity and resulting in a high level of noise and false positives (Castellini et al. 2017, 53-56).

IV. Reflection-Optical methods

In this chapter methods depending on the optical reflective properties of the objects, surface is going to be discussed.

Another term applicable here is **surface metrology**. This type of measurements focuses on the surface characteristics such as roughness, small-scale features and the main form of the object. Surface texture is used in the field of surface or material engineering to test the quality of the product. It can give specific information but can give an image as well of the technology which has been used to fabricate the object. Therefore it can be an interesting tool for archaeological studies (Stemp, Stemp 2001, 82; Avdelidis et al. 2004, 571; Delegou et al. 2008, 437; Riegert, Konopka 2011, 163; Mital et al. 2019, 1).

The surface texture or topography is composed of lay, waviness and roughness. These three characteristics define the microtopography of the surface and are specific for the type of tool used in the manufacturing process or for the marks of use-wear. The detection of the topography is done by several techniques: profilometers, microscopy, photogrammetry, structured light scanners, interferometry and holography. To choose between these techniques several questions can be asked: which features (size and shape) tells more about the manufacturing process?, which features tells more about its function?, are the features intentional created or natural? (Townsend et al. 2016, 40; Macdonald, Harman, Evans 2018, 840)

In figure 54, the three components of the surface topology are visualized. Lay is the general direction of the texture and is characterized by the used equipment. Waviness has longer wavelengths in comparison to roughness and are caused by vibrations during the manufacturing process. Roughness are short wavelengths and define the irregularities of the surface. To evaluate one component, the raw data set is imposed on a filtering step. When a high-pass filter is used the roughness profile is obtained when a low-pass filter is applicated the waviness profiles is retrieved (Page et al. 2016, 112; Townsend et al. 2016, 44).

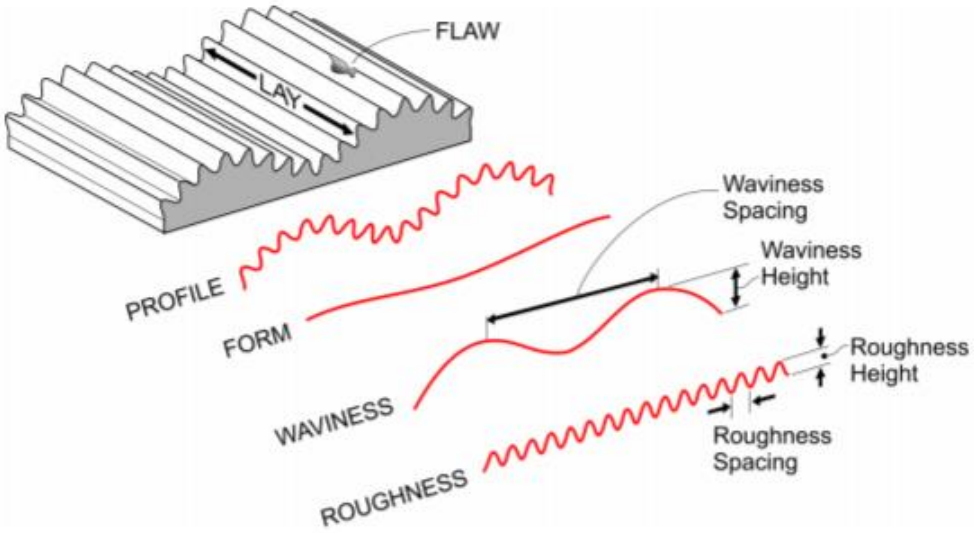

Figure 54: The terminology of the surface topography (Zygo Corporation 2018, 4).

Roughness is composed of several profile parameters (and area parameters). Rq is a mathematical length scale dependent parameter of the finest and closely spaced irregularities present on the surface and is defined by the following equation (Delegou et al. 2008, 436-437, Page et al. 2016, 113; Townsend et al. 2016, 41):

$$Rq = \sqrt{\frac{1}{l}\int_0^l \big(P(x)\big)^2 dx}$$

It is the root mean square of all the points, where:

- P(x) is the profile;
- l: length of the profile.

Another profile height parameter is the arithmetic average (Ra) which is most suitable for polished surfaces (Fort et al. 2013, 396; Page et al. 2016, 113; Zygo 2018, 5):

$$Ra = \frac{1}{l}\int_0^l |P(x)|\, dx$$

Final important parameters of Rq are the mean valley profile depth and the mean peak profile height. When both are viewed as a unit/sum it is called the average peak-to-valley profile roughness (Rz). All these parameters and others are described in the standard 4287 of the International Organisation for Standardisation (ISO) (Fort et al. 2013, 396; Page et al. 2016, 113; Zygo 2018, 6-7).

The main form and small-scale features can be analysed by different techniques. These can either be 3D-model retrieval or insights in the manufacturing process or enhancing small details. A distinction can be made when looking at the manner of sensing: either the natural or ambient light is used (= passive sensing) or an extern stimulus is used and the resulting patterns are analysed (= active sensing). Several of these methods are not considered new, but because their principles are used in combination with other techniques.

1. Photogrammetry-Structure from Motion

Photogrammetry is one of the 3D modelling techniques used to digitally replicate artefacts, the other techniques are laser scanning and structured light, both discussed in the next paragraphs. The use of photogrammetry finds its origin already in the second half of the 19th century. Now photogrammetry is being operated in many disciplines such as civil engineering, mapping, archaeology, mining etc. Photogrammetry in archaeology goes back to the beginning, especially for topographic map. Not long later the first object is photogrammetric documented: the ancient ruins of Persepolis. Another example dated from the 1990s is three Gudea statues of Lagash by Guitty Azarpay. Especially from the beginning of 2000 onwards, when more open source programs are available and it becomes more user friendly, photogrammetry has shown its potential in archaeology. At present, it is used to generate virtual models, relief models and orthophoto plans. It can be used for the documentation of artefacts and figurative art, but in recent years, it has shown its capability for analysing rock art. It detects subtle surface characteristics and even distinguishes the difference between natural or human-made deformations. Further, the generated 3D models can be interesting for musea and engaging the public such as Virtual Reality (VR), accessibility of the objects or online tours of excavations or exhibitions (Hixon et al. 2017, 3).

1.1. Theoretical principle

3D models are created through photographs or digital images (2D) and are a form of passive sensing through triangulation. A photogrammetric project consists of the following main two steps: data acquisition and image processing, where the image processing is realized with a technique called Structure from Motion (SfM) – Multiview Stereo (MVS).

The first step is taking the **photographs** (image acquisition) with consideration of the sunlight (when the data acquisition is done outdoors or on-site) or with the artificial light (when it is done inside or off-site), the number of photographs needed for the grade of detail and the settings.

Then **camera calibration and imaging orientation** is also known as restitution and alignment are computed for acquiring accurate images. Factors as lens distortion (interior orientation), finding corresponding points (relative orientation), ground control points for estimating the precision, root mean square (absolute orientation) and rectification of the images so that the epipolar lines of the images lies on the same level (this results in the removal of parallax except the one in the x-direction which contains the only information about the height differences of the object) (Schindler, Grabner, Leberl 2008, 464; Sansoni, Trebeschi, Docchio 2009, 574; Remondino 2014, 69; Brutto, Dardanelli 2017, 40; Hixon et al. 2017, 10).

The images must contain a certain degree of overlap (preferably 60-80%). By doing this finding the corresponding points will be easier. Second the base-to-depth (B/D) or base-to-height (B/H) ratio should be 0,5 – 0,8 for a strong geometric configuration (Schindler, Grabner, Leberl 2008, 464; Remondino 2014, 67; Brutto, Dardanelli 2017, 39).

Image point registration consists usually of four either fully automated or semi-automated steps. Fully automatization means that with every step of the software program no human intervention will be acquired. With semi-automatization, the obtained models can be reassessed and the outlying points and other error points will be filtered with hand. SfM runs a geometric reconstruction algorithm by finding the corresponding points in two or more images (this can be simultaneously done with the

camera calibration step). The 2D points are now located in a 3D space also called apoint cloud, these can be aligned by using ICP algorithm. MVS creates a depth map by tracing the location and orientation with the camera parameters for every pixel. This results in a more dense point cloud. Mesh generation or polygons (by Poisson) connect each point to create the surface of the object. This differs from 3D scanning where the gaps between the points will be interpolated to make a closed structure. In the final step, the texture and colour of the object will be applied with the information of the photograph (Schindler, Grabner, Leberl 2008, 465; Sansoni, Trebeschi, Docchio 2009, 574; Remondino 2014, 70-71; Brutto, Dardanelli 2017, 41-42; Hixon et al. 2017, 10; Collins et al. 2019, 7).

The 3D reconstruction is usually done by Agisoft Photoscan (Marziali, Dionisio 2017, 303; Berto, Salemi 2019, 63).

1.2. Advantages and limitations

Photogrammetry (with the combination of SfM-MVS) has one main advantage when comparing it with laser scanning, the possibility of generating a 3D model out of 2D images. These 2D images contain all the necessary information needed to make the reconstruction more realistic. When an object or statue is destroyed (intentionally or not) they can be remodelled when photographs are taken. This makes it possible for the recreation of the lost Cultural Heritage.

When using metrical cameras the interior orientation is already taken into account but this comes with a price. So often non-metrical cameras are used where the lens distortion can be solved by a software program which now the distortion curve for each type of lens and corrects the images according to this curve. Other solutions might be a self-made lens calibration or measuring more GCP during the absolute orientation. Non-metrical cameras are cheaper and therefore preferably used (Brutto, Dardanelli 2017, 40; Peng et al. 2017, 326).

This method has a high accuracy, where the maximum error is set at cm-mm even in some cases submillimeter level. The more GCP are available the higher the accuracy will be. This accuracy is dependent on the lighting, the camera setting (focal length,

diaphragm aperture), degree of overlap and texture (Almasri et al. 2017, 14; Quattrini, Nespeca, Ruggeri 2017, 647; Hixon et al. 2017, 10; Peng et al. 2017, 326-327). But when using macrophotography the depth-of-field (or the distance between the farthest and nearest object in one scene) is the main issue. It depends on the focal length, the focusing distance and the diaphragm aperture. The tinier the object, the larger focal length is necessary which results in a shorter depth-of-field and causing a shallow or blurred focus area (Marziali, Dionisio 2017, 300; Collins et al. 2019, 5).

While the image acquisition is rather easy, the processing of the images might need more experience, even though it can be fully automated, the desirable outcome is generated when applying semi-automatization. This involves human interference and can cause faults, on the other hand detecting outliers is better when done by hand than by machine (Remondino 2014, 66; Magnani, Douglas, Porter 2016, 1656; Marshall et al. 2019, 751).

The reflective properties of the object its surface can be an issue when it has a rather shiny surface (high reflective properties) or a darker surface (low reflective properties). Both problems can be overcome by powders or coatings (Neiß, Sholts, Wärmländer 2016, 652-653). When light is used to enlighten the object shadow effects must be minimalized. This can be done by putting small and medium-sized objects in a box or using a room with the least amount of ambient light (Quattrini, Nespeca, Ruggeri 2017, 644).

An advantage in contrast to laser scanning is its possibility to capture detailed colour information and cheaper equipment. The camera used for the image acquisition is normal digital single-lens reflection camera. They can be around 500 euros. Non-metrical cameras are usually cheaper than metric cameras. The software programs can be open-source such as Visual SFM or commercial-fee such as ReCap Photo which cost 325 euro per year. The most used software program is Agisoft Photoscan. The educational standard license only cost 59 dollars (Magnani, Douglass, Porter 2016, 1654-1655; Peng et al. 2017, 326; Marshall et al. 2019, 751).

The processing time is medium and dependent on the number of images and overlap. Approximately 2 to 4 hours can a process be, where the larger part is for the data processing (Marziali, Dionisio 2017, 306; Quattrini, Nespeca, Ruggeri 2017, 647; Collins et al. 2019, 12).

One of the disadvantages of photogrammetry is that a point cloud can only be generated through mathematical processing, while with active range sensors the 3D data directly be obtained (Remondino 2014, 67).

1.3. Its practice in archaeology

As previously said photogrammetry-SfM-MVS is used for 3D modelling of archaeological artefacts of different sizes. The smaller the object, the more difficult it gets to obtain a high accuracy for capturing the details. But due to the increase in accuracy cylinder seals and other small objects can be studied. Normally these are studied by making drawings or mould but now 3D models are generated by a special rotating device (Reh, Seitz, Speck 2016, 28). Since it is not a new technique, a lot of statues have already been digitalized and reconstructed into 3D models some examples will be given here.

1.3.1. Aegean seals-Greece

MUSINT II has started to make a virtual interactive museum with Aegean objects from Crete. By using macrophotography 17 Minoan seals (figure 55) from the National Archaeological Museum in Florence dating from the Minoan Pre-Palatial to the late Mycenaean period. They are approximately 15 mm diameter big and depicts animal and human figurines (Marziali, Dionisio 2017, 298-299).

Figure 55: A visualization of three 3D models (texture-mesh-wireframe) (Marziali, Dionisio 2017, 307, Fig. 2).

1.3.2. Marble statue-Jordan

An enthroned Tyche ivory-coloured marble from Gadara has been made into a 3D model. A Tyche is a very common goddess throughout the Near East and gains importance in the Roman empire where she is illustrated on coins, bronze and stone statues and terracotta figurines. In the current case, she is identified by a cornucopia which she holds in her left arm (Almasri et al. 2017, 6; 10).

Figure 56: the enthroned Tyche of Gadara as a 3D model (Almasri et al. 2017, 17, Fig. 38).

1.3.3. Various artefacts-unknown

In the study of Makris et al. (2018) a feminine bust, two sunken reliefs and two high relief artefacts are used. This study has shown that despite the three different manufacturing techniques, a good and accurate 3D model can be generated to study its conservation (Makris et al. 2018, 2).

1.3.4. Two statue of Roman emperors-Turin

The two statues of Julio-Claudians emperors are located in the Civic Archaeological Museum of Turin but were found in Susa. They are known for their highly detailed armour, wherein the first bust it depicts a mythical scene (*gens Iulia*) and in the second bust a victory scene (Donadio et al. 2018, 109). Photogrammetry and SfM are applied to model these statues to use them in a multimedia installation (Donadio et al. 2018, 110). High accuracy is obtained by several decimations and optimization processes such as polynomial texture maps (explained further) (Donadio et al. 2018, 113).

1.3.5. A bronze medallion-Italy

A micro-photogrammetric analysis of a bronze medallion (figure 57, now located in the Numismatic Cabinet of the Correr Museum in Venice) of roman emperor *Maximianus Herculeus* dating from the late 3rd century AC is analyzed by Berto and Salemi (2019). A total of 152 images where taken and they tried to study the impact of the reduction of the number of images in three steps (152-114-68-45). It became clear the less amount of images necessary the shorter the time. The cost is a lower accuracy of the geometry, but for numismatic studies is the resulting 3D model by only using 45 images good (Berto, Salemi 2019, 62-64).

Figure 57: The 3D model of a medallion of a Roman emperor (Berto, Salemi 2019, 67, Fig. 4).

1.3.6. Fragment of a Louteria-Italy

Two fragments (figures 58 and 59) from a *Louteria*, a large vase, from Cignana dating from the 5th century BC. To calculate the diameter of this vase a manual and digital procedure were combined resulting in an approximate 33 cm diameter for the *Centauromachia* fragment and an approximate of 30 for the *Komòs* fragment (Ebolese, Lo Brutto, Burgio 2017, 578). The first fragment depicts a *Centauromachia* in bas relief. Somewhat visible are three centaurs. But by making a 3D model certain characteristics can be highlighted and the representation is more clear. The centaur on the left is throwing something large, the middle centaur has hold of a *Lapith* and is armed. The right centaur is more degraded (Ebolese, Lo Brutto, Burgio 2017, 574).

Figure 58: The photograph (left) and 3D model (right) of a Centauromachia (Ebolese, Lo Brutto, Burgio 2017, 574 and 579, Fig. 3 and 20).

The second fragment depicts a *Komòs* scene. At first only three satyrs can be seen dancing around a column-krater. When looking at the enhanced 3D model other details appear: the satyrs are naked, the neck of the column-krater has a geometric decoration, the muscles of the satyrs and a cup is emerging at the top of the column-krater (Ebolese, Lo Brutto, Burgio 2017, 575; 579).

Figure 59: The photograph (left) and 3D model (right) of a Komòs (Ebolese, Lo Brutto, Burgio 2017, 575 and 579, Fig. 4 and 21).

2. Laser scanning

Previously it has been mentioned that laser scanning is another method for the creation of 3D models. Different from photogrammetry is this an active way of sensing by using a laser, phase or pulse. Since phase- and pulse-based laser scanners are mainly used for long-range scanning, only laser triangulation will be explained briefly.

2.1. Theoretical background

Laser triangulation is a technique used for short or closed range scanners. The principle can best be explained with following figure:

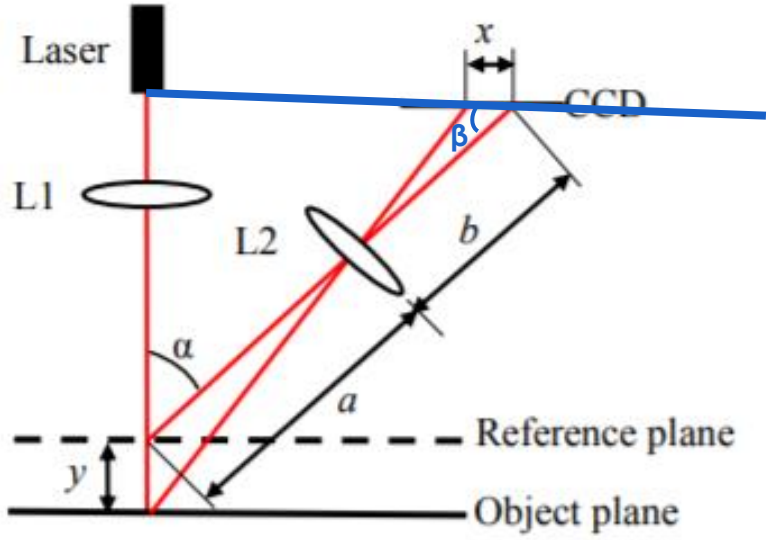

Figure 60: The principle of laser triangulation (to: Bai, Zhang, Tian, 2016, 2, Fig. 1).

A laser emits a single point or a laser line with a specific wavelength vertically towards the object. Dependent on the optical characteristics of the surface (transparency or colour) the emitted beam will be partially absorbed and reflected. A sensor (in most cases a charged-coupled device (CCD) camera) detects the quantity of the incident reflected beam. This allows to determine the distance of the object. When the position or distance is known the depth coordinate (z) can be calculated (Fontana et al. 2002, 326; Bogojevic 2012, 21; Mital et al. 2019, 5):

$$z = \frac{baseline}{\tan(\alpha + \beta)}$$

Where:

- Baseline is the distance between the camera and the laser;
- a is the angle between the laser and the lens before the sensor;
- β is the angle between light strip in the sensor and the lens.

Since laser units are monochromatic and in one direction a rotating polygon mirror is often used to scan in different directions. This makes it possible to measure the spatial coordinates of a set of points on the surface of the object and the creation of a dense 3D point cloud. The cloud can be converted into a triangle mesh format by connecting the vertices. To get an accurate colour and texture representation two CCD cameras will be installed instead of one (Fontana et al. 2002, 328; Fontana et al. 2003, 37; Giesko, Zbrowski, Czajka 2007, 98; Periverzoc, Ilieş 2012, 5; Munaro et al. 2015, 203; Bai, Zhang, Tian 2016, 1-2; Errickson et al. 2017, 651; Sarri, Athanassopoulos 2020, 176).

2.2. Advantages and limitations

In comparison to photogrammetry, the reflective properties of the object's surface can cause errors in the data acquisition phase. The same solutions can be used in this case. Both have high accuracy, here it can go to mm levels and a million points can be generated in several minutes (Fontana et al. 2003, 35; Periverzoc, Ilieş 2012, 9; Omar, Nehdi 2016, 148; Winemiller, Ochoa-Winemiller, Ludwig 2018, 1005; Sarri, Athanassopoulos 2020, 177).

In contradiction to photogrammetry, the laser scanners have a higher cost. The scanners deliver directly the points without the interference of math and it is independent to ambient light and texture of the surface (Bogojevic 2012, 21; Periverzoc, Ilieş 2012, 8; Arslan, Kaplan 2013, 19; Hixon et al. 2017, 2).

Other drawbacks are their generation of higher noise, the limited ability when sharp edges are present on the object and the necessity of a clear line of sight (Omar, Nehdi 2016, 148; Errickson et al. 2017, 651).

2.3. Its practice in archaeology

3D scanners have the same archaeological applications as photogrammetry: the digital models can be used as a template for the restoration (Fontana et al. 2002, 329), in the study of stylistic and motif analysis by isolating fragments of the model (Neiß, Sholts, Wärmländer 2016, 660), for a detailed examination of engravings or carvings (Bourider, Fuentes, Pinçon 2015, 142), to evaluate the degree of variability between or within groups, to record details such as facial features or decoration lines, mould study (Winemiller, Ochoa-Winemiller, Ludwig 2018, 1002), etc.

2.3.1. *Various artefacts-Nimrud*

In the study of Shanoer and Abed (2018, 298-299) different objects from the Iraqi museum were made into a 3D model: the limestone statue of the god of wisdom, a Lamassu from Nimrud (figure 61), a statue of king Sargon II and the glazed mural bricks from fort Shalmaneser III.

Figure 61: A 3D scan of a Lamassu (to: Shanoer, Abed 2018, 302, Fig. 14)

2.3.2. *Marble statue-unknown*

The marble statue of "San Giovannino Martelli" is used to analyse the impact of exposure to climate changes. It is located in the Bargello Museum of Florence and presumable dated from the 15th century AD. The maximal level of detail and Mohr-Coulomb criteria are here the main factors for evaluation if the risks. As a result, the right leg is the most exposed (Spangher et al. 2017, 63-67).

2.3.3. Terracotta figurine-Cyprus

Terracotta figurines from the 'House of Orpheus' in Nea Paphos (Cyprus) are studied to gain information on their style, structural aspects and expand these findings to an interactive platform (Papantoniou et al. 2012, 544; 549).

2.3.4. Terracotta figurines-Greece

In the study of Morris, Peatfield and O'Neill (2018, 56) two terracotta figurines from peak sanctuaries in Prinias (Crete) dating from the Bronze Age are made into replicas to understand their manufacturing and function.

2.3.5. Terracotta votive figurine-Greece

Terracotta votive figurines were found in a sanctuary at Plakomenos (Greece) and dates from the end of the 7th century to the middle of the 5th century BCE and scanned to gain more insight in their construction, details, indentations and surface lines. The aim of this collection is to develop a digital library (Sarri, Athanassopoulos 2020, 172-175).

3. Structured light

The final 3D-imaging technique is structured light, again based on active triangulation. White and blue light can both be used (Bogojevic 2012, 22). Fringe projection technique is also being used for fringe-projected profilometry and is discussed further.

3.1. Theoretical background

Instead of a single light, a (bi-dimensional) pattern or a bundle of geometric planes is projected onto the object. This is illustrated in figure 62. The configuration requires three components: a projector, one or two cameras and the object of interest. These can often be tripod-mounted.

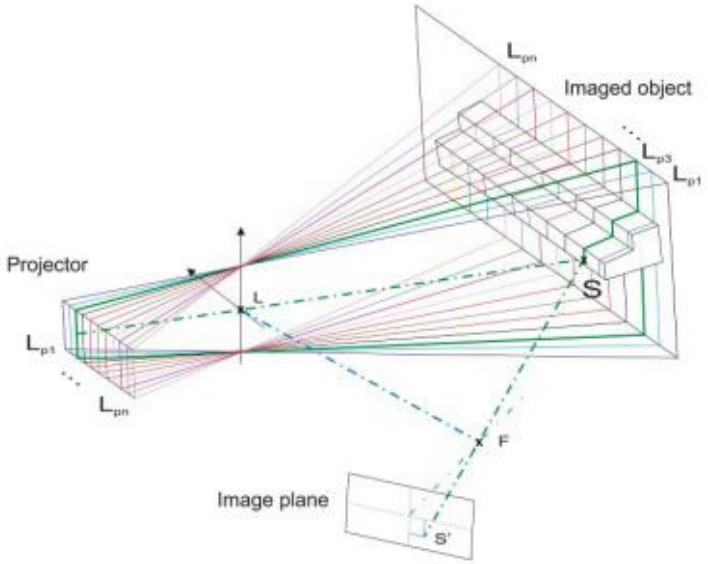

Figure 62: Structured light 3D imaging with laser triangulation (Periverzoc, Ilieş 2012,5, Fig. 5).

The pattern, fringes or parallel lines, square grids or dots are being projected vertically and displaced horizontally. They contain a coding strategy which creates a bridge between each pixel on the image with the desired code in the pattern network. This code is related to various pattern projection techniques: direct codification technique, spatial neighbourhood technique and the most frequently used multiplexing techniques. The latter operates with four types of coding systems: the binary system, which is the simplest of the three, N-ary code, grey codification with displacement or phase shift and grey code and line shifting (Gühring 2001, 223-224; Granero et al. 2009, 3; Sansoni, Trebeschi, Docchio 2009, 572-573; Bogojevic 2012, 22; Periverzoc, Ilieş 2012, 5; Counts, Averett, Garstki 2016, 210).

But other types of projections exist. Every company develops its own hardware and mode of operation, for example, Breuckmann is a widely used white-light 3D scanner where one of its projectors work with a miniature projection technique (MPT) which contains a stripe pattern with different widths and multi-phased slides (McPherron, Gernat, Hublin 2009, 20; Scafuri, Rennison 2016, 303).

The CCD camera (one or two) captures the changes of the reflected pattern in xyz-coordinates for each pixel, by comparing it with the original image. The z-coordinate represent the depth information and can be calculated by Fourier transform and transformed into a point cloud. An example of the registration of one point can be

seen in figure 62. Point S lies on the intersection of the plane LP_3 (dark green) and the line of sight SS'. The point clouds are then again meshed together (Granero et al. 2009, 4; Sansoni, Trebeschi, Docchio 2009, 572-573; Periverzoc, Ilieş 2012, 5; Counts, Averett, Garstki 2016, 210; Errickson et al. 2017, 652).

3.2. Advantages and limitations

Structured light scans have high accuracy and resolution at sub-millimetre levels (Granero et al. 2009, 3; Counts, Averett, Garstki 2016, 213). Similar to 3D scanning it is dependent on ambient light but also to moisture and dust (Tokovinine, Estrade Belli 2017, 19; Sarri, Athanassopoulos 2020, 177),

Because two cameras are used, both surface geometry, colour and texture can be recorded (Granero et al. 2009, 4; McPherron, Gernat, Hublin 2009, 20; Counts, Averett, Garstki 2016, 210)

They are useful for the analysis of small and medium-sized artefacts due to their high accuracy levels (Scafuri, Rennison 2016, 302).

3.3. Its practice in archaeology

While most of the materials (limestone, ivory, metal) can be used, terracotta seems to generate less detailed and accurate models (Count, Averett, Garstki 2016, 212; Kolobova et al. 2019, 67).

Because it is one of the better techniques to form 3D models of smaller objects and generates high accurate geometrical models with realistic textures, It might be the best tool to study figurative art.

3.3.1. Two sculptures-Greece

In the study of Stanco et al. (2016, 134; 136) two Greek sculptures (the Biscari head of a boy (figure 63) and a torso both found in the area of Leontinoi) were digitized with structured light and analysed to evaluate their possible association. To evaluate this association their stylistic appearance, their volume and virtual reconstruction. All these features confirm their association.

Figure 63: A digital reconstruction of the two separate pieces (Stanco et al. 2016, 139, Fig. 20).

3.3.2. Cylinder seals-Near East

SL can also be used as a fast method to generate plenty of digital 3D-models of cylinder seals (figure 64) to generate a large corpus. With these models, it is possible to unwrap the surface and keep the colour, details and texture (Dahl et al. 2018, 51-53). These can be combined with machine learning to find patterns and gain information in production, chronology and find matching impressed seals (Dahl et al. 2018, 57-59).

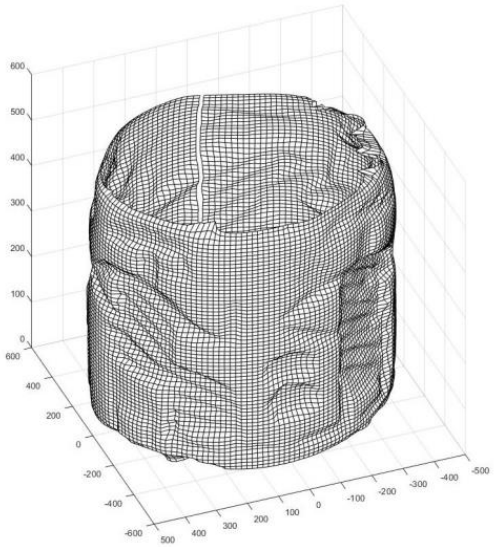

Figure 64: 3D model of a cylinder seal with SL (Dahl et al. 2018, 70, Fig. 9).

4. Profilometry

Profilometry can be used to extract topographical data and more precisely quantify the roughness. Contact profilometers use a stylus to detect the variations in the surface, where non-contact profilometers try to do the same but without the possibility of harming the object. Since it is important to make little damage to the artefact, non-contact profilometers will be discussed in this chapter. Laser profilometry, confocal laser profilometry, holographic profilometry, interferometric profilometry and fringe pattern profilometry are used to model the micro-topographical surface, only laser profilometry and confocal laser profilometry are used to analyse the roughness. Interferometric and holographic profilometry will not be handled here but they have an overlapping principle with fringe pattern profilometry.

4.1. Theoretical principles

4.1.1. Optical laser profilometry

This is based on laser triangulation explained with laser scanning at the beginning of this chapter. After modifications in a software program a 3D micro-topographical plot as in figure 65 can be obtained, such as the roughness parameters Rq, Ra and Rz (Giesko, Zbrowski, Czajka 2007, 98; Rodriguez, Curtis, Bartlett 2009, 501; Mital et al. 2019, 5).

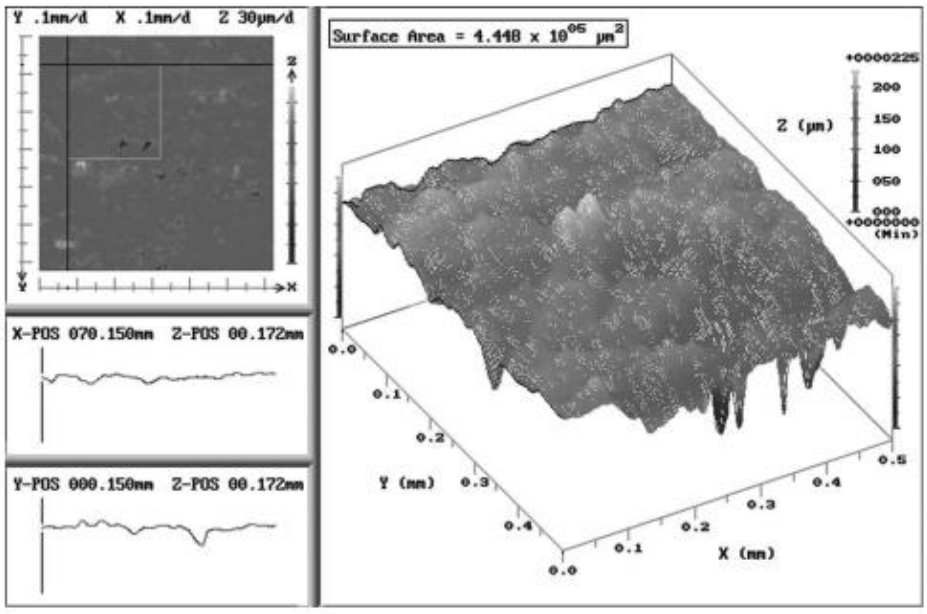

Figure 65: An example of a 3D micro-topography plot (Avdelidis et al. 2004, 573, Fig. 2).

4.1.2. Confocal laser optical profilometry

Confocal[3] laser optical profilometry works with the principle of a laser scanner confocal microscope (LSCM). The working principle of LSCM is illustrated in figure 66:

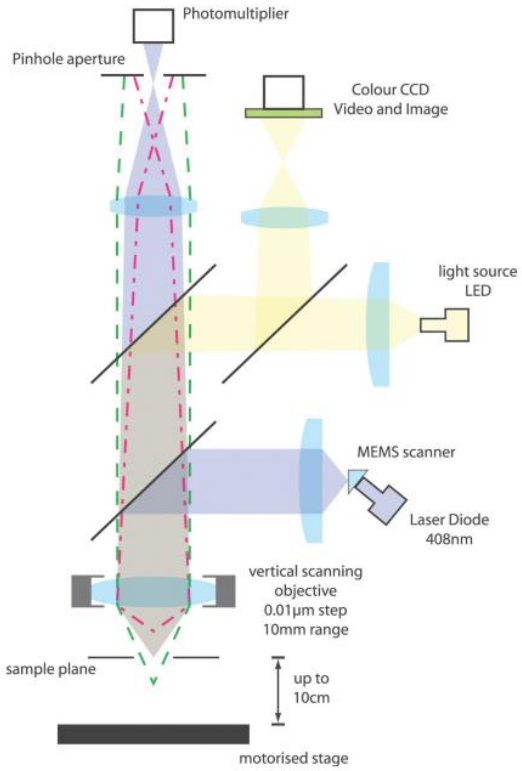

Figure 66: The working principle of LCSM (Evans, Maxwell, Cuickshanks 2012, 125, Fig. 10.2).

A LSCM uses an imaging system with two types of illumination: the incident light originates of a 405-408 nm laser diode for a microscopic 3D modelling and a white light source for normal viewing. The laser beam scans, often in a raster pattern, the surface using various types of mirrors, such as polygon mirrors, resonant Galvano mirrors (to increase the field of view), micro-electromechanical system mirrors (MEMS) and acousto-optic deflectors. All of them allows improving lower magnification. The reflected light passes through the optical pass and the confocal pinholes. They discard out-of-focus signal and therefore improves the signal-to-noise ratio and creates a low depth-of-focus which in result increases surface resolution. The focussed light is guided to a photomultiplier and the intensities are stored into an amplifier. These intensities correspond with the z-coordinate in each pixel and contain information about the height or depth which is used to generate a depth response curve. A high-resolution

[3] Two lenses with the same focal point

encoder measures the different heights, from this a surface profile or 3D-microtopographic plot will be derived from all these points and the roughness parameters can be calculated (Maté-González et al. 2017, 358; Fu et al. 2018, 2-3; Macdonald, Harman, Evans 2018, 843; Stemp, Lerner, Kristant 2018, 664; Calandra et al. 2019, 5941; Stemp, Macdondald, Gleason 2019, 516; Ibáñez, Lazuen, González-Urguijo 2019, 1182).

4.1.3. Fringe projection profilometry

Fringe projected profilometry (FPP) consists of two methods based on the structured light technique: phase-shifting profilometry (PSP) and Fourier-transform profilometry (FTP). In general, a (sinusoidal) fringe pattern or a (Ronchi or sinusoidal) grating (figure 67) is created by a computer and then projected on the surface of the object (Wu et al. 2012, 2037; Marrugo et al. 2018, 3-4; Willomitzer 2019, 37).

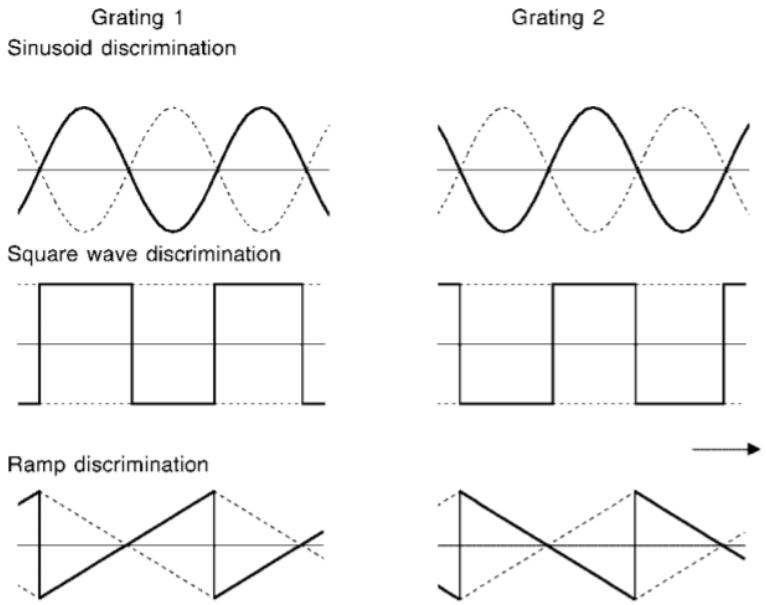

Figure 67: The difference between a Ronchi and a sinusoidal grating (White et al. 2002, 3594, Fig. 5A).

The pre-defined fringe pattern can be expressed as (Song et al. 2016, 75; Marrugo et al. 2018, 5; Zuo et al. 2018, 25; Wang 2020, 4):

$$I_0(x, y) = a_0(x, y) + b_0(x, y) \cdot \cos [2\pi f_0 x + \varphi (x, y)]$$

Where:

- I_0: the intensity of the fringe image on the reference plane
- a_0: the mean value of the reference plane;
- b_0: the amplitude of the reference plane;
- (x, y): coordinates of the pixel in the camera;
- f_0: the carrier frequency of the reference plane (sinusoidal);
- Φ_0: the phase modulation on the reference plane.

This causes a deformation of the fringe pattern due to the differences of shape and will be reflected and captured by the camera. This deformed fringe pattern can be expressed with the following equation, where the last section of this equation has the desired information (Marrugo et al. 2018, 5; Zuo et al. 2018, 25; Stivanello, Stemmer 2019, 689; Wang 2020, 4):

$$I(x, y) = a(x, y) + b(x, y) \cdot \cos[2\pi f_0 x + \varphi(x, y)]$$

Where:

- I: the intensity of the fringe image;
- a(x, y): the average intensity;
- b (x, y): the amplitude (related to ambient light and reflectivity);
- f_0: the frequency of the projected fringes;
- φ: the phase modulation of the deformed fringe pattern.

The obtained distorted fringe pattern can be analysed with FTP or PSP. The difference in both methods lies in the number of fringe patterns and in time. FTP only needs one high-frequency fringe pattern, while SPS needs several and in result, it takes longer to acquire the number of fringe patterns (Wu et al. 2012, 2037; Zuo et al. 2018, 24). Both methods consist of a phase wrapping (in a principal interval of $[-\pi, \pi]$) and unwrapping step. To have an absolute phase recovery phase unwrapping has to be performed. This can be done by temporal phase unwrapping (with multiple wrapped phase maps) or by spatial phase unwrapping (with a single wrapped phase map) (Zuo et al. 2018, 25).

FTP usually consists of five steps (figure 68), but recent studies have shown that some of these steps can either be dismissed or be more optimized. The principles of this technique already existed in the 1980s' and were formulated by Takeda and Mutoh in 1983 (Song et al. 2016, 75; Willomizer 2019, 37).

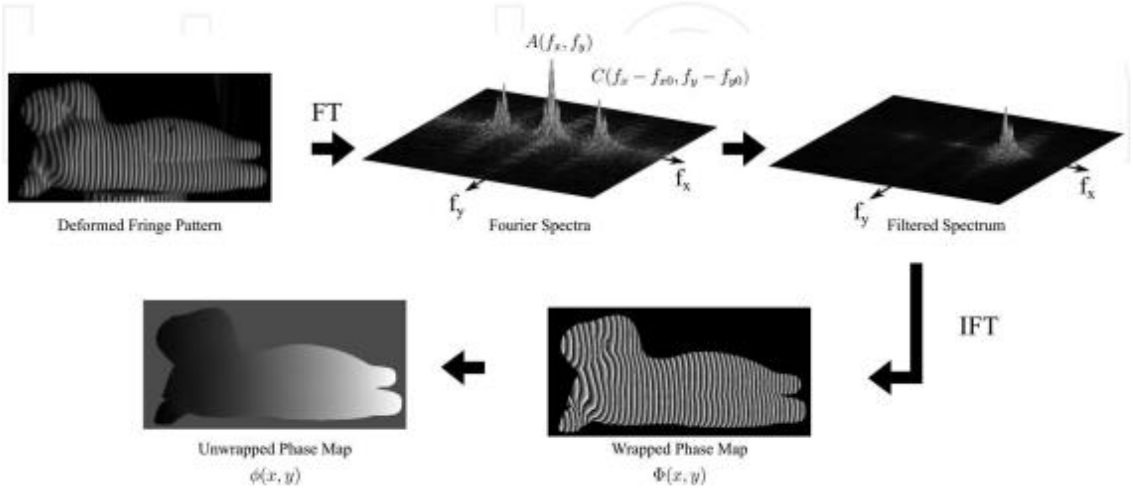

Figure 68: The principle of FTP (Marrugo et al. 2018, 5, Fig. 2).

The deformed fringe pattern is expanded to the cosine function and 2D Fourier transform (FT) is applied to find the phase of the fringe pattern and results in the division of the previous two equations into three spectra (Marrugo et al. 2018, 6, Zuo et al. 2018, 31):

$$\hat{I}\,(f_x, y) = \hat{A}(f_x, y) + \hat{C}(f_x - f_0, y) + \hat{C}^*(f_x + f_0, y)$$

A band-pass filter (for instance the Hanning filter) selects a fundamental unit to retrieve the phase and removes the unwanted amplitude variation: $C(f_x - f_0, y)$, i.e. the $\varphi\,(x, y)$ will be separated from $a(x, y)$ and $b(x, y)$ (Song et al. 2016, 75; Marrugo et al. 2018, 6; Stivanello, Stemmer 2019, 690; Willomizter 2019, 37; Wang 2020, 4).

The filtered unit is then subjected to inverse FT, resulting in a complex signal (Marrugo et al. 2018, 6; Wang 2020, 4):

$$\hat{C}\,(x, y) = \frac{1}{2}\, b(x, y)\, e^{i\,(2\pi f x + \varphi(x,y))}$$

The phase change (Δ φ (x, y)) is associated with the height distribution and this gives the following wrapped phases (Song et al. 2016, 75; Marrugo et al. 2018, 6; Zuo et al. 2018, 31):

$$\Phi(x, y) = \tan^{-1} \frac{\text{Imaginary part } [\hat{C}(x,y)]}{\text{Real part } [\hat{C}(x,y)]}$$

In the final step, the wrapped phase will be unwrapped with a specific algorithm given the wanted continuous phase map Δ φ (x, y). As seen on figure 68 this map shows the height of the surface of the object: the darker the higher. From these images, a 3D reconstruction can be made (Marrugo et al 2018, 7). This step can be skipped because some researchers believe the unwrapping phase has some pitfalls and takes time. Song et al. (2016, 74) propose two sets of wrapped phase maps (figure 69):

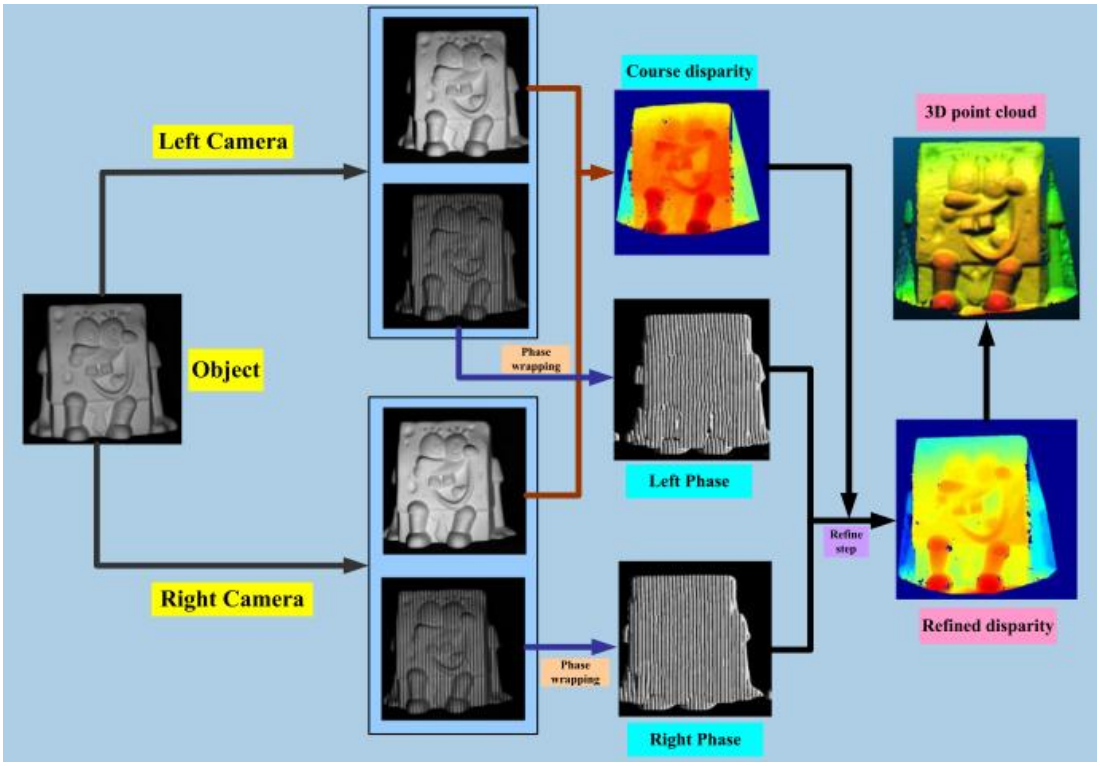

Figure 69: The principle of FTP without the unwrapping phase (Song et al. 2016, 75, Fig.1).

Two cameras are positioned above or in front of the object (binocular stereo vision). Both take a picture of the object with its corresponding fringe pattern. The wrapped phase is like the 'normal' way (FT → filter → inverse FT). Of the original image, the coarse disparity map is calculated by applying an Efficient Large-Scale Stereo Matching (ELAS) algorithm (Song et al. 2016, 74). Both original and wrapped phase image has been rectified (see Photogrammetry for more information). The final step is to link the

two phase maps by finding the corresponding phase. This is done by two processes. The first process is called local phase matching. The main principle is somewhat similar as with photogrammetry and SfM-MVS: find matching points located on both (in this case) phase images by coarse disparity (d), which allows obtaining the disparity (dp). This disparity is a pixel-to-pixel match between the two phase images (Song et al. 2016, 75-76). The second process is called sub-pixel disparity refinement. Since with the previous step pixel disparity is obtained, it needs to be more accurate and therefore going to sub-pixel level. Gaining a sub-pixel level can be done because the phase values are almost linearly in the entire interval of [-π, π]. This allows to find the sub-pixel x-coordinate of the matching point (Song et al. 2016, 75-77). A similar approach is proposed by M.E. Stivanello and M.R. Stemmer (2019)

When the coordinates of the different heights recorded in the pixels are known, a 3D model can be generated. The height in the function of phase distribution can be calculated (Su, Zhang 2010, 193; Stivanello, Stemmer 2019, 690):

$$z\,(x, y) = \frac{l0\ Øz\ (x,y)}{Øz\ (x\ ,y) - 2\pi f0 d0}$$

Where:

- l_0 is the distance between reference and the system;
- f_0 is the frequency of the fringes;
- d_0 is the baseline between the projector and the camera.

PSP uses multiple distorted patterns to retrieve phase information. These fringe patterns consist of several phase shifts in sine and cosine phases (figure 70) created by phase shift algorithms.

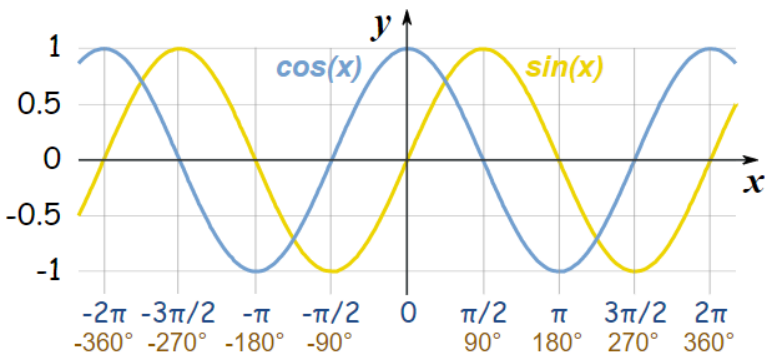

Figure 70: A plot of cosine and sine (Pierce 2018, s.d.).

There are a lot of algorithms created and the higher the number of fringe images necessary to extract the phase, the longer the processing time. Each one of them tries to overcome different types of errors: lens defocusing, intensity noise due to the ambient light, camera and projector noise, non-linearity error, phase shift error and intensity saturation due to high reflectivity or long exposure time (Chen et al. 2018, 179; Zuo et al. 2018, 34-40) and it is necessary to know their strengths and weaknesses before starting the analysis. This type of comparison has been done by Zuo et al. (2018). Some examples of phase-shifting algorithms are standard N-step phase shift with three phase shifts on the cosine (0, $\frac{2\pi}{3}$, $\frac{4\pi}{3}$), double three-step shifting algorithm with phase shifts on the cosine (0, $\frac{2\pi}{3}$, $\frac{4\pi}{3}$, $\frac{\pi}{3}$, π, $\frac{5\pi}{3}$) and in combination with FTP (π-shift algorithm or modified FTP) (Zuo et al. 2018, 25; 28; 32).

On these dataset phase wrapping and phase unwrapping are performed and with the resulted height or depth coordinates a 3D map can be generated.

4.2. Advantages and limitations

Since the principles of lasers profilometers are used for other techniques, the same advantages and limitations can apply here. Mayor problems are seen with highly and poor reflective surfaces and extremely rough surfaces. But it has a rapid data acquisition phase (1000 measurements per seconds) and a high resolution (submillimetre level) (Stemp, Stemp 2001, 82; Giesko, Zbrowski, Czajka 2007; 99; Baysan et al. 2018, 230).

LSCM can scan 8 million points per meter. The resolution is dependent on the type of laser used. The shorter the wavelength the better the lateral resolution will be. Equipment nowadays has a 120 nm planar resolution and a 10 nm vertical resolution. Pitfalls of LSCM are its price, the duration of each scan (the more variation are present in the surface its microtopography and the more points per meter are measured, the longer it takes to create 3D maps) and non-reflective surfaces. The latter can be overcome by using dual pinholes with detectors of various sensitivities. Special training might be necessary (Evans, Maxwell, Cuickshanks 2012, 123-125; Maté-González et al.

2017, 359; 367; Stemp, Lerner, Kristant 2018, 664-665; Stemp, Macdondald, Gleason 2019, 516).

The microscope has to be warmed up beforehand to rule out the possibility of thermal drift (Calandra et al. 2019, 5939).

Because laser profilometers and confocal laser profilometers measure quantitative data, it is used to identify the different tools used for engraving or carving of the object (Pedergnana, Ollé, Evans 2020, 9).

Fringe pattern profilometry is only used to generate 3D-models. Again any kind of material is measurable, but highly reflective areas might cause some irregularities on the maps. This can be resolved by using a specific harmless spray (Song et al. 2016, 81). Systems based on structured light are often pricier but they have a good accuracy (which is dependent on the phase distribution). In FTP the accuracy is increased by changing the fringe pattern, while in PSP different algorithms exist. FTP is faster than PSP since it only uses one single-shot and has, therefore, a fast measuring speed. When the phase unwrapping phase is disregarded, the importance of calibration (system, camera and recorder) is highlighted (Wu et al. 2012, 2038; Song et al. 2016, 74; Marrugo et al. 2018, 4; Stivanello, Stemmer 2019, 690; Willomitzer 2019, 37; Feng et al. 2020, 1).

Reduction of time is also achieved by combining FTP and PSP or with deep learning (Feng et al. 2020, 2).

4.3. Its practice in archaeology

Analysing the roughness parameters might be interesting for conservation purposes since it tells more about the friction, deformation, tightness of joints, etc. The 3D micro-topographical models are mostly used in the analysis of cut marks, rock or glyptic art and use-wear. In the Mediterranean, Cyprus and the Near East, it is not frequently used in figurative art, nor the last five year. Still, to show its benefits some case studies are given regardless off the time nor the place. Similar results (3D micro-topography) can be obtained by SEM and conoscopic holography, which might be a reason for the few case studies.

4.3.1. Bronze statue-Italy

In the study of Caragni et al. (2005, §3.1), the bronze statue 'Minerva of Arezzo' has been analyzed due to its bad state. It is located in the Archaeological Museum in Florence. Restauration work has been conducted earlier. From the 3D-data set micro-topographical analysis was conducted to evaluate the different roughness parameters.

4.3.2. Roman pottery-Switzerland

Montani et al. (2012, 3350-3352) studied *graffiti* carved on Roman pottery by laser profilometry. One of these fragments shows a figurative scene. The fragment is the bottom of a bowl made of Terra Sigillata imitation from Avenches (*Ciuitatis Heluetiorum Forum*). On figure 71 are the obtained 3D image and the vector image shown. The following details are now visible:

- A bird and an altar: presumably referring to a sacrifice;
- The letters IR and MARTI: referring to the Roman god of war, Mars;
- Letter T: not sure, might also be part of the bird.

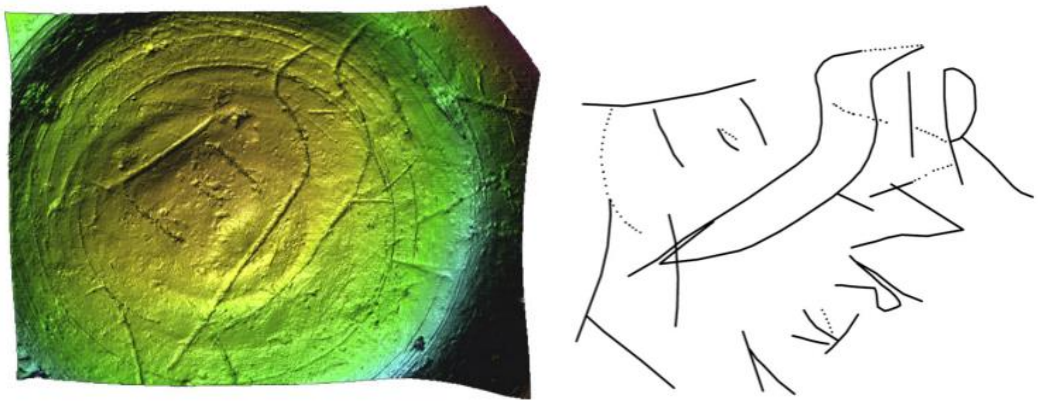

Figure 71: A 3D model and its vector representation (Montani et al. 2012, 3342, Fig. 4 and 6).

4.3.3. Limestone sculptures-Spain

Iberian limestone sculptures are analysed by Fort et al. (2013, 392). The five sculptures come from Cerrillo Blanco de Porcuna and are dating from the mid-fifth century BCE. For each of them a petrographic, mineralogical, colour, hardness and roughness analysis conducted. One of these sculptures is the Hunter with Hare (figure 72, E35).

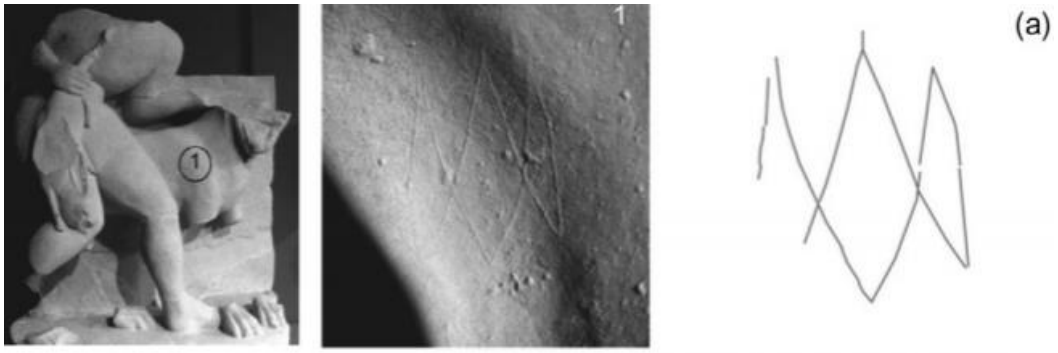

Figure 72: The surface mark of the sculpture 'Hunter with Hare' (Fort et al. 2013, 395, Fig. 2a).

On figure 73, the micro-topography of the mark is given. The lines are straight where on the end of B is slightly skewed (Fort et al. 2013, 400-404). The line B-B' was less rough and deep than line A-A', where an irregular topography is visible due to higher pressure or loose rock fragments. With each of these lines were less deep toward the end, this indicated a movement where the tool is dragged over the surface causing different pressure points. It might be that these marks are some sort of signature of the sculptor.

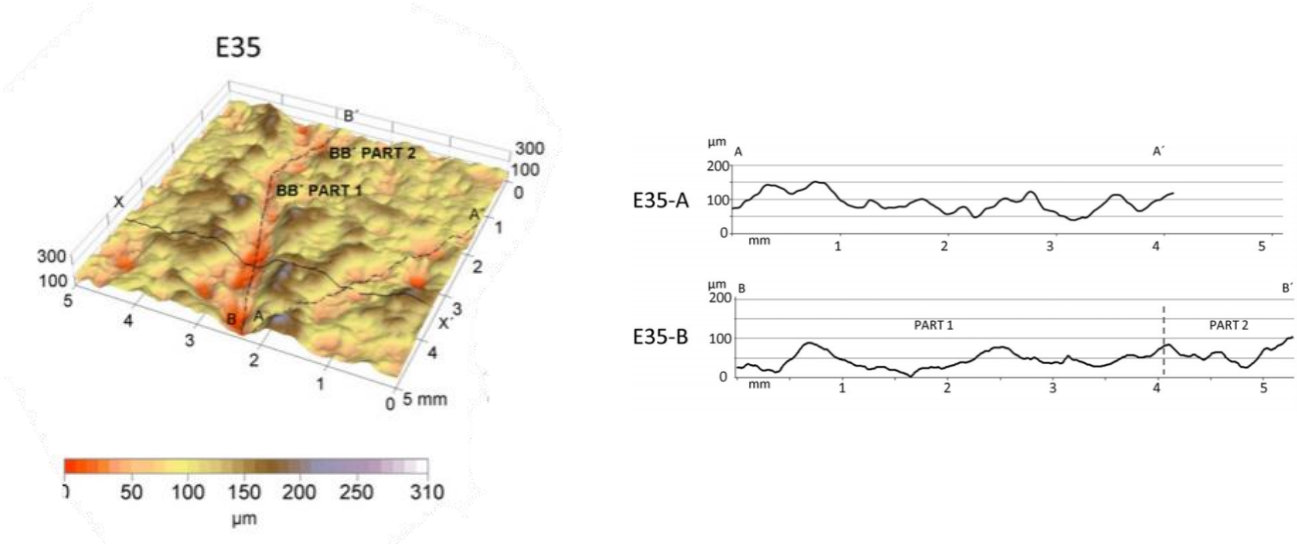

Figure 73: 3D micro-topography and its corresponding roughness profile (to: Fort et al. 2013, 400 and 402, Fig. 5 and 7).

4.3.4. Coins-Spain

A study on coins is conducted by R. Vargiolu, H. Zahouani and J.-Y. Blot in 2005 on coins from *San Pedro de Alcantara* (1786). Since these coins were located underwater the influence of corrosion is evaluated. By analysing the micro-relief three types of alterations are present: impact marks of sand, pitting erosion indicated by numerous deep valleys and erosion-corrosion (Vargiolu, Zahouarni, Blot 2005, 449).

4.3.5. Coins-Poland

A lot of coins of different countries are studied by their micro-topography. In the study of Kaplonek et al. (2018, 186-189) a chromatic sensor focal profilometer is used to give more insight into the iconography and manufacturing process or minting. One of these coins is a circulated and uncirculated coin from Poland. By analysing both 'exact' copies use-wear analysis can be conducted, due to changes in geometry (figure 74).

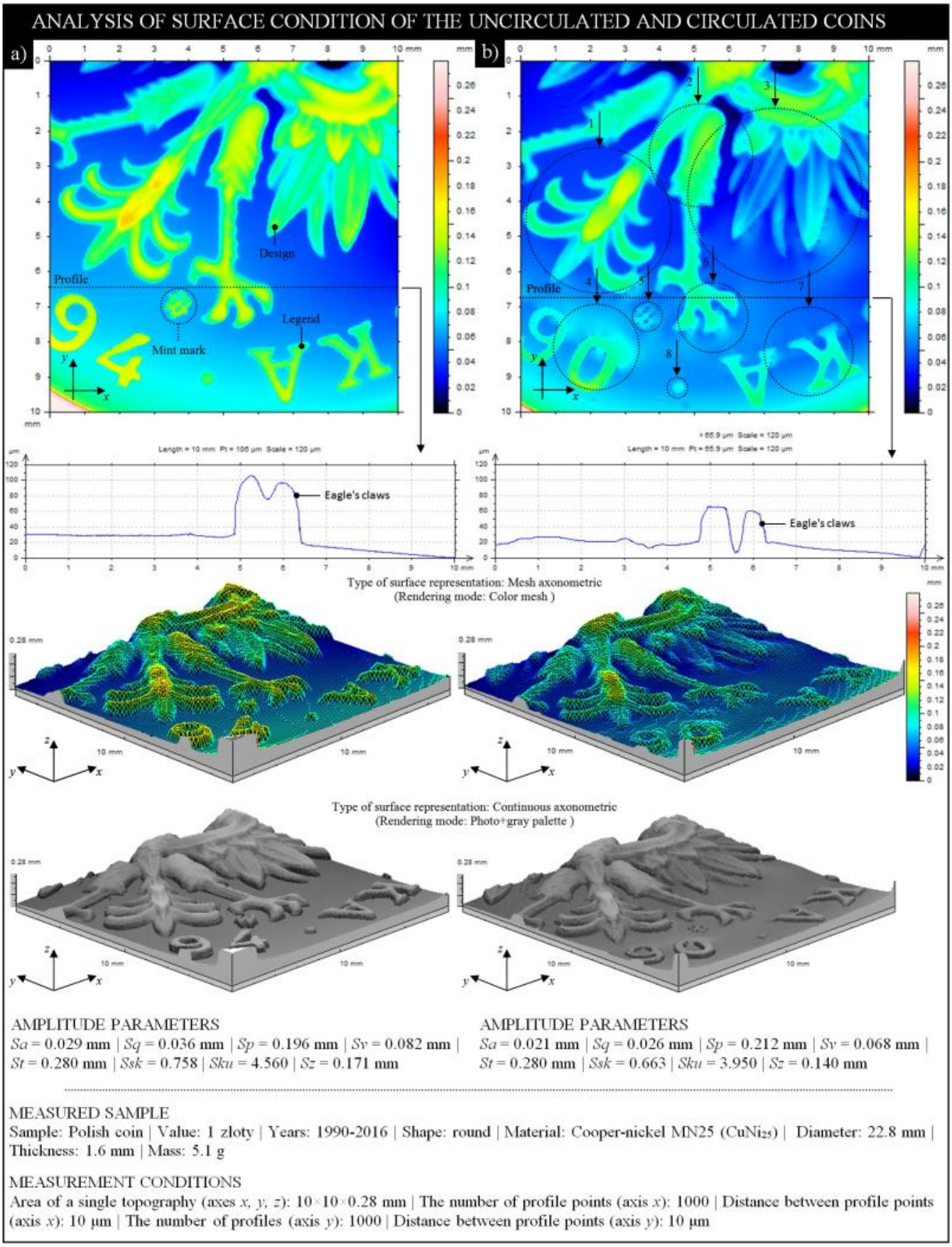

Figure 74: 3D micro-topography of a Polish coin (Kaplonek et al. 2018, 186, Fig. 4).

5. Shape from shading

Information about the shape of an object is gathered by analysing shadings. It is a photometric stereo technique where the obtained data for reconstruction of the surface is captured in one single image. A similar technique is reflectance transformation imaging (RTI). RTI is developed by Malzbender associated with Hewlett-Packard and later by Cultural Heritage Imaging. It is a real-time visualization of the surface through reflective characteristics and the resulting images can be digitally manipulated by modifying the incident light (Díaz-Guardamino, Wheatley 2013, 190; Arico, Greene, Parker 2016, 61).

5.1. Theoretical principle

It is known that different angles of incident light highlight other details of the relief on the surface and RTI works with this principle. Therefore is the data acquisition phase of this method crucial. Both camera and object have a stationary, fixed position (figure 75). The camera can either be placed above or in front of the object. The position of the light(s) can be movable in case of a narc or fixed by using a dome, where the position of the lights are known. With every image, the illumination angle will be altered. The results are a set of images with various incident light and shadows (Earl, Martinez, Malzbender 2010, 2043; Arico, Greene, Parker 2016, 62; Mytum, Peterson 2018; 490). In some cases, a black or red reflective sphere is positioned near the object in the camera's field of view. An RTI Builder software detects the highlights present on the sphere and calculates the direction and position and forms from this information a highlight blend map (Zányi et al. 2007, 22.4; Earl et al. 2010, 221; Earl, Martinez, Malzbender 2010, 2044; Arico, Greene, Parker 2016, 62; Mytum, Peterson 2018, 491)

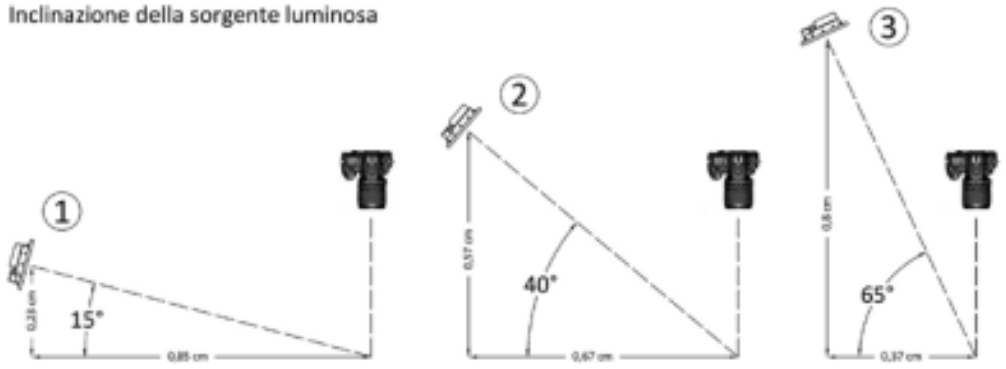

Figure 75: Possible selection of angles used in the acquisition phase (Fiorini 2018, 246, Fig. 2).

Processing these "texture" maps into one interactive image[4] can be done with mathematical fitting algorithms to generate RTI files: polynomial texture mapping (PTM), morphological residual models (MRM), hemispherical harmonies (HSH) and discrete modal decomposition (DMD). The final images can be visualized with RTI or PTM viewer software where the lighting can be virtually manipulated or by using different rendering descriptors (Pitard 2006, 19; Earl et al. 2010, 218; Earl, Martinez, Malzbender 2010, 2041; Maleševic et al. 2013, Polynomial texture mapping, § 1; Pires et al. 2014, 134; Pires, Rubio, Arana 2015, 418; DiBiasie Sammons 2018, 186; Fiorini 2018, 241; Mytum, Peterson 2018, 490; Coules, Orrock, Seow 2019, 1007).

5.1.1. Creating of normal maps

The first step of the fitting procedure is to generate a normal map by SVD. The calculation of the algorithms is based on each pixel (figure 76) of each captured image located in a spatial coordinate system (u, v). These pixels contains information about the micro-topography through colour or chromaticity (red, green and blue) and normals (Figure 77) or vectors perpendicular to the object's surface (or perpendicular to the tangent plane if the surface is not smooth) and showing the luminance or light intensity in that direction (L), assuming a Lambertian surface. As mentioned earlier the direction of illumination (θ_i, φ_i) is the only variable. For each local luminance two components, l_u and l_v correspond to the projections of the normal vector in a horizontal plane. This makes that L (u, v) is angle-dependent. These maps are then used in PTM, HSH and DMD (MacDonald, Robson 2010, 423; Kim et al. 2016, 85; Pitard et al. 2017, 610-611; Coules, Orrock, Seow 2019, 1007).

[4] In the form of a file and not a composite image

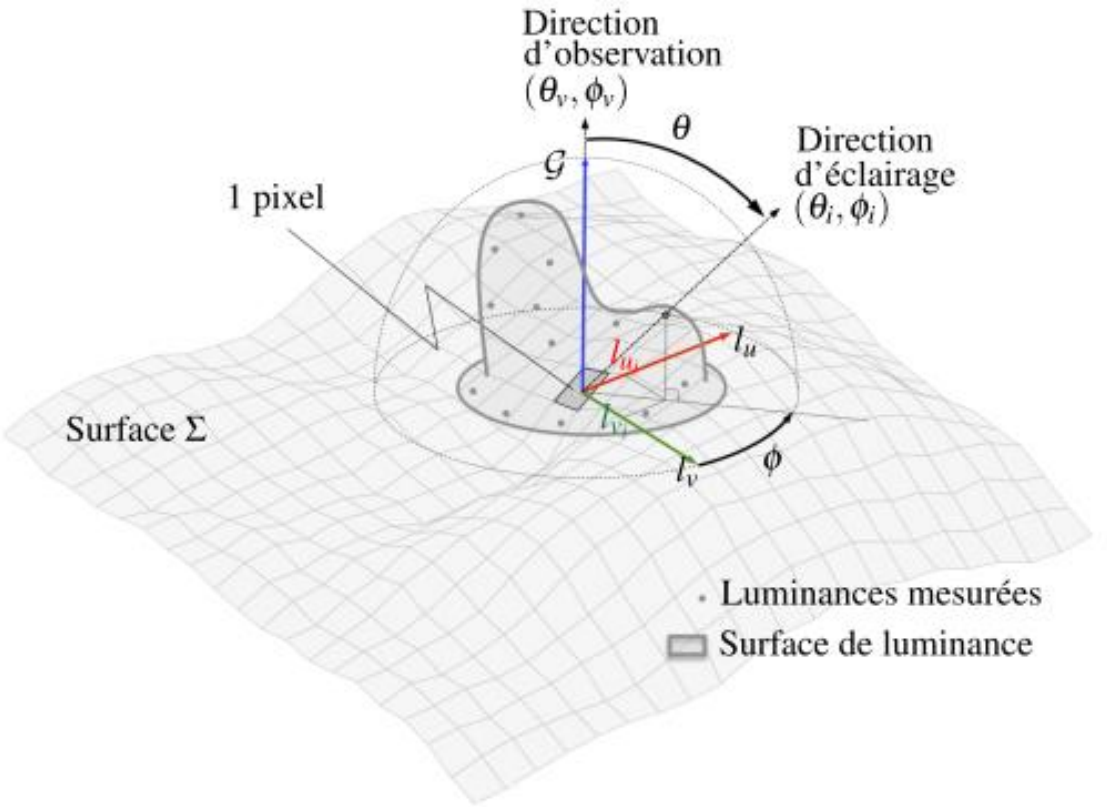

Figure 76: Visual representation of the different elements of luminosity (Pitard 2006, 21, Fig. 1.12).

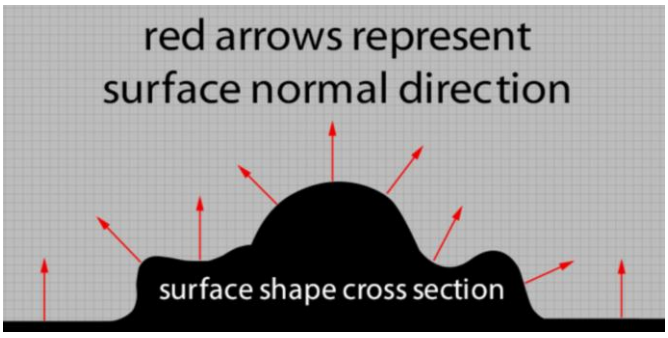

Figure 77: Normals of a surface (Cultural Heritage Imaging 2020, s.p. Fig. 1).

5.1.2. PTM

This mathematical algorithm fits a continuous biquadratic function with six parameters and multiple linear regression to calculate every intensity (luminance) value stored in the pixels. These six coefficients (a_0-a_5) are parameters for a second-degree polynomial model. This biquadratic function can be expressed by the following equation (MacDonald, Robson 2010, 423; MacDonald 2015, 45; Pitard et al. 2017, 610-611):

$$L(u, v; l_u, l_v) = a_0 l_u^2 + a_1 l_v^2 + a_2 l_u l_v + a_3 l_u + a_4 l_v + a_5$$

Where (figure 78):

- L (u, v) is the angle-dependent resultant luminance;
- u and v are spatial variables in a coordinate system;
- l_u and l_v are the projections of the vector.

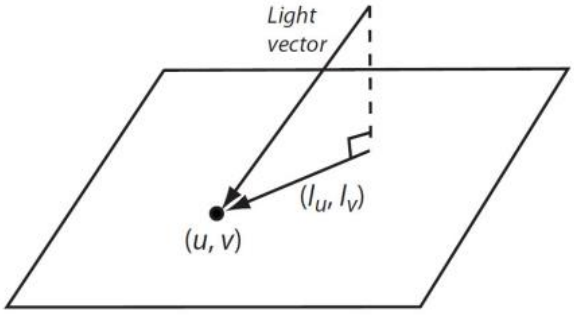

Figure 78: Visual representation of the different elements of lumonisity with a biquadratic polynomial function (Hammer, Spocova 2013, 5, Fig. 3).

In the end, nine values are stored in a new PTM-file: the three colours and the six coefficients. One PTM can produce a diffuse, a normal and a height map which is combined to generate a 2.5D texture map of the surface (Pitard 2006, 22; Coules, Orrock, Seow 2019, 1007).

Six modes of polynomial projections can be described (figure 79a): one translation, two inclinations, one saddle-shaped and two parabolics. The drawback of this technique is it is not convenient for complex and highly irregulated surfaces, because it 'over smooths' (figure 80a) the respective surface (MacDonald 2015, 47; Pitard et al. 2017, 610-611).

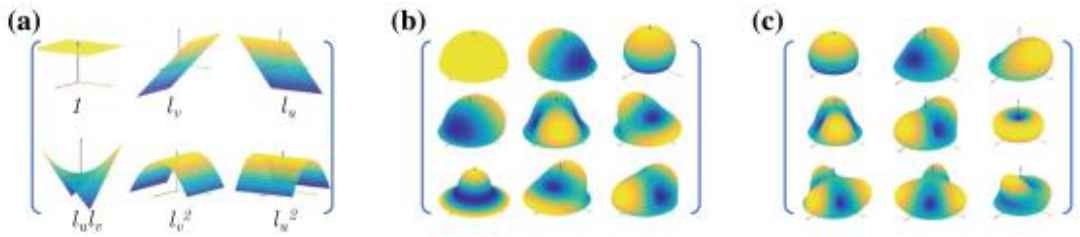

Figure 79: Different type of modes of polynomial projections for respectively PTM, HSH and DMB (Pitard et al. 2017, 611, Fig. 4).

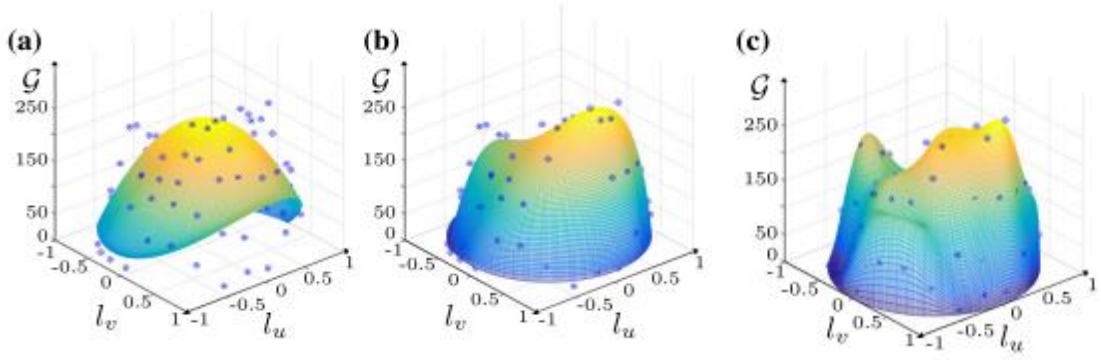

Figure 80: The reflectance surface for respectively PTM, HSH, DMB (Pitard et al. 2017, 613).

With all this information (colour and form) the 3D geometry and texture maps can be reproduced by three sorts of maps: a displacement/height map for the geometry, a normal map for the surface details and a diffuse map for the colours (Elfarargy, Rizq, Rashwan 2013, 355). Generating a diffuse map from PTM is quite easily done because the chromaticity (red, green and blue) is stored separately from the luminance (as explained above). In this map, each pixel has the same amount of light which generates a more uniform lighted map (Elfarargy, Rizq, Rashwan 2013, 356). In a normal map, the surface normal is stored as red, green and blue values for each pixel. Estimation of the surface normal is done by the directional lightning information (MacDonald, Robson 2010, 422; Elfarargy, Rizq, Rashwan 2013, 357). At last, a height map uses 3D details to generate a mesh. They can be used to remodel or refine a surface (Elfarargy, Rizq, Rashwan 2013, 358).

5.1.3. MRM

Illustrated by figure 81 are the different steps for generating an MRM-map. First, a 3D model is created from a dense point cloud (a). Then a decimated model (or trend surface) is created by a mesh decimation algorithm which can correspond to a more distant view of the object with a lower spatial resolution (b). A smoothing algorithm (Laplacian filter) is applied (c). Here the Latin inscriptions are not a part of the model and calculate the morphological details excluded of the trend shape. This makes it possible to visualize local small-scale irregularities apart from the engraving. As of last the residuals are encoded in a colour model. These colours (independent of the position of the light source) contrast positive and negative shape variations from each other and makes it possible to capture the micro-relief of the object or morphology by

combining the different 3D-models without considering the texture. This method is usually combined with PTM-files (Pires et al. 2014, 136-137; Pires, Rubio, Arana 2015, 419; Pan et al. 2017, 34).

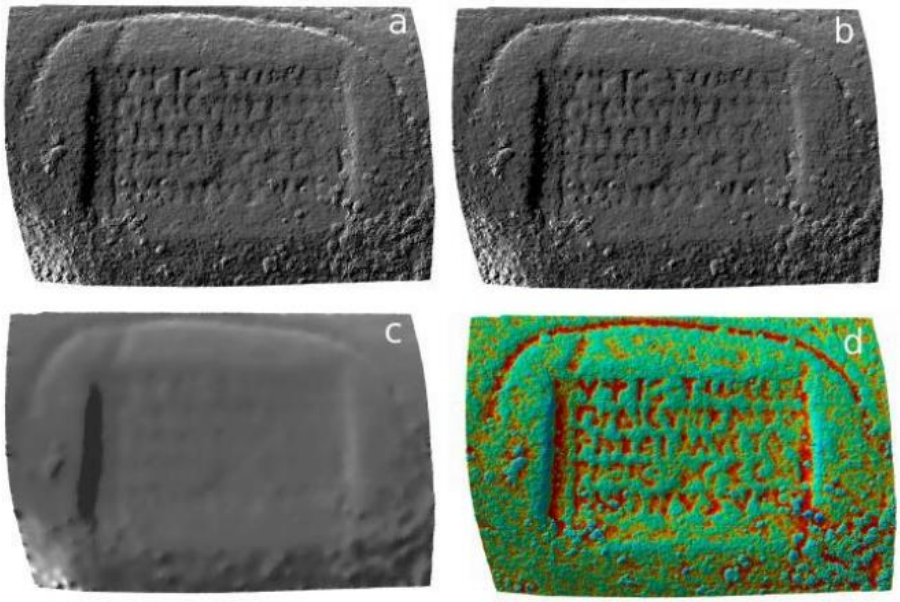

Figure 81: A MRM of an Latin inscription from a Roman sanctuary in Panóias (Pires et al. 2014, 137, Fig. 7.2).

It is possible to combine both geometry and texture properties (figure 82) by adding the texture information to the normal map and generate a fused map. This can be relevant for marble-based figurative art (Pan et al. 2017, 36).

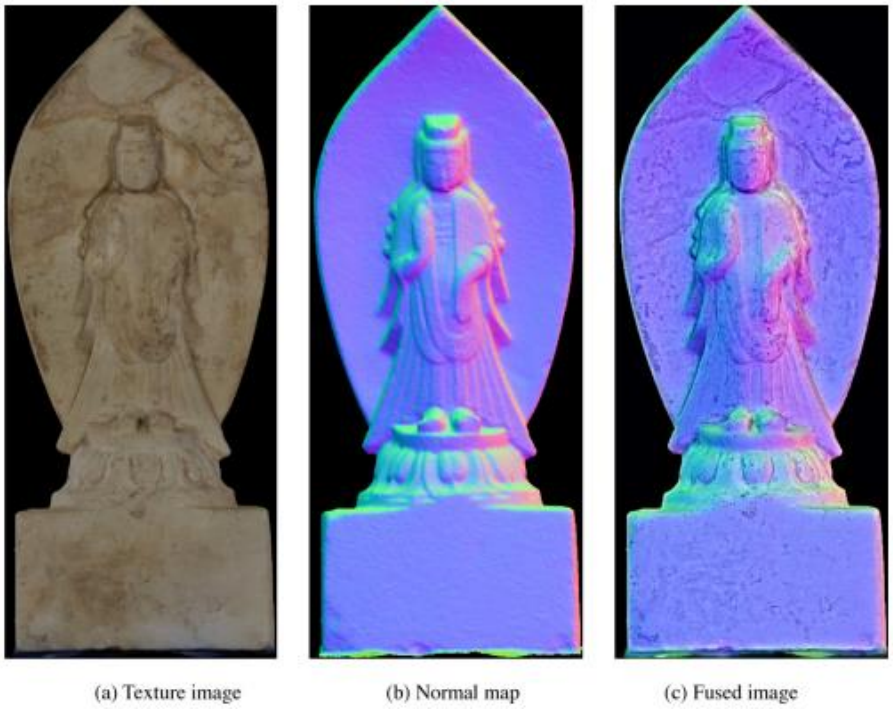

Figure 82: A fused image of a marble statue (Pan et al. 2017, 34, Fig.2).

5.1.4. HSH

HSH is developed to overcome the problems of PTM (figures 79b and 80b). Here the orthogonal basis functions are limited to the domain of a hemisphere since only the upper hemisphere of a normal is visible. The component of an HSH-functions is the elevation angle (θ) and the co-latitude (φ). The functions are derived from shifted Associated Legendre Polynomials by applying a linear transformation. The reflectance per pixel can be calculated with the following expression, where the best results can be obtained by nine parameters (four first-order terms, five second-order terms and seven third-order terms) (Gautron et al. 2004, 321-330; MacDonald 2015, 46; Pitard et al. 2017, 611; Pintus et al. 2018, 90):

$$I = \sum_{l=0}^{n-1} \sum_{m=-l}^{l} \alpha_l^m H_l^m$$

Where:

- l is the number of the order;
- m is the number of the degree;
- a is the coefficient;
- H is the HSH.

5.1.5. DMD

DMD can be used to evaluate the angular reflectance function for each pixel and has higher accuracy in comparison to PTM and HSH (figure 79c and 80c). The function can be expressed as the residue of decomposition and the linear combination of modal vectors. Same as HSH it is described in a hemisphere (Pitard et al. 2017, 612-613; Coules, Orrock, Seow 2019, 1007).

5.1.6. RTI/PTM viewer

Finally, the fitted files can be analysed with an RTI/PTM viewer software program. Here the reflectance properties can be changed to increase the perception in an interactive virtual environment (Díaz-Guardamino, Wheatley 2013, 192). For archaeological purpose several rendering descriptors can be used to enhance details and micro-reliefs, explained by figure 83 (A is a normal picture):

- Surface normals (figure 83D): the creation of false-colours map;
- Normal unsharp masking: enhancement of the edges;

- Diffuse gain (figure 83C): maintaining the normal and increasing the shallow surfaces by increasing the curvature of each pixel;
- Specular enhancement (figure 83B): a monochromatic visualisation by enhancing the reflectivity by estimating the direction of light with maximal brightness (Malzbender, Gelb, Wolters 2001, 519; Earl, Martinez, Malzbender 2010, 2042; Díaz-Guardamino, Wheatley 2013; 192; DiBiasie Sammons 2018, 186; Mytum, Peterson 2018, 495; Coules, Orrock, Seow 2019, 1009).

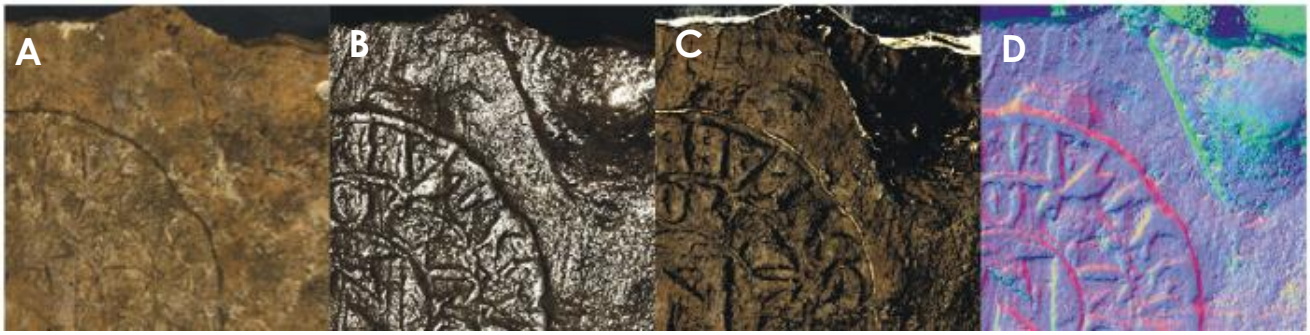

Figure 83: Portus brick stamp surface under different types of lighting perspectives (to: Earl, Martinez, Malzbender 2010, 2046, Fig. 9).

5.1.7. Combination with 3D-modeling techniques

This technique is often accompanied by photogrammetric data or other 3D imaging tools such as laser scanning or structured light scanning (which are explained in other paragraphs). This allows combining accurate geometrical data with accurate texture mapping (Earl et al. 2010, 221; Zányi et al. 2007, 22.3; Fiorini 2018, 242; Coules, Orrock, Seow 2019, 1007).

5.2. Advantages and limitations

When using a dome construction a fast data acquiring can be obtained, this is the contrast when a movable light source is used since the position needs to be calculated each time of capturing an image. This dome structure causes some difficulties when analysing larger objects and especially unmoveable objects. In comparison as with the 3D-modelling techniques, ambient light needs to be avoided, by either applying a neutral lens or taking one photograph with full exposure to ambient light. The two important software programs are freely available and additional software programs are rather cheap. It is also easy to learn but not easily portable (dependent on the size of the dome). On its own, it renders poor geometry

qualifications but when combined with 3D-models a complete model can be achieved. But since the cost is moderate, using 3D models might elevate the price (Earl et al. 2010, 220; Earl, Martinez, Malzbender 2010, 2043; Díaz-Guardamino, Wheatley 2013, 191; Kotoula, Kyranoudi 2013, 85; MacDonald 2015, 48; Santos et al. 2015, 439; Arico, Greene, Parker 2016, 63; Porter et al. 2016, 86; Kim et al. 2016, 84).

5.3. Its practice in archaeology

IRT can be used for different kind of materials ranging from organic (wood, bone, paint, clay) to inorganic (copper, metal, stone). Therefore a various set of figurative art can be analyzed: painted walls, stele, numismatics, terracotta figurines, inscriptions and engravings (Kotoula, Robinson, Bedford 2018, 26; Morita, Novoa, Bilmes 2019, 1). Recently a new method, micro-RTI have been used to examine textiles from Yoram Cave in Israel (Goldman et al. 2018, 2). With this technique the technology, production methods, design decoration, etc. can be studied (Earl et al. 2010, 219; Earl, Martinez, Malzbender 2010, 2040; Fiorini 2018, 243).

5.3.1. Terracotta figurine-Jordan

A total of 450 terracotta figurines are found in the Buṣayra and Jordan can be dated in two periods: a part is older than the mid-sixth century BCE, another part is between the mid-sixth century BCE and third century BCE (Hunziker-Rodewald, Fornaro 2019, 191). One of these, in particular, is the most complete figurine (Reg. 637). This figurine has been under study (as part of the Franco-German Figurines Project) before but RTI has shed some new light on these interpretations. A dome structure with 48 white-lights LED has been applied (Hunziker-Rodewald, Fornaro 2019, 194). On figure 87 the RTI of figurine Reg. 637 is visible.

Figure 84: The RTI of the upper part of a terracotta figurine (Hunziker-Rodewald, Fornaro 2019, 201, Fig. 9a).

Five new observations have been made regarding this figurine:

- Possibility of paint at the back of the figurine and above her eyes;
- The form of the eyes now rather be described as more almond-shape;
- The hands show incisions representing fingers, parallel lines representing bracelets and hold the breast in a cupping position;
- The appearance of a choker;
- On her head, she is wearing a shoulder-length veil or hood but a piece of hair is coming out on the front (Hunziker-Rodewald, Fornaro 2019, 199-200).

These figurines represent pregnant woman, non-pregnant woman, some are painted etc. and are quite similar to each other. The goal of the researchers of the Franco-German Figurine Project is to acquire a collection of all those figurines to compare them and study their relationship with each other in relevance to their context. Due to the similarity, these researchers would like to investigate the possibilities of long term use of the figurine or mould, heirlooms etc. (Hunziker-Rodewald, Fornaro 2019, 192). For this study, the Geometric Morphometric study described in the first chapter might be useful.

5.3.2. Neolithic figurine-Greece

To try and understand a figurine completely Neolithic figurines from Koutroulou Magoula (Greece) are analyzed with photogrammetry-SfM, 3D printing, RTI and multispectral imaging (see further). They were made with local clay and could be made by a single core or composite technique (Papadopoulos et al. 2019, 626-635). RTI is used to gain insight in the texture of the figurines: fingerprints, brushstrokes or marks. A fingerprint (figure 88) is detected on the head of a bird-shaped figurine. It is hypothesized as a learning model due to the badly fired and partially smoothed character (Papadopoulos et al. 2019, 640).

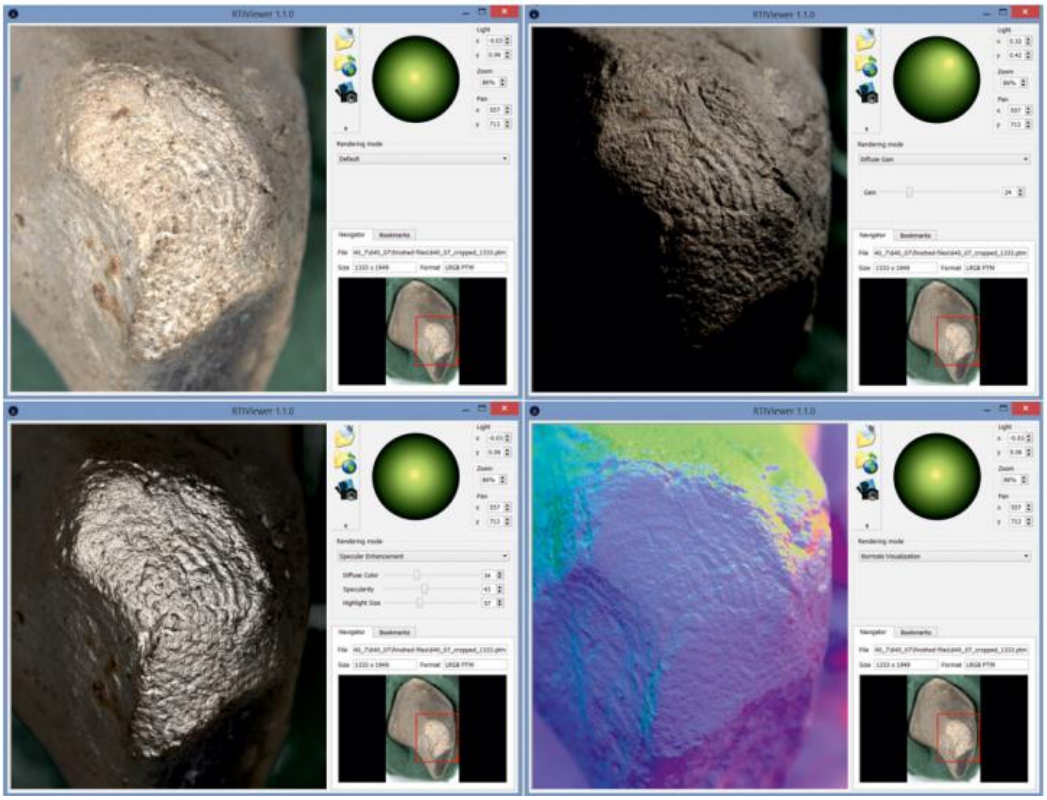

Figure 85: A fingerprint on the head of a figurine (Papadopoulos et al. 2019, 641, Fig. 8).

Brushstrokes can be seen as small vertical and horizontal lines across the figurine (figure 89). The colours used on figurines is detected by multispectral imaging. Colours are created in this culture by differences in the type of clay and its preparation. On the figurine of a sitting female (figure 90), red colour is used for vertical bands on the back and front, for a collar and a belt (Papadopoulos et al. 2019, 641-642).

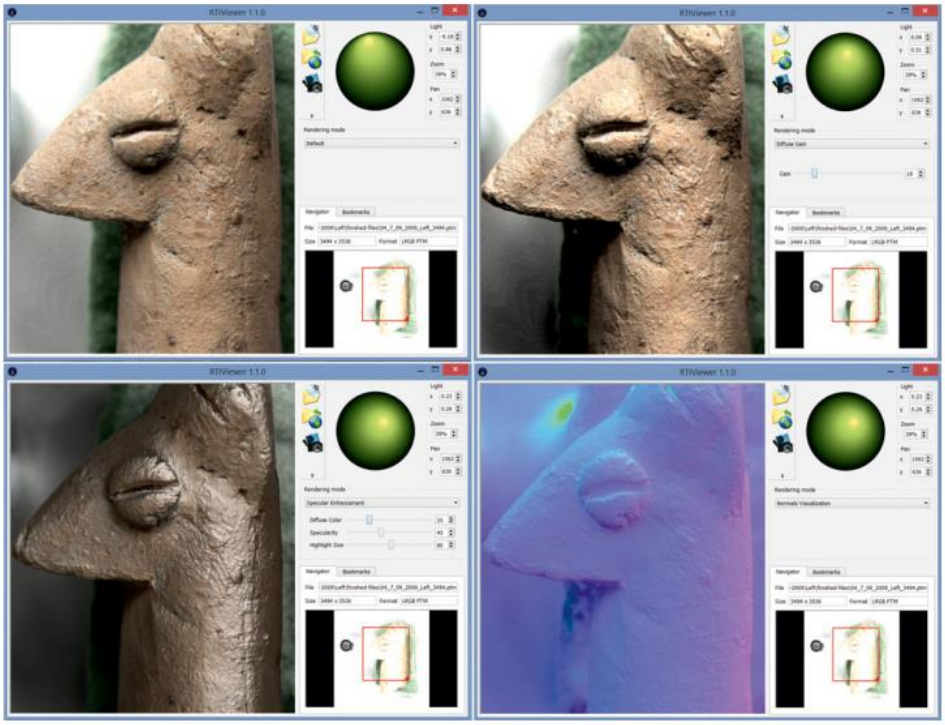

Figure 86: Brush strokes on a figurine (Papadopoulos et al. 2019, 643, Fig. 11)

Figure 87: Multispectral imaging of a figurine (Papadopoulos et al. 2019, 644, Fig. 13).

V. Transmitted energy

In this chapter the transmitted properties of the artefacts will be discussed.

1. Tomography

Tomography is an imaging process as well, based on a penetrating ray. As result slices of the object is obtained. There are many types of tomography but some can be used in archaeology, such as computed tomography and neutron tomography.

1.1. Computed tomography

1.1.1. Theoretical background

Computed tomography is a non-destructive, non-contact imaging technique to visualize the inner structure of an object. Further, it gives detailed information about the geometry. An X-ray or gamma-ray beam is used for analysing the object and is directed from multiple angles and positions (360°). Dependent on the density of the material, a part of this energetic beam will be absorbed. The rest of the energy (attenuation) will be calculated and cross-sectional images can be formed. With a specialized algorithm, these can then be used to create a 3D model (Pavel et al. 2012, 193; Miles et al 2016, 35; Maher 2020, 1). The attenuation depends on the composition of the material, the energy, the path length (Pavel et al. 2012, 193).

1.2. Neutron tomography

1.2.1. Theoretical background

Neutron tomography is based on the measurement of the absorbance of neutrons. Since neutrons have an electrically neutral charge they easily go through the object (= transmission, see figure 3) and interacts with the nucleus (in contradiction to X-ray). The unattenuated neutrons are recorded (at various time intervals) by a detector and a contrast image is produced. How deep a neutron can go depends on the energy-distribution of both incident beam and material. 3D images are obtained by a series of projections and algorithms (Szilágyi, Kis, Szentmiklósi 2016, 158-159; Kardjilov et al. 2017, 330-332).

1.3. Advantages and limitations

The main advantage of tomography in general is that the inner structure can be revealed without destroying the outer structure.

X-ray computed tomography has a high spatial resolution and a low distortion (Gapinski et al. 2014, 258; Maher 2020, 2). It has a fast data acquisition and processing time, about ten minutes (Pavel et al. 2012, 195).

Neutron tomography has also a high accuracy and fast processing time but it is more dangerous when the acquisition time is long (alteration of the colour and structure). There are not that many neutron-imaging facilities which increase the price. It is best combined with X-ray since neutrons can easily detect light elements (Szilágyi, Kis, Szentmiklósi 2016, 160-161; Kardjilov et al. 2017, 332; Lehmann 2017, 6-7).

1.4. Its practise in archaeology

With tomography information about wall thickness, attenuation values and the inside of an object can tell a lot about its manufacturing process. Weaponry, pottery, coin hoards and figurative art can all be studied (Szilágyi, Kis, Szentmiklósi 2016, 165).

1.4.1. Bronze sculpture-Southern-Levantine

A southern-Levantine bronze sculpture from the Late Bronze Age I is analysed with neutron-based techniques to gain insight in the composition, manufacturing process and origin. It is located in the Museum of Fine Arts, Hungary. It depicts a naked Canaanite goddess with monkeys sitting next to her, palm trees and is in an Egyptian style (Maróti et al. 2017, 368; Szentmiklósi et al. 2018, 478). In this study prompt-gamma activation analysis (PGAA, elemental composition), ToF-ND (detect manufacturing process) and NT are combined. PGAA shows that the composition correlates with a cast tin-bronze with impurities of Ni and Mn. The ToF-ND indicates the presence of oxidized iron. NT shows three parts (figure 88). A is the dark grey area consistent with neutron-transparent areas and indicates tin-bronze alloy. B is the brighter area consistent with a higher attenuation due to the high content of hydrogen and chlorine. C is a mixture of both and consists of medium attenuation. Another

observation is that the monkeys are solid, while the palm stub is hollow (Maróti et al. 2017, 371; 374; Szentmiklósi et al. 2018, 478).

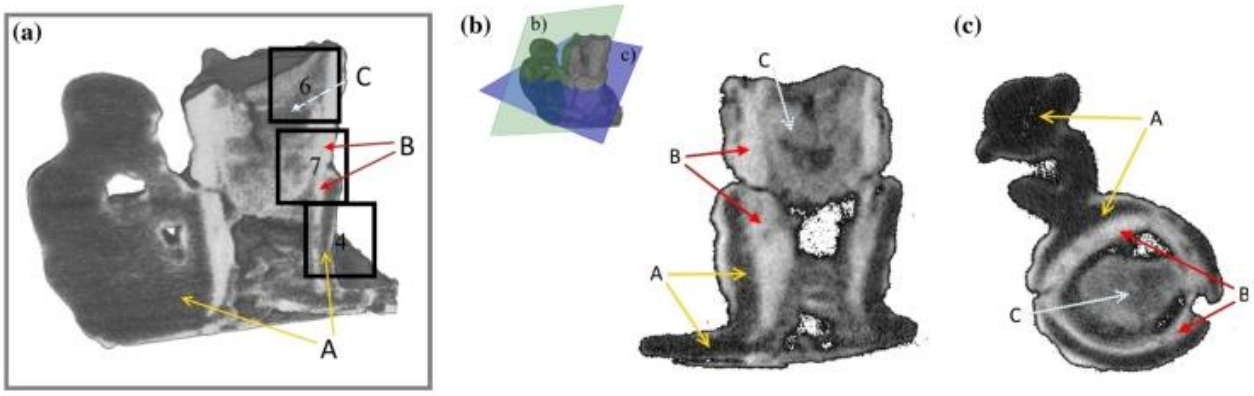

Figure 88: the 3D image of the palm and left monkey (Moróti et al. 2017, 371, Fig. 5).

1.4.2. Coins-England

Coins are analysed with neutron and x-ray computed tomography. One example is the Selby coin hoard. In two ceramic pots silver denarii (figure 89) from the first millennium BC to the second millennium AC was recovered. X-ray computed tomography made it possible to analyse the coins without opening or breaking the pots, by digitally stripping away different sections. Further, individual coins could be analysed. RTI is applied to better understand the details of the surface (Mital et al. 2016, 37-39).

Figure 89: X-ray computed tomographical image of a coin hoard (Mittal et al. 2016, 39, Fig. 9).

1.4.3. Coins-unknown

Two Roman silver denarii of Empress Favstine I are analysed with several techniques to understand its design, usage, provenance and manufacturing and to generate a workflow for assessing coins. PTM is used to monitor colour and surface changes. Focus stacking with a digital microscope gives a highly detailed 3D surface model. Photogrammetry-SfM is used for the acquiring of high-resolution colour images and laser scanning and SL for the spatial data. X-ray microtomography is used for the images on the internal microstructures to detect cracks or impurities. SEM, EMPA and XRF were used for the compositional analysis (Hess, MacDonald, Valach 2018, 5-14).

VI. Colour residue

Colour, in general, can tell something about the tradition, the perspective of the period or the artist, the trade routes, use of local sources, functions of certain rooms, symbolism and technique or skills (Sbroscia et al. 2020, 1-2).

To get colour, different colouring agents will be used such as metals, paint or pigments and coloured marbles (Østergaard 2018, 1). The pigments are synthetic, organic and non-organic and they need to be mixed with a binder or medium to produce paint. The used binder is related to the technique of application. When wet limewash is used the technique is called fresco when eggs or gum is used the technique is called secco (Siddall 2018, 1; Kokiasmenou et al. 2020, 1). Other binders can be based on plant-derived oils or wax (Brøns, Hedegaard, Sargent 2016; 50; Østergaard 2018, 1; Siddall 2018, 1).

Throughout the Mediterranean, Cyprus and the Near East, a majority of similar pigments have been used. It is noteworthy to remind that when examining the pigments the colour palette varies in different periods, style, application and accessibility to certain minerals or metals. Here is a list of pigments used mostly in the period from the Bronze Age to the Roman time (Brecoulaki 2014, 2-24; Brøns, Hedegaard, Sargent 2016, 29-32; 50-57; Gasanova et al. 2018, 88-92; Siddall 2018, 7-22; Radpour, Fischer, Kakoulli 2019, 11):

white	blue	green	yellow
•dolomite •aragonite •gypsum •calcite •lead white	•egyptian blue •azurite •amphybole mineral •lapis lazuli	•celadonite •malachite •egyptian green •mixture	•yellow ochre •goethite •jarosite •natrojarosite

red	brown	black	pink/purple
•red ochre •cinnabar •hematite •magnetite •cochineal •realgar	•mangenese umber	•carbon •mangenese •mixture	•madder •Murex •mixture

1. Detection of colour

Getting a full understanding of the presence of colour can be done by multi- and hyperspectral imaging (and maybe in the future ultraspectral imaging). Here the acquisition of photographs is taken in a broad range of wavelengths of the EM-spectrum. Multi- and hyperspectral imaging rely on the same principle. The images are created by a high-resolution camera or a spectrometer, where either coloured filters are placed in front of the lens or different coloured LEDs are used. They differ in resolution, but both make it possible to see UV (10-380 nm), visible light (380-700nm) and NIR (700-1100nm). Multispectral imaging usually refers to 3 to 15 non-continuous (small gaps) spectral bands of the light spectrum with a spectral resolution of 100 nm, while hyperspectral imaging refers to 100s to 1000s of continuous narrow spectral bands with a spectral resolution of 10 nm (MacDonald et al. 2017, 3; Howell 2018, 37-38; Verhoeven 2018, 2; Mathys, Jadinon, Hallot 2019, 92).

There are three ways of registering these images: the reflected radiation will be recorded (visible reflected photography, IR reflected and UV reflected), the transmitted radiation will be recorded or the fluorescence is detected (UV-induced luminescence, UV-fluorescence, visible induced visible luminescence, visible induced IR luminescence) (Nocerino et al. 2018, 773). The process of luminescence and fluorescence is explained in the beginning (see: Basic Principles).

In general, these imaging methods can be used to study traces of pigment, to map the original colour, study the layering effects, gain information of the technological achievements, their inspirations and finding evidence of underdrawings through the

interaction between emission and detection of photons (Comelli et al. 2016, 1; Dyer, Sotiropoulou 2017, 2).

1.1. Ultraviolet

Ultraviolet induced visible luminescence (UIL or UVL) is used to analyse the surface to detect the presence of consolidant, organic binders, organic colourants and varnishes. A UV radiation is used to excite electrons, which releases light in the visible region when it transforms this absorbed energy in luminescence. A filter will be used that absorbs (read: block) UV and IR light (Dyer, Sotiropoulou 2017, 2; Nocerino et al. 2018, 774; Østergaard, 2018, 7).

Since **ultraviolet fluorescence** (UVf) does not differ from luminescence they have the same principle, but it is used to detect and map residues of organic pigments such as madder lake, which transforms the energy in pink fluorescence and ancient patina and surface treatments. Further, it can be used for a more general status of the object in terms for conservation and for dismissing the presence of organic material (Bracci et al. 2019, 1611;1616-1617; Lanteri, Agresti, Pelosi 2019, 210).

Ultraviolet reflectance (UVR) uses UV emitting lamps to illuminate the object, where the camera contains a UV transmitted lens to block all IR and visible light. It is most often used to reveal the presence of pigment and coatings and strengthens the contrast (Nocerino et al. 2018, 774; Østergaard, 2018, 7). A small example is given in figure 90. Four types of fluorescence could be distinguished: light blue, bright purple, bright and light orange and pale yellow. The light blue fluorescence is being associated with gypsum used as a glue-binder, the bright purple (located at the left side of the drapery) might be a red organic dye, the bright orange at the back of the model is from wax used to seal the relic into the bust, the light orange fluorescence on the collar and base might be from the natural resin used to treat the surface of the wood and the light yellow fluorescence on the face is from a paint binder (Lanteri, Agresti, Pelosi 2019, 212).

Figure 90: UV fluorescence images on 3D model (Lanteri, Agresti, Pelosi 2019, 210, Fig. 2).

1.2. Visible

Visible-induced IR luminescence (VIL) is used to capture the luminescence of pigments and primarily Egyptian blue (figure 91), which has a peak at 950nm and when excited with red light an absorption band at 600-630nm. An object is illuminated with visible light and a camera records the emission of light in the near IR-region. When the pigments emit light in the visible region the method is called **visible-induced visible luminescence** (VIVL), which is more used to detect red and yellow pigments. Most common red pigments detected with VIVL is madder lake (figure 92). Madder lake can be derived from the family of the plant Rubiaceae where *Rubia Peregrina*, *Rubia Tinctorum* and *Rubia Cordifolia* indicates for purpurin (absorption band at 506 and 540 nm and an emission band at 506, 600 and 650 nm() and *Rubia Tinctorum* and Alizarin crimson (absorption band at 500 nm and emission band at 660 nm) (Amadori et al. 2015, 184; 189; Dyer, Sotiropoulou 2017 2-3; Kakoulli et al. 2017, 106; Nocerino et al. 2018, 774; Bracci et al. 2019, 1611).

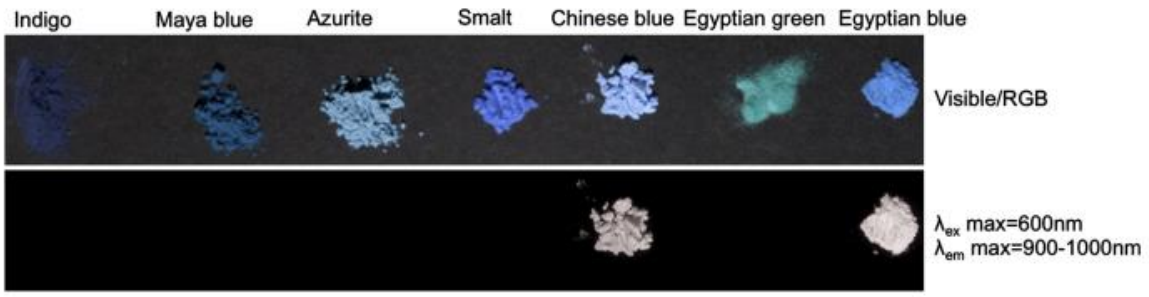

Figure 91: VIL from blue and green pigments (Kakoulli et al. 2017, 110, Fig. 5).

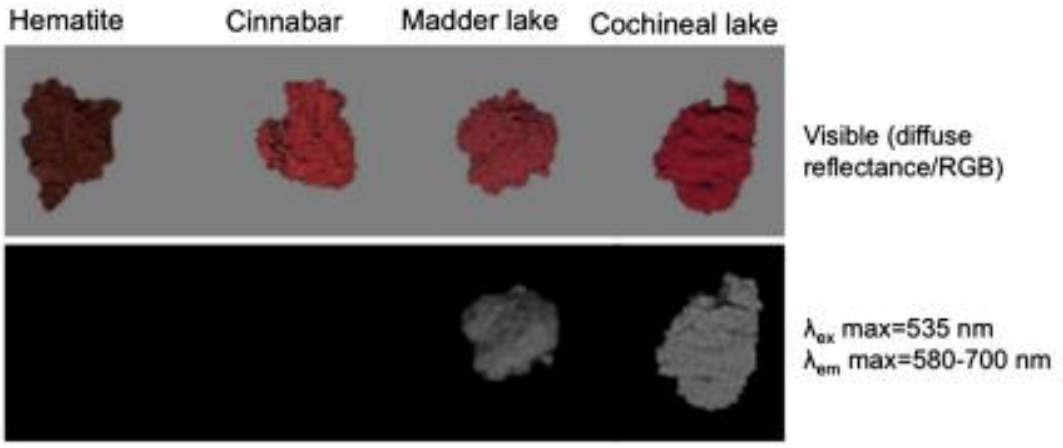

Figure 92: VIVL from red pigments (Kakoulli et al. 2017, 112, Fig. 8).

1.3. Infrared

Infrared reflectography (IRR) is commonly used in archaeology for the detection of underdrawings as a guide for the actual paintings or carvings, cracks and repairs (figure 93). The object will be subjected to IR light. This light will be transmitted and reflected. Carbon-based regions will absorb the (NIR) radiation and appears darker in contradiction to the rest (Sfarra et al. 2017, 289; Nocerino et al. 2018, 774; Lanteri, Agresti, Pelosi 2019, 210).

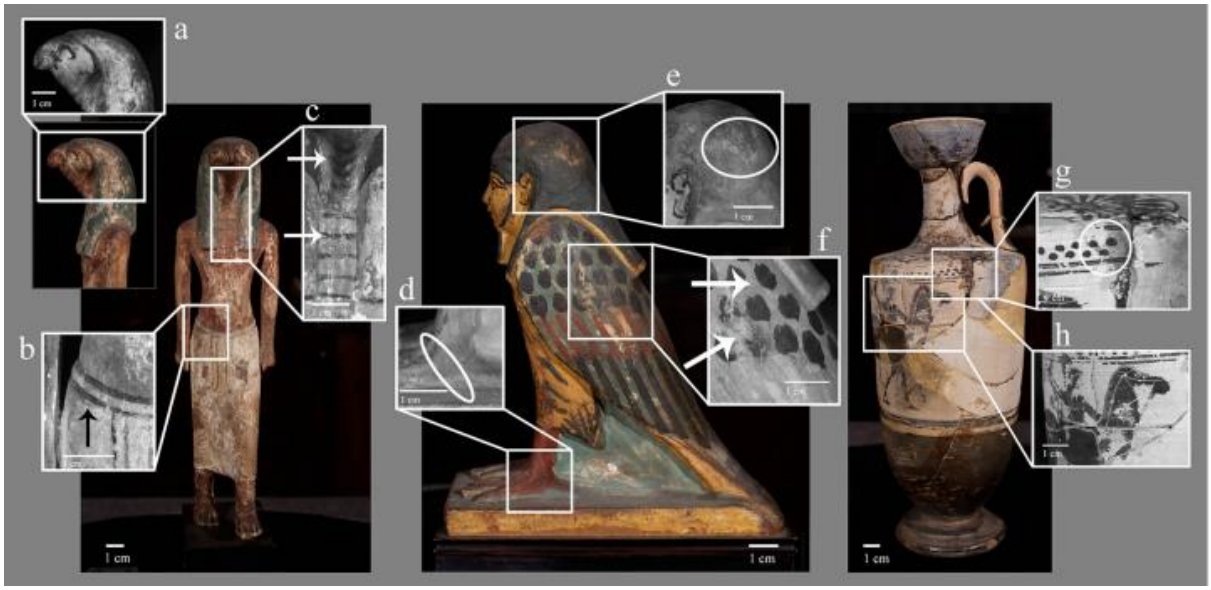

Figure 93: reflected IR images of details of drawings (left), cracks (middle) and reparation (right) (Webb 2017, 6, Fig. 2).

1.4. Combination with 3D modelling

The pipeline of photogrammetry or other 3D modelling methods can be combined with the data acquisition of the multi -and hyperspectral images. In the case of photogrammetry first, the images will be taken with the filters (UV-Vis-IR). These images are then aligned and meshed so a 3D model is generated from the filter images (Mathys, Jadinon, Hallot 2019, 92).

Recently in a study of Hedeaard et al. (2019), they have created a 3D model where the distribution of Egyptian blue is depicted (figure 94).

Figure 94: A 3D model with the distribution of Egyptian blue (Hedeaard et al. 2019, 186, Fig. 4).

1.5. Combination with RTI

Multi -and hyperspectral imaging can also be combined with RTI. Visible and IR-RTI is best for surface and texture analysis for the detection of engravings and colour variations. UV-RTI shows the best result for the detection of repairs, subtle surface variations and usage of varnish (Kotoula 2015, 912-913). With the images, the same software programs as RTI can be used (Watteeuw et al. 2016, 4; Triolo et al. 2019, 5005).

Also used for the detection of tool marks (ancient and modern). For instance in the study of a recurving of Caligula to Claudius variations were detected in the hairline, eyes, neck and ears (bright pink fluorescence) by multispectral imaging (figure 95) but additional RTI showed markings on the right and left cheek (figure 96). Presumably be accidental damage (Pollard 2018, 153; 155).

Figure 95: Roman head under visible, UV and IR light (Pollard 2018, 153, Fig. 8).

Figure 96: RTI images of the right cheek of a Roman head (Pollard 2018, 156, Fig. 11).

2. Identification of the pigments

The identification of the pigments is not new in the field of archaeology, therefore a short explanation of the most commonly used techniques will be given below. Most of them can be used for other application such as provenience studies or in a combined pipeline and are small-scale destructive.

X-ray fluorescence spectroscopy (XRF) uses X-rays or gamma rays to remove electrons so that the electrons arrange themselves to regain a stable structure, in other words, fill the gap. When the electron falls it releases energy characteristic to the element (figure 97). This characteristic of energy is illustrated by a spectrum. The absence or presence of a certain element is representative for the used pigment. For instance, the presence of silicon (Si) and aluminium (Al) often indicates earth colours due to the clay. Sulphur (S) frequently indicates the yellow pigment jarosite (Tsatsouli, Nikolaou 2017, 343; Gasanova et al. 2017, 532; 539; 541; 543, Alfeld et al. 2018, 398).

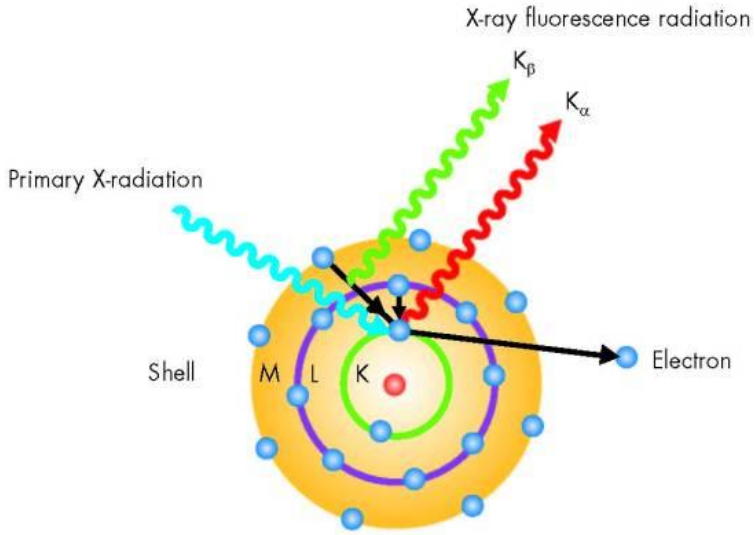

Figure 97: principle of XRF (Fischer 2019, s.d.).

Raman spectroscopy uses laser light to react with the molecules and their bonding. Certain photons will disperse at a different energy than the incident photon. This vibrational movement is called inelastic scattering or Raman effect and once again unique for each molecule. The results are illustrated in the form of a spectrum. These can be compared to known spectra. For instance, the difference between cinnabar (HgS), red ochre (Fe_3O_4 + clay + silica) and haematite (Fe_2O_3) is clear when looking at their respective spectra (figure 98).

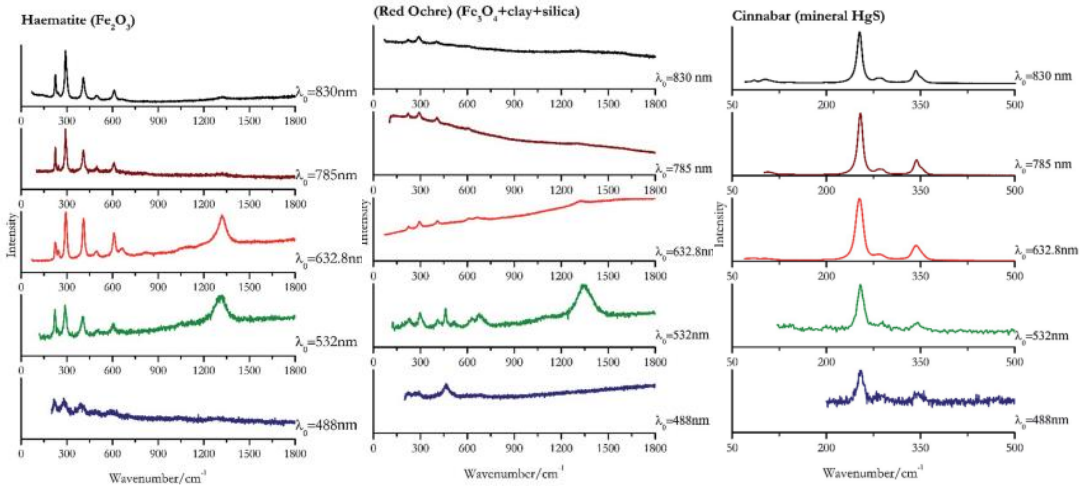

Figure 98: The Raman spectrum of (left) haematite, (middle) red ochre and (right) cinnabar (Marucci et al. 2018, 1227-1228 , Fig. 2, 3 and 6).

Fourier transform infrared spectroscopy (FTIR) or micro-FITR analyses the absorbance of IR light at different wavelengths to detect the molecular composition and structure of the pigment. The resulted spectrum can then be compared with reference samples. For instance, the differences between cinnabar, red ochre and haematite are shown in figure 99 (Khramchenkova et al. 2019, 6; Pronti et al. 2020, Roman wall paintings §1).

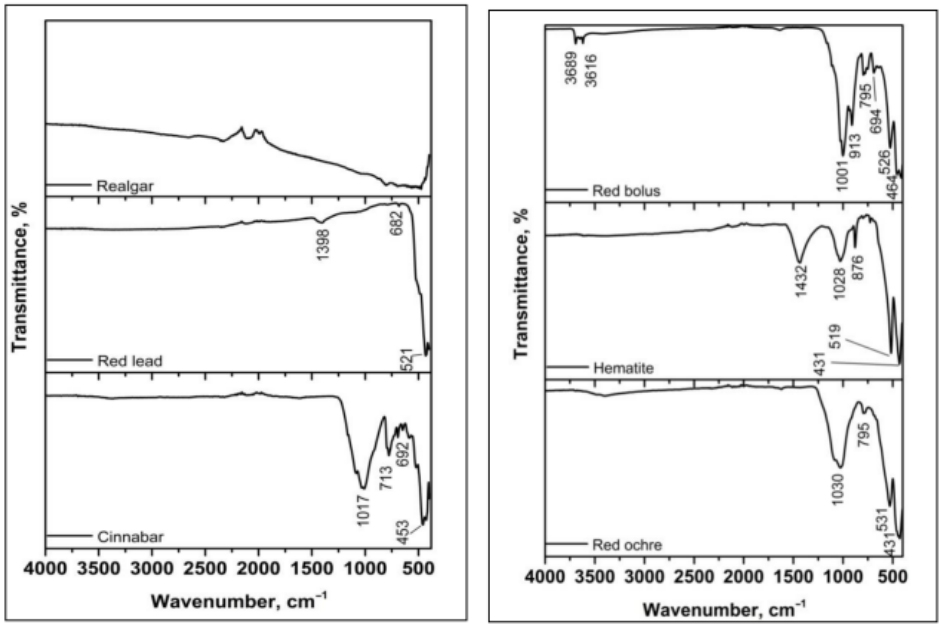

Figure 99: The FTIR spectra of three red pigments (Čiuladienė et al. 2018, 246, Fig. 3 and 4).

Fibre optic (diffuse) reflectance spectroscopy (FO(D)RS) is used for the molecular composition of the pigments by measuring the reflectance spectrum in UV, Vis and NIR spectral range. The obtained spectra are unique for each pigment by analysing the reflectance and absorbance peaks (Cucci, Bigazzi, Picollo 2013, 291; Saint et al. 2018, 234; Radpour, Fischer, Kakoulli 2019, 12; 14-15).

3. Advantages and limitations

Multi- and hyperspectral imaging are highly sensitive and can have accurate recordings of the polychromy. To increase visuality, the best is to place the object in a dark room to lower the influence of ambient light (Dyer, Sotiropoulou 2017, 2; MacDonald et al. 2017, 8; Nocerino et al. 2018, 776). Hyperspectral images have a higher spectral resolution in comparison to multispectral images but consist of more noise (MacDonald et al. 2017, 9; Verhoeven 2018, 3; Howell 2018, 38). The technique is affordable but the software program for processing is more expensive (ENVI) (Cosentino 2015, 2; Howell 2018, 39; Østergaard, 2018, 1). Since it only takes a few minutes to generate images the technique is rather fast (Van der Perre et al. 2016, 166).

The techniques for identification have their own advantage and limitations. XRF is the most frequently used since it is fast and has high accuracy, but it is restricted to elements heavier than magnesium. The best way is to combine different techniques (Brøns, Hedegaard, Sargent 2016, 26; Kokiasmenou et al. 2020, 3; Pronti et al. 2020, Roman wall paintings §1).

4. Its practice in archaeology

A lot of studies have been conducted using multi -and hyperspectral images due to its properties to identify Egyptian blue.

4.1. The tomb of blue demons-Italy

The tomb of the blue demons is located in the Necropolis of Monterozzi in Tarquinia and dates from 450 to 430 BCE. The paintings are very degraded (figure 100) and so multispectral imaging is used to give qualitative information about the used material and assess the readability of the depicted scene (Adinolfi et al. 2019, 450-451).

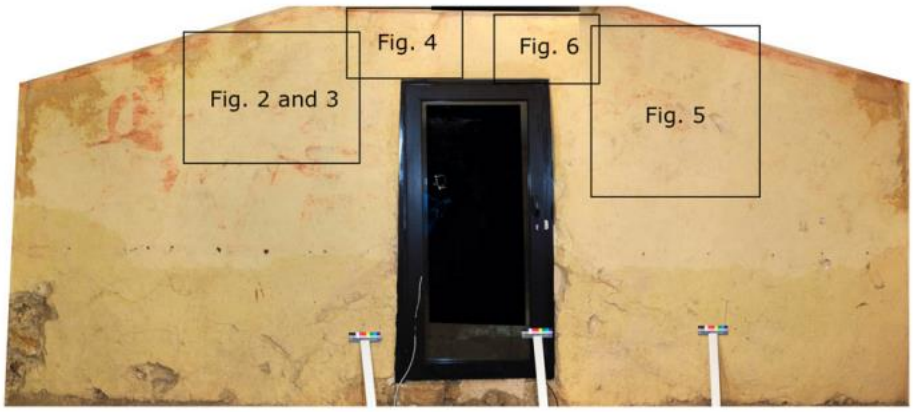

Figure 100: The entrance wall with the locations of five scenes (Adinolfi et al. 2019, 543, Fig. 1).

Figure 101 shows the multispectral image of figure 5. The following elements could be distinguished: a deer, the leg of a hunter (A), a catlike animal (C), possible bird (D) and antlers of a male deer (B). This scene probably illustrates a hunt.

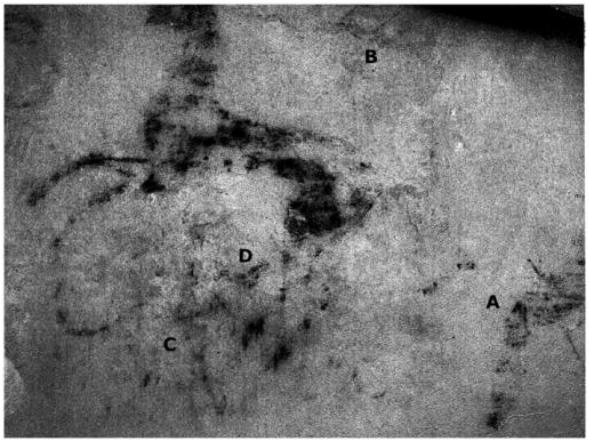

Figure 101: UVf image of figure five located at the left side of the entrance (Adinolfi et al. 2019, 455, Fig. 5).

On figure 102 (representing figure 2 on figure 59) a bright white fluorescence is showing the hair of a person and some small contouring of the body (Adinolfi et al. 2019, 453)

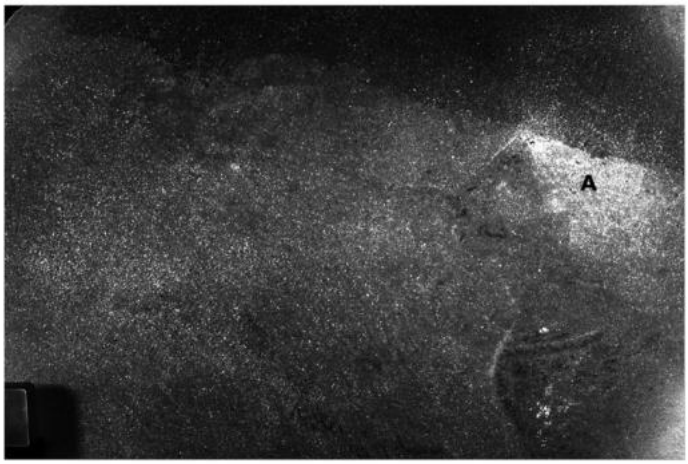

Figure 102: UVf image (750-850 nm) of figure two located at the right side of the entrance (Adinolfi et al. 2019, 454, Fig. 2).

Figure 103 (figure 6 on figure 59) a wild cat (*Caracal caracal)* has been identified by its ears (point 1) and a reddish fur (Adinolfi et al. 2019, 456).

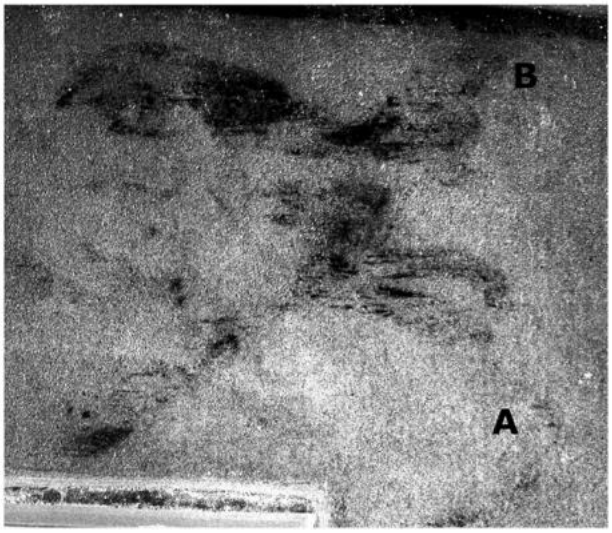

Figure 103: UVf image of figure six located at the top of the entrance (Adinolfi et al. 2019, 456, Fig. 6).

The second scene at the top of the entrance shows a dog (figure 104) who's biting the back of a boar (Adinolfi et al. 2019, 455).

Figure 104: UVf image of figure four located at the top of the entrance (Adinolfi et al. 2019, 455, Fig. 4).

A final scene shows the face of an armed person (A), the front legs of a boar (D), the rear legs of a boar (E), the ear of a boar (C) and its fang (B). On the left side of this boar, a second hunter is present (Adinolfi et al. 2019, 454).

Where the other walls of the tombs are a representation of the Etruscan afterlife where the demons escort the dead towards Hades (Adinolfi et al. 2019, 450), the wall at the entrance represent two hunting scenes with landscape elements such as leaves, bushes, plants and Myrtus (figure).

4.2. The palace of Nestor-Greece

The Palace of Nestor in Pylos holds house several interesting aspects of the Mycenaean royal way of living. Close to the palace the famous "Griffin Warrior Tomb" has been found. The palace itself dates from the Late Helladic IIIB period and contains numerous wall-paintings on the interior and exterior, mostly applied with a secco and tempera technique (Kokiasmenou et al. 2020, 1).

The following scenes are located in Hall 64, located in the southeast corner of the palace. The first scene depicts a battle scene between several warriors in a hand-to-hand battle (figure 105). Compared to the naval scene more colour is used. Quite exceptional is the use of Murex purple (presence of bromine) as a background colour. The garments and weaponry of the warriors are white and have black patterns and is painted on top of the skin. The skin colour is dark brown. The borders are three straight lines in blue, red and orange with underneath a black and white square pattern

(Kokiasmenou et al. 2020, 2;11). Macroscopic XRF is used for the identification of the composition of the used pigments. The brown-reddish skin colour contains iron from the iron-based ochres. The black colouring is attributed to manganese-based minerals. Traces of copper are detected around the warriors and originates from Egyptian blue (Kokiasmenou et al. 2020, 7-8). Information on the application of the different pigments can be made when looking at missing elements in the XRF-spectrum. Since there was no evidence of copper in the traces of the warriors, it could be that the warriors were painted directly onto the white background and afterwards the purple background was applied (Kokiasmenou et al. 2020, 9).

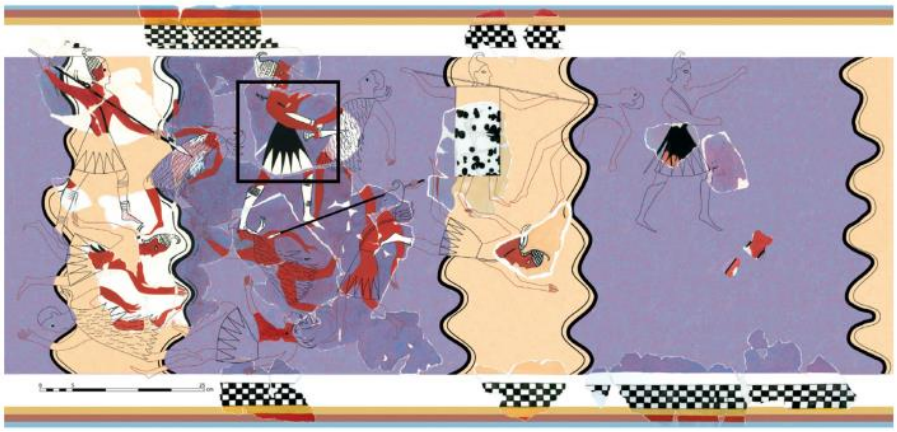

Figure 105: The reconstruction of the battle scene (Kokiasmenou et al. 2020, 3, Fig. 2).

The second scene depicts a naval scene (figure 106). Here three Mycenaean ships, who slightly overlap, are sailing from left to right. For the ground layer, a homogeneous white (calcium) layer is attributed. Once again purple is used for the background. The ships are constructed with different tones of yellow and brown ochres, where the darker tones are used for outlining the elements. A zig-zag lined decorated hull of the third ship could be distinguished. The edges here are similar to the battle scene (Kokiasmenou et al. 2020, 2; 7).

Figure 106: the reconstruction of the naval scene and fragments used for macroscopic XRF (Kokiasmenou et al. 2020, 2, Fig. 1).

When looking closely to the macroscopic XRF images the spatial variation of iron and copper could be closer examined. Diverse new information has come to light, revealing the brush strokes and details of the ship (Kokiasmenou et al. 2020, 5). Ia and Ib (figure 107) show a fish, the shape of the deck and hull and a figure in the cabin of the ship with detailed facial features. This scene tells more about the aspect of humans possible to be inside cabins in the actual seafaring Mycenaean world (Kokiasmenou et al. 2020, 7).

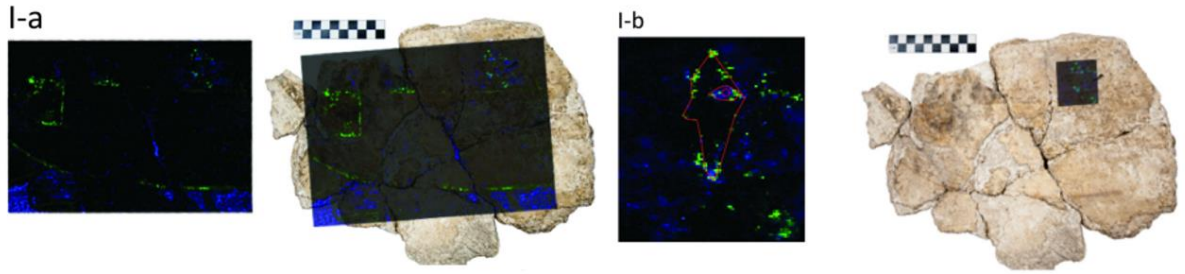

Figure 107: The spatial variation of iron (green) and copper (blue) for fragment Ia and b (to: Kokiasmenou et al. 2020, 6;8, Fig. 6 and 7).

IIa and b (figure 108) shows more information about the position and shape of the oar and rudders and the presence of a fish swimming in close contact with the ship (Kokiasmenou et al. 2020, 7).

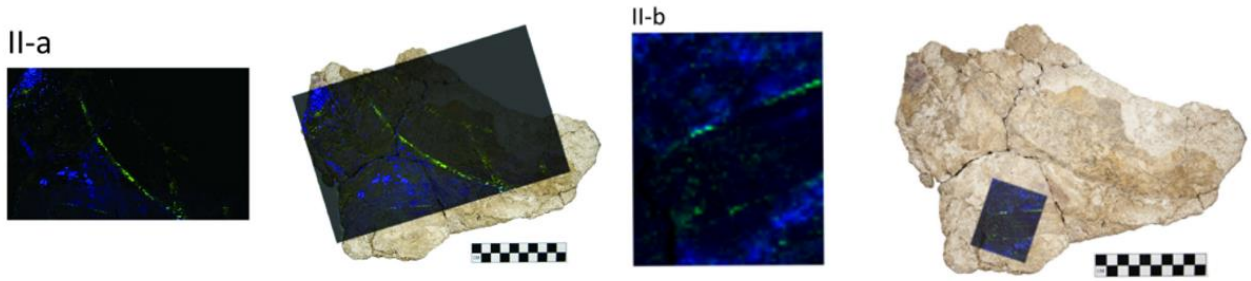

Figure 108: The spatial variation of iron (green) and copper (blue) for fragment IIa and b (to: Kokiasmenou et al. 2020, 6;8, Fig. 6 and 7).

IIIa and b (figure 109) gives as well information about the rudders but also insights in the exact style used for the geometric decorative pattern, where it can be seen that the artist tried to create an impression of depth (Kokiasmenou et al. 2020, 7)

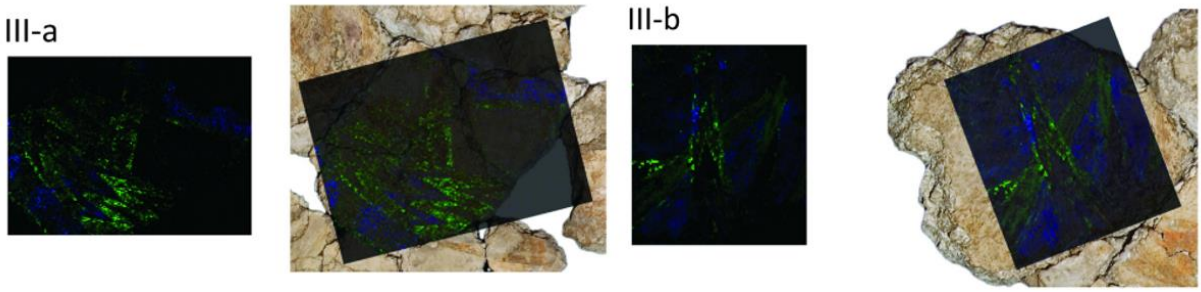

Figure 109: The spatial variation of iron (green) and copper (blue) for fragment IIIa and b (to: Kokiasmenou et al. 2020, 6, Fig. 6).

The same approach of painting can be seen in the naval scene, where first the ships are painted onto the white plaster and afterwards the purple background (Kokiasmenou et al. 2020, 7).

In both mural paintings, the purple colour is obtained in some areas by a mixture of Egyptian blue, yellow ochre, black pigment and an organic colourant of Murex purple. The use of Murex purple is often linked with wealth and restricted to important rooms (Kokiasmenou et al. 2020, 7). When looking at the application technique of this purple background there is a difference between the two scenes: where the background in the battle scene is constructed through superimposition of pictorial layers to produce the mixture, the one of the naval scene is produced by directly mixing Egyptian blue with Murex purple (Kokiasmenou et al. 2020, 9).

4.3. Wall painting-Palestine

Roman wall paintings from Caesarea Maritima on the eastern Mediterranean coast dating from the Herodian to the late Roman period are analysed with optical microscopy, SEM-EDS, XRD, micro-FTIR and micro-Raman to determine the used technology, material and function (Linn 2017, 774-775). The detection of lime suggest a fresco technique used to outline the composition, but a secco technique is present as well in form of thick lines. Further analysis revealed underdrawings in red ochres, colour is obtained by layering the different pigments or by mixtures (Linn 2019, 779-780).

4.4. Marble figurines-Greece

Five marble figurines (figure 110) and two marble statues dating from the Early Cycladic I and II period are analyzed by XRF and VIS-NIR FODRS to detect and identify pigments. Currently these objects are stores din the National Archaeological Museum of Athens (Saint et al. 2018, 234).

Figure 110: the five marble object from the Early Cycladic Period (Saint et al. 2018, 234, Fig. 23.1).

4.5. Painted fragments-Israel

In the study of Linn, Cline and Yasur-Landau (2017, 466-474) Aegean-style painted fragments from Tel Kabri in Western Galilee (Israel) are used to gain information in the colour palette, painting techniques and the stratigraphy of the layers by optical microscopy, RTI, VIL, XRF, Micro-Raman and FTIR spectroscopy. With RTI is was more clear where incision where located to outline the border of the decoration, but there is also evidence of more free-style. Here a snapped line is also present and is quite an unique feature. Fingernail imprints and brush strokes were detected on the plaster (indicating a fresco technique) and on the paint. The used colour palette was restricted to five colours

VII. Results

In this chapter the findings of this thesis will be discussed.

1. Techniques

In the attachment, a summary table of each technique its assets are given. It is clear that all of them can be used for every type of figurative art but that different features or properties are analysed. When assessing an object three characteristics can be measured: colour, texture and geometry (figure 111). To receive a full understanding of the object these must be covered (unless the research question revolves around a specific topic).

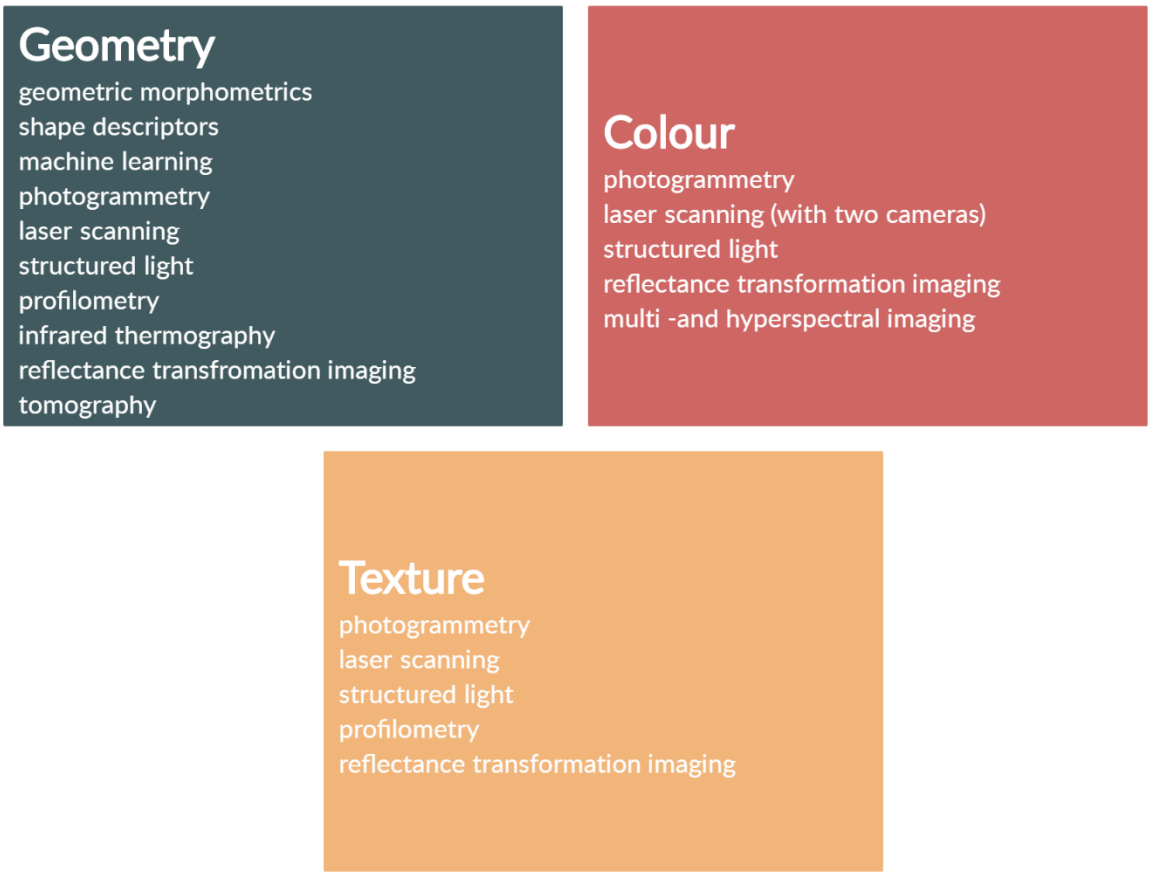

Figure 111: The three characteristics of an object

This does not mean that when applying one technique of each property all the information about the object is gathered. For instance, profilometry is used for a 3D micro-topographical model, whereas photogrammetry is used to generate a 3D model. Or profilometry can be used to assess roughness and generate a 3D map of

the incision on specific regions, whereas RTI detects marks on the object at once by using variations in light and shadow.

It is also visible that most of the techniques can be applied in the same pipeline and in result reducing the time and cost of the analysis, since similar apparatus is used, such as a dSLR camera. When only images of the object are present photogrammetry can be used to generate a 3D model (the more images the better the accuracy). If the model has a high accuracy 3D micro-profiles can be made and tool marks or incision can be studied. Variations between or within groups are possible by extracting pictorial elements or the object as a whole with machine learning, shape descriptors or geometric morphometrics. Different surface rendering models can be made with RTI and textures such as fingerprints, hidden images or brush strokes are visualized. If it is possible to use the object itself, everything can be used.

The main problem with most of these techniques is the cost of the equipment and the software. More and more free software and open sources are available but this at the expense of the resolution or processing time and the complexity of some might appear unattractive to use. Software and programs usually require a capable operator and the need for standardization are present.

With the techniques in this thesis, the following information can be obtained: manufacturing process, variations within and between groups and new information. The manufacturing process can be analysed with thermal IR when it involves bronze materials, aspects such as repairs, cracks and coldworking are detectable even the depth of these defects can be measured. In the case of paintings, it is possible to detect the different layers (plaster or canvas) or structural aspects (nails or wooden support) For other types of material it is often used for conservation. Profilometry is used for the micro-topography of the surface, aspects such as use-wear, marks or cracks are detectable. Even a quantitative assessment about the roughness parameters is possible. RTI is used to enhance surface properties by changing the light angle. Toolmarks, fingerprints and hidden images can be visualised. Tomography gives more insight into the inside of an object. It is possible to detect cracks, to measure the wall thickness (of a hollow object) and to 'peel' an object layer by layer. Multi -and

hyperspectral images and pigment detection can give information about the way of painting.

Variations within and between groups are based on geometric morphometrics, shape descriptors and machine learning. These are useful to detect patterns between small and large datasets and possibly detecting trade networks or similar ideologies when images are recurrent. It is even possible to link a seal with its impression.

New information can be obtained with the already mentioned techniques. The opportunity to visualize or analyse an object with a big part of the EM-spectrum makes it possible to gain as much information as possible.

2. Figurative art

When looking at the given case studies (once again keep in mind that this is just a small dataset of the actual papers about new techniques) it can be concluded that in general statues and figurines are the most studied (figure) and reliefs and seals less.

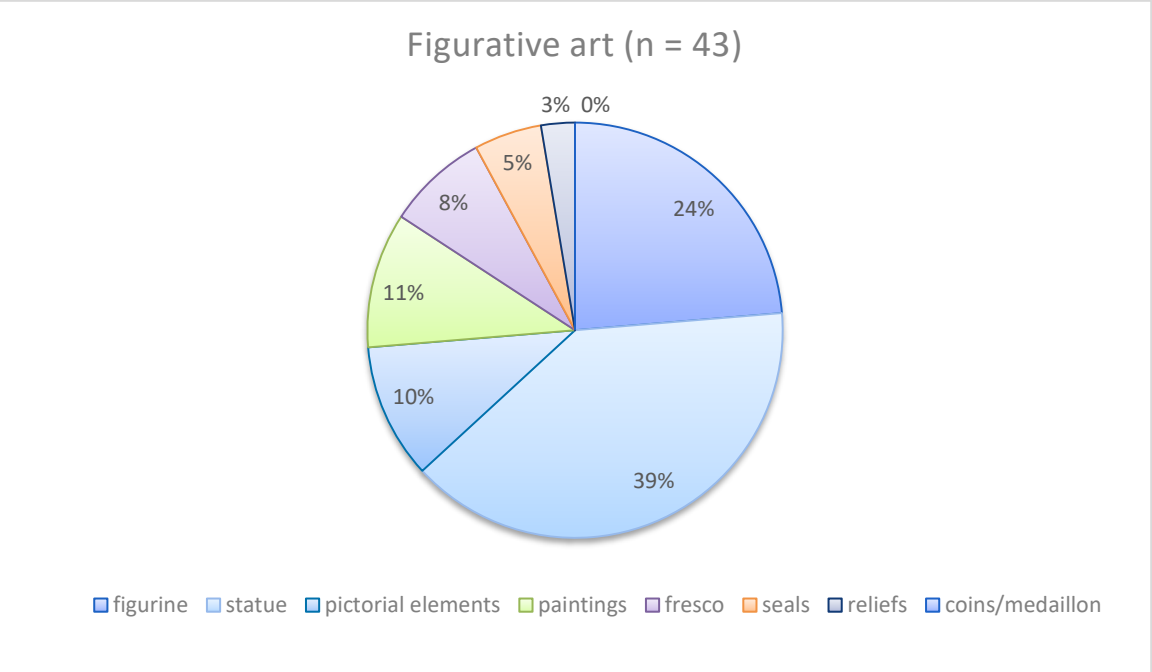

Figure 112: Pie chart of the mentioned figurative art.

This might be because of the higher information potential and the easy accessibility since most of them are either in a museum or in the open air. When studying figurines and statues different aspects can be measured: the manufacturing process (especially for bronze with IRT), the presence of colour on marble statues, corrosion

processes, conservation, equipment and provenance study. But then again all this information can be gathered on the other figurative art. It probably depends on the research question.

3. Geographical context

In this thesis, case studies from the Mediterranean, Cyprus and the Near East are used to evaluate the use of new techniques. In figure the spread of the sites from the case studies can be seen, with exception of Teotihuacan (number 1) and Arnhem Land (number 3). This is only a selected range and are therefore not representative for an overall assessment. Still when going through most of the papers and books it was clear that in the Mediterranean more studies are present with different techniques, especially on bronze statues, probably because there are more bronze figurative art in this region. In Cyprus and the Near East most case studies revolves around colour and more precisely Egyptian blue and red madder. This is because VIL and VIVL can detect these two pigments with high accuracy.

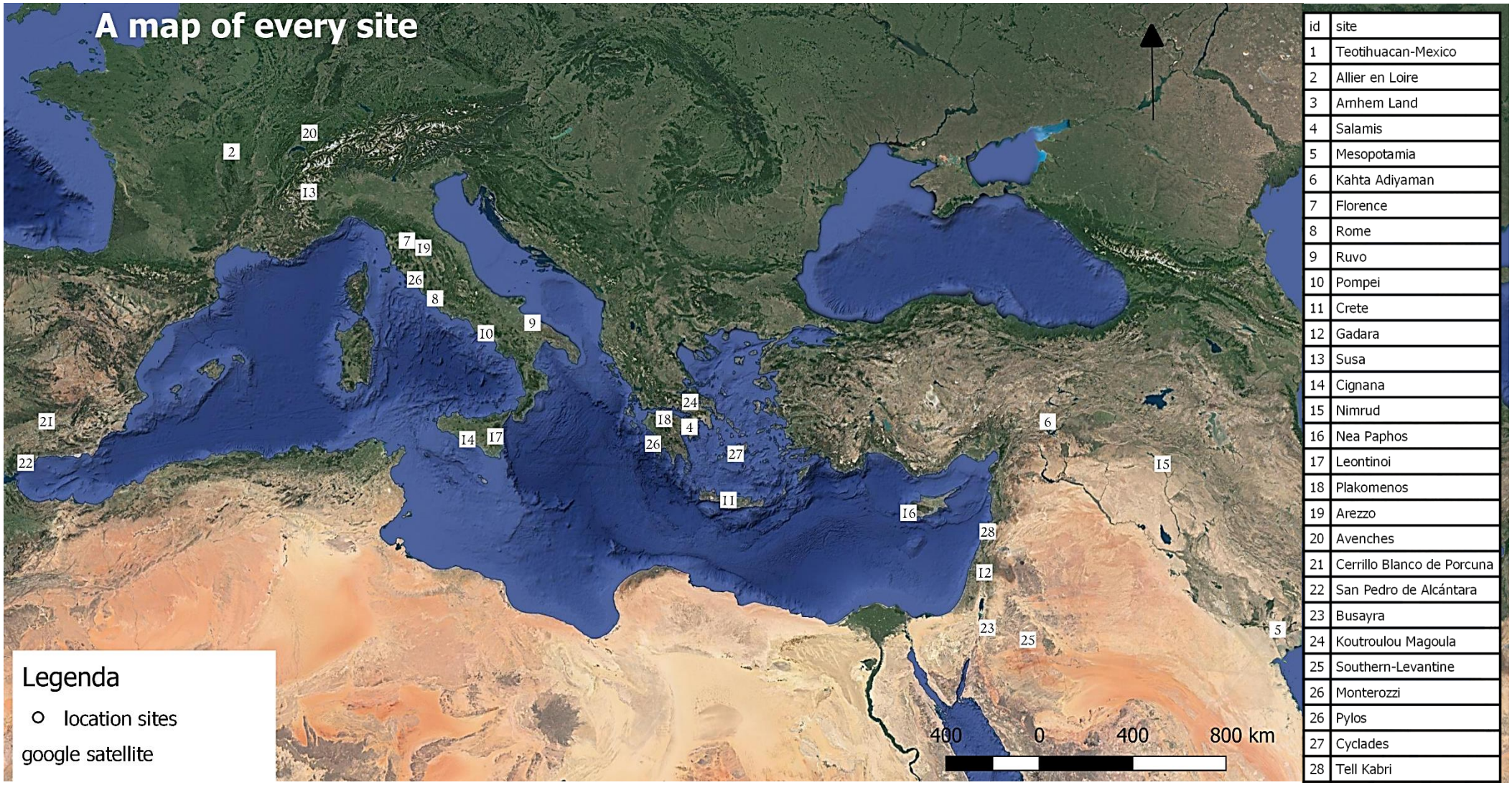

id	site
1	Teotihuacan-Mexico
2	Allier en Loire
3	Arnhem Land
4	Salamis
5	Mesopotamia
6	Kahta Adiyaman
7	Florence
8	Rome
9	Ruvo
10	Pompei
11	Crete
12	Gadara
13	Susa
14	Cignana
15	Nimrud
16	Nea Paphos
17	Leontinoi
18	Plakomenos
19	Arezzo
20	Avenches
21	Cerrillo Blanco de Porcuna
22	San Pedro de Alcántara
23	Busayra
24	Koutroulou Magoula
25	Southern-Levantine
26	Monterozzi
26	Pylos
27	Cyclades
28	Tell Kabri

Figure 113: A map with every site mentioned in this thesis and the corresponding sites (QGIS).

VIII. Conclusion

The role of an archaeologist is to strive to as much information as possible to interpret the situation or role of the object as good as possible (of course the human role of the creator is not measurable) and since Archaeometry is an evolving field, so will the techniques. The need for a more standardised 'pipeline' is necessary, since the techniques have either a complex theoretical background or a complex data processing software not to mention the cost. Before starting with the analyses it is therefore important to make an assessment of which technique can be best combined with another to gain full knowledge without increasing time and cost. Here most techniques have a high accuracy (almost all micrometre levels) and similar equipment can be used such as a dSLR camera with additional filters. Bigger apparatus such as a CT scan, profilometer or scanning devices are more expensive but considering their advantages it is profitable. The fact that these are new techniques might result in a higher cost and for now more complex theory. When more scientists use a certain technique it will increase its use and in result its function. For now each of these techniques demand a certain knowledge, several days of work, a high cost but in result information of a high accuracy and a high level.

IX. Bibliography

Adams D.C., Rohlf F.J., Slice D.E., 2004. Geometric morphometrics: ten years of progress following the 'revolution', *Italian journal of zoology* 71, 5-16.

Adinolfi G., Carmagnola R., Cataldi M., Marras L., Palleschi V., 2019. Recovery of a lost wall painting at the Etruscan tomb of the blue demons in Tarquinia (Viterbo, Italy) by multispectral reflectometry and UV fluorescence imaging, *Archaeometry* 61/2, 450-458.

Alfeld M., Mulliez M., Devogelaere J., de Viguerie L., Jockey P., Walter P., 2018. MA-XRF and hyperspectral reflectance imaging for visualizing traces of antique polychromy on the Frieze of the Siphnian Treasury, *Microchemical Journal* 14, 395-403.

Almasri E., Alshawabkeh Y., Balaawi F., Shwater A., 2017. An enthroned tyche statue from Gadara/Umm Qais, Jordan, *Acta Historiae Artium* 58, 5-20.

Amadori M.L., Barcelli S., Poldi G., Ferrucci F., Andreotti A., Baraldi P., Colombini M.P., 2015. Invasive and non-invasive analyses for knowledge and conservation of Roman wall paintings of the Villa of the Papyri in Herculaneum, *Microchemical Journal* 118, 183-192.

Ambrosini D., Daffara C., Di Biase R., Paoletti D., Pezzati L., Bellucci R., Bettini F., 2010. Integrated reflectography and thermography for wooden paintings diagnostics, *Journal of Cultural Heritage* 11, 196-204.

Antonelli F., Colivicchi F., Lazzzarini L., 2017. Craftmanship and Identity in the Hellenistic Funerary Reliefs of Naples: an Archaeological and Archaeometric Analysis, *Archaeometry* 59/1, 1-12.

Arico A.F., Greene N.E., Parker H.D.D., 2016. Ancient Near Eastern Material Culture Studies and Reflectance Transformation Imaging, in: Chalikias K., Beeler M., Pearce A., Renette S (eds.), *THE FUTURE OF THE PAST; From Amphipolis to Mosul, New Approaches to Cultural Heritage Preservation in the Eastern Mediterranean*, (No Publisher), 61-68.

Arslan A.E., Kalkan K., 2013. Comparison of working efficiency of terrestrial laser scanner in day and night condition, *International Archives of the Photogrammetry, Remote Sensing and Spatial Information Sciences* XL-7/W2, 19-21.

Artal-Isbrand P., Klausmeyer P., Murray W., 2011. An Evaluation of Decorative Techniques on a Red-Figure Attic Vase from the Worcester Art Museum using Reflectance Transformation Imaging (RTI) and Confocal Microscopy with a Special Focus on the "Relief Line", *MRS Online Proceeding Library Archive* 1319, 3-33.

Asscher Y., Angelini I., Secco M., Parisatto M., Chaban A., Deiana R., Artialo G., 2019. Combining multispectral imaging with X-ray fluorescence to quantify the distribution of pigments in the frigidarium of the Sarno Baths, Pompei, *Journal of Cultural Heritage* 40, 317-323.

Attanasio D., Bruno M., Prochaska W., Yavuz A.B., 2020. Comments on the paper "*Petrography and mineralogy of the white marble and black stone of Göktepe (Muğla, Turkey) used in antiquity: New data for provenance determination*" by M. Brilli, M.P. Lapuente Mercadal, F. Giustini and H. Royo Plumed (JAS Reports 2018, 19, 625-642), *Journal of Archaeological Science* 30, 1-5.

Avdelidis N.P., Delegou E.T. Almond D.P., Moropoulou A., 2004. Surface roughness evaluation of marble by 3D laser profilometry and pulsed thermography, *NDT&E International* 37, 571-575.

Azarpay G., 1990. A Photogrammetric Study of Three Gudea Statues, *Journal of the American Oriental Society* 110/4, 660-665.

Bai F., Zhang X., Tian C., 2016. Surface roughness measurement with laser triangulation, *SPIE Proceedings* 9684, 1-5.

Barceló J.A., 2010. Visual Analysis in Archaeology. An Artificial Intelligence Approach, in: Elewa A.M.T., (ed.), *Morphometrics for Nonmorphometricians*, Berlin: Springer, 93-156.

Barrile V., Fotia A., 2018. 3D Modeling by thermography for non-destructive analysis of archaeological heritage, *Instrumentation, Mesure, Métrologie* 17/3, 393-410.

Baylac M., Frieß M., 2005. Fourier Descriptors, Procrustes Superimposition, and Data Dimensionality: An Example of Cranial Shape Analysis in Modern Human Population, in: Slice D., (ed.), *Modern Morphometrics in Physical Anthropology*, New York: Springer, 145-166.

Baysan A., Sleibi A., Ozel B., Anderson P., 2018. The quantification of surface roughness on root caries using Noncontact Optical Profilometry-An in vitro study, *Lasers in Dental Science* 2, 229-237.

Bendada A., Sfarra S., Ambrosini D., Paoletti D., Ibarra-Castanedo C., Maldague X.P.V., 2010. Active thermography data processing for the NDT&E of frescoes, *10th International Conference on Quantitative InfraRed Thermography*, 1-6.

Bengio Y., Goodfellow I., Courville A., (eds.), 2015. *Deep Learning*, Cambridge: MIT Press.

Berto S., Salemi G., 2019. "Old and low-cost sensor" for microphotogrammetry. Case study: the emperor *Maximianus Herculeus*' medallion at the Correr museum (Venice), *The International Archives of the Photogrammetry, Remote Sensing and Spatial Information Sciences* XLII-2/W17, 61-68.

Bici M., Campana F., Colacicchi O., D'Ercoli G., 2018. CAD-CAE methods to support restoration and museum exhibition of bronze statues: the "Principe Ellenistico", *IOP Conference Series: Materials Science and Engineering* 364, 1-10.

Bogojevic N., 2012. Optical Systems for 3D Scanning, *Mechanics Transport Communication* 10/3, 20-26.

Bookstein F.L., (ed.), 1991. *Morphometric tools for landmark data. Geometry and biology*, Cambridge: Cambridge University Press.

Bookstein F.L., 1996/7. Landmark methods for forms without landmarks: morphometrics of group differences in outline shape, *Medical Image Analysis* 1/3, 225-243.

Bourdeu A., Pitzalis D., 2010. Geometric morphometrics for provenance determination of Gallo-Roman white clay figurines, *The 11th International Sympoisum on Virtual Reality, Archaeology and Cultural Heritage VAST*, 25-31.

Bracci S., Vettori S., Cantisani E., Degano I., Galli M., 2019. The ancient use of colouring on the marble statues of Hierapolis of Phrygia (Turkey): an integrated multi-analytical approach, *Archaeological and Anthropological Sciences* 11, 1611-1619.

Brecoulaki H., 2014. "Precious colours" in ancient Greek polychromy and paintings: material aspects and symbolic values, *Revue Archaeologique* 1, 1-35.

Brøns C., Hedegaard S.S., Sargent M.L., 2016. Painted Faces: Investigations of Polychromy on Etruscan Antefixen in the Ny Carlsberg Glyptotek, *Etruscan Studies* 19/1, 23-67.

Brutto M.L., Dardanelli G., 2017. Vision metrology and Structure from Motion for archaeological heritage 3D reconstruction: a Case Study of various Roman mosaics, *Acta Imeko* 6/3, 35-44.

Burger W., Burge M.J., (eds.), 2016. *Digital Image Processing. An Algorithmic Introduction Using Java*, Londen: Spinger-Verlag.

Buxeda I Garrigós J., Gordaliza A.V., 2011. Morphometrics and compositional classes. The study of anthropomorphic sculptures from Teotihuacan (México), *Proceedings of the 4th International Workshop on Compositional Data Analysis*, 1-21.

Calandra I., Schunk L., Rodriguez A., Gneisinger W., Pedergnana A., Paixao E., Pereira T., Iovita R., Marreiros J., 2019. Back to the edge: relative coordinate system for use-wear analysis, *Archaeological and Anthropological Sciences* 11, 5937-5948.

Campione I., Lucchi F., Santopuoli N., Seccia L., 2020. 3D Thermal Imaging System with Decoupled Acquisition for Industrial and Cultural Heritage Applications, *Applied Science* 10/828, 1-20.

Canul-Ku M., Hasimoto-Beltran R., Jiménez-Badillo D., Ruiz-Correa S., Román-Rangel E., 2019. Classification of 3D Archaeological Objects Using Multi-View Curvature Structure Signature, *IEEE-Access* 7, 3298-3313.

Carcagni P., Daffara C., Fontana R., Gambino M.C., Mastroianni M., Mazzotta C., Pampaloni E., Pezzati L., 2005. Optical micro-profilometry for archaeology, *Optical Metrology*, s.p.

Carrero-Pazos M., Vilas-Estévez B., Vázquez-Martínez A., 2018. Digital imaging techniques for recording and analysing prehistoric rock art panels in Galicia (NW Iberia), *Digital Applications in Archaeology and Cultural Heritage* 8, 35-45.

Castellini P., Martarelli M., Lenci S., Quagliarini E., Silani M., Matellone A., 2017. Diagnostic Survey on Frescoes Paintings in Pompei by Active IR-Thermography, *IMEKO*, 51-56.

Chen C., Gao N., Wang X., Zhang Z., Gao F., Jiang X., 2018. Generic exponential fringe model for alleviating phase error in phase measuring profilometry, *Optics and Lasers in Engineering* 110, 179-185.

Čiuladienė A., Luckutė A., Kiuberis J., Kareiva A., 2018. Investigation of the chemical composition of red pigments and binding media, *Chemija* 29/4, 243-256.

Cobden R., Clarkson C., Price G.J., David B., Geneste J.-M., Delannoy J.-J., Barker B., Lamb B., Gunn R.G., 2017. The identification of extinct megafauna in rock art using geometric morphometrics: A *Genyornis newtoni* painting in Arnhem Land, northern Australia?, *Journal of Archaeological Science* 87, 95-107.

Collins T., Woolley S.I., Gehlken E., Ch'ng E., 2019. Automated Low-Cost Photogrammetric Acquisition of 3D Models from Small Form-Factor Artefacts, *Electronics* 8/1441, 1-17.Comelli D., Capogrosso V., Orsenigo C., Nevin A., 2016. Dual wavelength excitation for time-resolved photoluminescence imaging of painted ancient Egyptian objects, *Heritage Science* 4/21, 1-8.

Cooke S.B., Terhune C.E., 2015. Form, Function, and Geometric Morphometrics, *The Anatomical Record* 298, 5-28.

Cosano D., Dara Mateos L., Jiménez-Sanchidrián C., Ruiz J.R., 2017. Identification by Raman microspectroscopy of pigments in seated statues found in the Torreparedones Roman archaeological site (Baena, Spain), *Microchemical Journal* 130, 191-197.

Cosentino A., 2015. Multispectral imaging of pigments with a digital camera and 12 interferential filters, *e-Preservation Science* 12, 1-7.

Coules H.E., Orrock P.J., Seow C.E., 2019. Reflectance Transformation Imaging as a tool for engineering failure analysis, *Engineering Failure Analysis* 105, 1006-1017.

Counts D.B., Averett E.W., Garstki K., 2016. A fragmented past: (re)constructing antiquity through 3D artefact modelling and customised structured light scanning at Athienou-*Malloura*, Cyprus, *Antiquity* 90/349, 206-218.

Cucci C., Bigazzi L., Picollo M., 2013. Fibre Optic Reflectance Spectroscopy as a non-invasive tool for investigating plastcs degradation in contemporary art collections: A methodological study on an expanded polystyrene artwork, *Journal of Cultural Heritage* 14, 290-296.

Dahl J.L., Hare J.S., Kelley K., Martinez K., Young D., 2018. A structured light approach to imaging ancient Near Eastern cylinder seals: how efficient 3D imaging may facilitate corpus-wide research, in: Kelley K., Wood R.K.L., (eds.), *Digital Imaging of Artefacts: Developments in Methods and Aims*, 49-74.

Delegou E.T., Avdelidis N.P., Karaviti E., Moropoulou A., 2008. NDT&E techniques and SEM-EDS for the assessment of cleaning interventions on Pentelic marble surfaces, *X-Ray Spectrometry* 37, 435-443.

Díaz-Guardamino M., Wheatley D., 2013. Rock art and digital technologies: the application of reflectance transformation imaging (RTI) and 3D laser scanning to the study of late Bronze age Iberian stelae, *Menga. Revista de Prehistoria de Andalucía*, 187-203.

Dibiasie Sammons J.F., 2018. Application of Reflectance Transformation Imaging (RTI) to the study of ancient graffiti from Herculaneum, Italy, *Journal of Archaeological Science* 17, 184-194.

Di Ludovico A., 2018. Data Description and the Integrated Study of Ancient Near Eastern Works of Art: The Potential of Cylinder Seals, in: Clivaz C., Hamidovoć D., (eds.), *Digital Biblical Studies*, Leiden: Brill, 85-110.

Di Tuccio M.C., Ludwug N., Gargano M., Bernardi A., 2015. Thermographic inspection of cracks in the mixed materials statue: Ratto delle Sabine, *Heritage Science* 3/10, 1-8.

Dommergues C.H., Dommergues J.-L., Verrecchia E.P., 2007. The Discrete Cosine Transform, a Fourier-related Method for Morphometric Analysis of Open Contours, *Mathematical Geology* 39/8, 749-763.

Donadio E., Sambuelli L., Spanò A., Pichi D., 2018. Three-Dimensional (3D) Modelling and Optimization for Multipurpose Analysis and Representation of Ancient Statues, in: Gonzalez-Aguilera D., (ed.), *Latest Developments in Reality-Based 3D Surveying and Modelling*, Basel: MDPI Books, 95-118.

Duan Y., Zhang H., Sfarra S., Avdelidis N., Loutas T.H., Sotiriadis G., Kostopoulos V., Fernandes H., Petrescu F.I., Ibarra-Castanedo C., Maldague X.P.V., 2019. On the

Use of Infrared Thermography and Acousto-Ultrasonics NDT Techniques for Ceramics-Coated Sandwich Structures, *Energies* 12, 1-12.

Dumoncel J., 2017. *Analyse morphométrique 3D de structure pour la paléoanthropologie*, Doctoral thesis Université de Toulouse, (No publisher).

Dyer J., Sotiropoulou S., 2017. A technical step forward in the integration of visible-induced luminescence imaging methods for the study of ancient polychromy, *Heritage Science* 5/24, 1-21.

Earl G., Beale G., Martinez K., Pagi H., 2010. Polynomial texture mapping and related imaging technologies for recording, analysis and presentation of archaeological materials, *International Archives of Photogrammetry, Remote Sensing and Spatial Information Sciences* XXXVIII/part 5, 218-223.

Earl G., Martinez K., Malzbender T., 2010. Archaeological applications of polynomial texture mapping: analysis, conservation and representation, *Journal of Archaeological Science* 37, 2040-2050.

Ebolese D., Lo Brutto M., Burgio A., 2017. 3D modeling of two *Louteria* fragments by image-based appraoach, *The International Archives of the Photogrammetry, Remote Sensing and Spatial Information Sciences* XLII-5/W1, 573-580.

Errickson D., Grueso I., Griffith S.J., Setchell J.M., Thompson T.J.U., Thompson C.E.L., Growland R.L., 2017. Towards a Best Practice for the Use of Active Non-contact Surface Scanning to Record Human Skeletal Remains from Archaeological Contexts, *International Journal of Osteoarchaeology* 27, 650-661.

Elfarargy M., Rizq A., Rashwan M., 2013. 3D Surface Reconstruction Using Polynomial Texture Mapping, *Proceedings, Part I, of the 9th International Symposium on Advances in Visual Computing* 8033, 353-362.

Elgammal A., Liu B., Kim D., Elhoseiny M., 2018. The Shape of Art History in the Eyes of the Machine, *The Thirty-Second AAAI Conference on Artificial Intelligence*, 2183-2191.

Evans A.A., Maxwell M.L., Cuickshanks G.L., 2012. From lidar to LSCM: micro-topographies of archaeological finds, in: Optiz R.S., Cowley D.C., (eds.), *Interpreting Archaeological Topography. Airborne laser scanning, 3D data and ground observation*, Oxford: Oxbow books, 123-135.

Falconer K., (ed.), 2014. *Fractal Geometry. Mathematical Foundations and Applications*, Chichester: Wiley & Sons Ltd.

Feng S., Chen Q., Gu G., Tao T., Zhang L., Hu Y., Yin W., Zuo C., 2020. Fringe pattern analysis using deep learning, *Advanced Photonics* 1/2, 1-7.

Fioretti G., Raneri S., Pinto D., Mignozzi M., Mauro D., 2020. The archaeological site of St. Maria Veterana (Triggiano, Southern Italy): Archaeometric study of the wall paintings for the historical reconstruction, *Journal of Archaeological Science* 29, 1-17.

Fiorini A., 2018. Il metodo fotografico RTI (reflectance transformation imaging) per la documentazione delle superfici archeologiche. L'applicazione ai materiali di età protostorica, *Archaeologia e Calcolatori* 29, 241-258.

Fiorucci M., Khoroshiltseva M., Pontil M., Traviglia A., Del Bue A., James S., 2020. Machine Learning for Cultural Heritage: A Survey, *Pattern Recognition Letters* 133, 102-108.

Fischer-Cripps A.C., (ed.), 2020. *Waves, Particles and Fields. Introducing Quantum Field Theory*, Boca Raton: CRC Press.

Fontana R., Greco M., Materazzi M., Pampaloni E., Pezzati L., Rocchini C., Scopigno R., 2002. Three-dimensional modelling of statues: the Minerva of Arezzo, *Journal of Cultural Heritage* 3, 325-331.

Fontana R., Gambino M.C., Greco M., Pampaloni E., Pezzati L., Scopigno R., 2003. High-resolution 3D digital models of artworks, *Proceedings SPIEE-Optical Metrology of Arts and Multimedia* 5146, 34-43.

Fort R., Vazquez-Calvo C., Chapa T., Martínez-Navarrete M.I., Belén M., 2013. An analytical study of Iberian Iron Age stone sculptures and their surface marks, *Archaeometry* 55/3, 391-406.

Fu S., Cheng F., Tjahjowidodo T., Zhou Y., Butler D., 2018. A Non-Contact Measuring System for In-Situ Surface Characterization Based on Laser Confocal Microscopy, *Sensors* 18/2657, 1-15.

Fulminante F., Unavane M., 2020. "Community practices" and "communities of practice" in smelting technology by XRF analysis of Archaic bronze votive figurines in central Italy (6th – 5th centuries BC), *Journal of Archaeological Science* 31, 1-13.

Gapinski B., Wieczorowski M., Marciniak-Podsadna L., Dybala B., Ziolkowksi G., 2014. Comparison of Different Method of Measurement Geometry using CMM, Optical Scanner and Computed Tomography 3D, *Procedia Engineering* 69, 255-262.

Garrido I., Lagüela S., Arias P., 2018. Infrared Thermography's Application to Infrastructure Inspections, *Infrastructures* 3/35, 1-19.

Gasanova S., Pagès-Camagna S., Andrioti M., Lemasson Q., Brunel L., Doublet C., Hermon S., 2017. Polychromy analysis on Cypriot Archaic statues by non- and micro-invasive analytical techniques, *Archaeometry* 59/3, 528-546.

Gasanova S., Pagès-Camagna S., Andrioti M., Hermon S., 2018. Non-destructive in situ analysis of polychromy on ancient Cypriot sculptures, *Archaeological and Anthropological Science* 10, 83-95.

Gautron P., Krivanek J., Pattanaik S., Bouatouch K., 2004. A Novel Hemispherical Basis for Accurate and Efficient Rendering, *Eurographics Symposium on Rendering*, 321-330.

Giesko T., Zbrowski A., Czajka P., 2007. Laser profilometers for surface inspection and profile measurement, *Problemy Eksploatacji* 1, 97-108.

Goldman Y., Linn R., Shamir O., Weinstein-Evron M., 2018. Micro-RTI as a novel technology for the investigation and documentation of archaeological textiles, *Journal of Archaeological Science* 19, 1-10.

Granero L., Díaz F., Domínguez R., Hervás J., Simón S., Pérez E., 2009. Application of optical techniques in documentation and identification of archaeological rests: the case study of the roman bronze rest found in Lucentum, *Proceedings of SPIE-Optics for Arts, Architecture and Archaeology II* 7391, 1-11.

Grilli E., Özdemir E., Remondino F., 2019. Application of Machine and Deep Learning Strategies for the Classification of Heritage Point Clouds, *The International Archives of the Photogrammetry, Remote Sensing and Spatial Information Sciences,* XLII-4/W18, 447-454.

Gühring J., 2001. Dense 3-D surface acquisition by structured light using off-the-shelf components, *Proceedings of SPIE-Videometrics and Optical Methods for 3D Shape Measurement* 4309, 220-231.

Hammer Ø., Spocova J., 2013. Virtual whitening of fossils using polynomial texture mapping, *Palaeontologia Electronica* 16/2, 1-10.

Hedeaard S.B., Brøns C., Drug I., Saulins P., Bercu C., Jakovlev A., Kjaer L., 2019. Multispectral Photogrammetry: 3D models highlighting traces of paint on ancient sculptures, *Proceedings of the 4th Conference of the Association of Digital Humanities in the Nordic Countries*, 181-189.

Herzlinger G., Goren-Inbar N., Grosman L., 2017. A new method for 3D geometric morphometric shape analysis: The case study of handaxe knapping skill, *Journal of Archaeological Science: Reports* 14, 163-173.

Herzlinger G., Grosman L., 2018. *AGMT3-D*: A software for 3-D landmarks-based geometric morphometric shape analysis of archaeological artifacts, *PLoS ONE* 13/11, 1-17.

Hess M., MacDonald L.W., Valach J., 2018. Application of multi-modal 2D and 3D imaging and analytical techniques to document and examine coins on the example of two Roman silver denarii, *Heritage Science*, 6/5, 1-22.

Hidalgo-Gato R., González de Ulloa L., Andrés J.R., Marínez J.R., Pérez A., Madruga F.J., López-Higueza J.M., 2015. A thermographic step-heating technique for metallic pollutant detection in soils, *Infrared Physics & Technology* 69, 191-197.

Hixon S.W., Lipo C.P., Hunt T.L., Lee C., 2017. Using Structure from Motion Mapping to Record and Analyze Details of the Colossal Hats (*Pukao*) of Monumental Statues on Rapa Nui (Easter Island), *Advances in Archaeological Practice*, 1-16.

Howell D., 2018. The potential of hyperspectral imaging for researching colour on artefacts, in: Kelley K., Wood R.K.L., (eds.), *Digital Imaging of Artefacts: Developments in Methods and Aims*, Summertowns: Archaeopress, 37-48.

Hunziker-Rodewald R., Fornaro P., 2019. RTI Images for Documentation in Archaeology: The Cas of the Iron Age Female Terracotta Figurines from Buṣayra, Jordan, *Journal of Eastern Mediterranean Archaeology and Heritage Studies* 7/2, 188-204.

Ibáñez J.J., Lazuen T., González-Urguijo J., 2019. Identifying Experimental Tool Use Through Confocal Microscopy, *Journal of Archaeological Method and Theory* 26, 1176-1215.

Ibarra-Castanedo C., Genest M., Piau J.-M., Guibert S., Bendada A., Maldague X.P.V., 2007. Active Infrared Thermography Techniques for the Nondestructive testing of Materials, in: Chen C.H., (ed.), *Ultrasonic and Advanced Methods for Nondestructive Testing and Material Characterization*, Singapore: World Scientific Publishing, 325-348.

Kable S., 2019. Basic Principle of Fluorescence, in: Cox G., (ed.), *Fundamentals of Fluorescence Imaging,* Singapore: Jenny Stanford Publishing, 1-34.

Kakoulli I., Radpour R., Lin Y., Svoboda M., Fischer C., 2017. Application of forensic photography for the detection and mapping of Egyptian blue and madder lake in Hellenistic polychrome terracotta's based on their photophysical properties, *Dyes and Pigments* 136, 104-115.

Kanaan H., Behrad A., 2020. Three-Dimensional Shape Recognition and Classification Using Local Features of Model Views and Sparse Representation of Shape Descriptors, *Journal of Information Processing Systems* 16/2, 343-359.

Kaplonek W., Sutowska M., Ungureanu M., Çetinkaya K., 2018. Optical profilometer with confocal chromatic sensor for high-accuracy 3D measurements of the uncirculated and circulated coins, *Journal of Mechanical and Energy Engineering* 2(42)/3, 181-192.

Kardjilov N., Lehmann E., Strobl M., Woracek R., Manke I., 2017. Neutron Imaging, in: Kardjilov N., Festa G., (eds.), *Neutron Methods for Archaeology and Cultural Heritage*, Cham: Springer International Publishing, 329-349.

Kazmi I.K., You L., Zhang J.J., 2013. A Survey of 2D and 3D Shape Descriptors, *10th International Conference Computer Graphics, Imaging and Visualization*, 1-10.

Khramchenkova R., Safina I., Drobyshev S., Batasheva S., Nuzhdin E., Fakhrullin R., 2019. Advanced Microscopy Techniques for Nanoscale Diagnostic of Cultural Heritage: Scanning Electron Microscopy for Investigation of Medieval Coins and Frescos From the Republic of Tartarstan, in: Lazzara G., Fakhrullin R. (eds.), *Nanotechnologies and Nanomaterials for Diagnostic, Conservation and Restoration of Cultural Heritage*, Amsterdam: Elsevier, 1-23.

Kim Y.H., Choi J., Lee Y.Y., Ahmed B., Lee K.H., 2016. Reflectance Transformation Imaging Method for Large-scale Objects, *Proceedings IEEE: 13th International Conference Computer Graphics, Imaging and Visualization*, 84-87.

Kim P., (ed.), 2017. *MALAB. Deep Learning. With Machine Learning, Neural Networks and Artificial Intelligence*, New York: Apress.

Klingenberg C.P., 2016. Size, shape, and form: concepts of allometry in geometric morphometrics, *Developmental Genes and Evolution* 226, 113-137.

Kolobova K.A., Fedorchenko A.Y., Basova N.V., Postnov A.V., Kovalev V.S., Christyakov P.V., Molodin V.I., 2019. The Use of 3D-Modeling for Reconstruction the Appearance and Function of Non-Utilitarian Items (the Case of Anthropomorphic Figurines from Tourist-2, *Archaeology, Ethnology & Anthropology of Eurasia* 47/4, 66-76.

Kokiasmenou E., Caliri C., Kantarelou V., Karydas A.G., Paolo Romano F., Brecoulaki H., 2020. Macroscopic XRF imaging in unravelling polychromy on Mycenaean wallpaintings from the Palace of Nestor at Pylos, *Journal of Archaeological Science* 29, 1-12.

Kotoula E., Kyranoudi M., 2013. Study of Ancient Greek and Roman coins using Reflectance Transformation Imaging, *E-conservation* 25, 75-88.

Kotoula E., 2015. Reflectance Transformation Imaging Beyond the Visible: Ultraviolet Reflected and Ultraviolet Induced Visible Fluorescence, *Keep the Revolution Going. Proceedings of the 43rd Annual Conference on CAA*, 909-918.

Kotoula E., Robinson D.W., Bedford C., 2018. Interactive relighting, digital image enhancement and inclusive diagrammatic representations for the analysis of rock art superimposition: The main Pleito cave (CA, USA), *Journal of Archaeological Science* 93, 26-41.

Krieger J.D., 2010. Controlling for Curvature in the Quantification of Leaf Form, in: Elewa A.M.T., (ed.), *Morphometrics for Nonmorphometricians*, Berlin: Springer, 27-71.

Kuhl F.P., Giardina C.R., 1982. Elliptical Fourier Features of a Closed Contour, *Computer Graphics and Image Processing* 18, 236-258.

Laga H., Guo Y., Tabia H., Fisher R.B., Bennamoun M., (eds.), 2019. *3D Shape Analysis. Fundamentals, Theory, and Applications*, Hoboken: John Wiley & Sons Inc.

Lanteri L., Agresti G., Pelosi C., 2019. A New Practical Approach for 3D Documentation in Ultraviolet Fluorescence and Infrared Reflectography of Polychromatic Sculptures as Fundamental Step in Restoration, *Heritage* 2, 207-215.

Laureti S., Colantonio C., Burrascano P., Melis M., Calabrò G., Malekmohammadi H., Sfarra S., Ricci M., Pelosi C., 2019a. Development of integrated innovative techniques for paintings examination: The case studies of *The Resurrection of Christ* attributed to Andrea Mantegna and the *Crucifixion* of Viterbo attributed to Michelangelo's workshop, *Journal of Cultural Heritage* 40, 1-16.

Laureti S., Malekmohammadi H., Rizwan M.K., Burrascano P., Sfarra S., Mostacci M., Ricci M., 2019b. Looking Through Paintings by Combining Hyper-Spectral Imaging and Pulse-Compression Thermography, *Sensors* 19, 1-24.

Lawing A.M., Polly P.D., 2009. Geometric morphometrics: Recent applications to the study of evolution and development, *Journal of Zoology*, 1-7.

Lecoutre A., Negrevergne B., Yger F., 2017. Recognizing Art Style Automatically in painting with deep learning, *Proceedings of Machine Learning Research* 77, 327-342.

Lehmann E.H., 2017. Neutron Imaging Facilities in Global Context, *Journal of Imaging* 3/52, 1-11.

Lele S.R., 1993. Euclidian Distance Matrix Analysis (EDMA): Estimation of mean form and mean form difference, *Mathematical Geology* 25/5, 573-602.

Lele S.R., Richtsmeier J.T. (eds.), 2001. *An Invariant Approach to Statistical Analysis of Shapes*, Florida: Chapman & CRC.

Lele S.R., McCulloch C.E., 2002. Invariance, Identifiability, and Morphometrics, *Journal of the American Statistical Association* 97/459, 796-806.

Li X., Tao N., Sun J.G., Lei Y., Qu L., Gao F., He Y., Wang G., Feng L., 2019. Evaluation of an ancient cast-iron Buddha head by step-heating infrared thermography, *Infrared Physics and Technology* 98, 223-229.

Li X., Zeng Y., Gong Y., 2019. Chronological Classification of Ancient Paintings of Mogao Grottoes Using Convolutional Neural Networks, *IEEE 4th International Conference on Signal and Image Processing*, 51-55.

Linn R., 2017. Layered pigments and painting technology of the Roman wall paintings of Caesarea Maritima, *Journal of Archaeological Science* 11, 774-781.

Linn R., Cline E.H., Yasur-Landau A., 2017. Technological study of Middle Bronze Age painted plaster fragments from the Canaanite Palace of Tel Kabri, Israel – materials and painting techniques, *Journal of Archaeological Science* 13, 466-475.

Liu Y., Wu J.-Y., Liu K., Wen H.-L., Yao Y., Sfarra S., Zhao C., 2019. Independent component thermography for non-destructive testing of defects in polymer composites, *Measurement Science and Technology* 30, 1-10.

Liverani P., Bracci S., Iannaccone R., Lenzi S., Magrini D., Mazzei B., 2018. Colours in the Dark: New Research into Catacombs, in: Bracci S., Giachi G., Liverani P., Pallecchi P., Paolucci F., (eds.), *Polychromy in Ancient Sculpture and Architecture*, Livorno: Sillabe, 111-122.

López G.L., Pérez Negrón A.P., Jiménez A.D.A., Rodríguez J.R., Paredes R.I., 2017. Comparative analysis of shape descriptors or 3D objects, *Multimedia Tools and Applications* 76, 7663-7040.

Macdonald D.A., Harman R., Evans A.A., 2018. Replicating surface texture: Preliminary testing of molding compound accuracy for surface measurements, *Journal of Archaeological Science* 18, 839-846.

Macdonald D.A., Xie L., Gallo T., 2019. Here's the dirt: First applications of confocal microscopy for quantifying microwear on experimental ground stone earth working tools, *Journal of Archaeological Science* 26, 1-10.

MacDonald L., Robson S., 2010. Polynomial texture mapping and 3D representations, *International Archives of Photogrammetry, Remote Sensing and Spatial Information Sciences* XXXVIII, 422-427.

MacDonald L.W., 2015. Representation of Cultural Objects by Image Sets with Directional Illumination, in: Trémeau A., Schettini R., Tominaga S., (eds.), *CCIW: International Workshop on Computational Color Imaging-Computational Color Imaging* LNCS 9016, Cham: Springer, 43-56.

MacDonald L.W., Vitorino T., Picollo M., Pillay R., Obarzanowski M., Sobczyk J., Nascimento S., Linhares J., 2017. Assessment of multispectral and hyperspectral imaging systems for digitization of a Russian icon, *Heritage Science* 5/41, 1-16.

Magnani M., Douglass M., Porter S.T., 2016. Closing the seams: resolving frequently encountered issues in photogrammetric modelling, *Antiquity* 90/354, 1654-1669.

Maher M., 2020. X-RAY computed tomography of a late period falcon bronze coffin, *Radiation Physics and Chemistry* 166, 1-7.

Malešević B., Obradović R., Banjac B., Jovović I., Makragić M., 2013. Application of polynomial texture mapping in process of digitalization of cultural heritage, *ArXIV* 1312.6935, s.p., https://arxiv.org/abs/1312.6935.

Malzbender T., Gelb D., Wolters H., 2001. Polynomial texture maps, *SIGGRAPH '01: Proceedings of the 28th annual conference on Computer graphics and interactive techniques*, 519-528.

Makris D., Skaltsas I., Fotiou S., Karampinis L., Vlachou M.A., 2018. Digitization of Athens School of Fine Arts artworks based on optical 3-D Scanning and Photogrammetry, *9th International Conference on Information, Intelligence, Systems and Applications*, 1-7.

Mantovan L., Nanni L., 2020. The computerization of archaeology: survey on AI techniques, *arXIV* 2005.02863, 1-47, https://arxiv.org/abs/2005.02863.

Marcus L.F., Corti M., 1996. Overview of the new, or geometric morphometrics, in: Marcus L.F., Corti M., Loy A., Naylor G.J.P., Slice D.E., (eds.), *Advances in Morphometrics*, Boston: Springer, 1-14.

Marrugo A.G., Pineda J., Romero L.A., Vargas R., Meneses J., 2018. Fourier Transform Profilometry in LabVIEW, in: Asadpour V., (ed.), *Digital Systems*, London: IntechOpen, 3-22.

Marshall M.E., Johnson A.A., Summerskill S.J., Baird Q., Esteban E., 2019. Automating photogrammetry for the 3D digitization of small artefact collections, *The International Archives of the Photogrammetry, Remote Sensing and Spatial Information Sciences,* XLII-2/W15, 751-757.

Martin-Garin B., Lathuillière B., Verrecchia E.P., Geister J., 2007. Use of fractal dimensions to quantify coral shape, *Coral Reefs* 3, 541-550.

Marucci G., Beeby A., Parker A.W., Nicholson C.E., 2018. Raman spectroscopic library of medieval pigments collected with five different wavelengths for investigation of illuminated manuscripts, *Analytical Methods* 10, 1219-1236.

Marziali S., Dionisio G., 2017. Photogrammetry and Macro Photography. The Experience of the MUSINT II Project in the 3D Digitization of Small Archaeological Artifacts, *Studies in Digital Heritage* 1/2, 298-309.

Maset E., Fusiello A., Crosilla F., Toldo R., Zorzetto D., 2017. Photogrammetric 3D building reconstruction from thermal images, *ISPRS-Annals of the Photogrammetry, Remote Sensing and Spatial Information Sciences* IV-2/W3, 25-32.

Maté-González M.Á., Aramendi J., Yravedra J., Blasco R., Rosell J., González-Aguilera, Domínguez-Rodrigo M., 2017. Assessment of statistical agreement of three techniques for the study of cut marks: 3D digital microscope, laser scanning confocal microscopy and micro-photogrammetry, *Journal of Microscopy* 267/3, 356-370.

Mathys A., Jadinon R., Hallot P., 2019. Exploiting 3D multispectral texture for a better feature identification for cultural heritage, *The International Annals of the*

Photogrammetry, Remote Sensing and Spatial Information Sciences, IV-2/W6, 91-97.

McCafferty D.J., 2007. The value of infrared thermography for research on mammals: previous applications and future directions, *Mammal Review* 37/3, 207-223.

McPherron S.P., Gernat T., Hublin J.-J., 2009. Structured light scanning for high-resolution documentation of *in situ* archaeological finds, *Journal of Archaeological Science* 36, 19-24.

Meola C., Boccardi S., Carlomagno G.M., 2016. An Excursus on Infrared Thermography Imaging, *Journal of Imaging* 2/23, 2-16.

Mercuri F., Zammit U., Orazi N., Paoloni S., Marinelli M., Scudieri F., 2011. Active infrared thermography applied to the investigation of art and historic artefacts, *Journal of Thermal Analysis and Calorimetry* 104, 475-485.

Mercuri F., Orazi N., Zammit U., Giuffredi A., Stefano Salerno C., Cicero C., Paoloni S., 2017a. The manufacturing process of the Capitoline She Wolf: a thermographic method for the investigation of repairs and casting faults, *Journal of Archaeological Science* 14, 199-207.

Mercuri F., Paoloni S., Orazi N., Cicero C., Zammit U., 2017b. Pulsed infrared thermography applied to quantitative characterization of the structure and the casting faults of the Capitoline She Wolf, *Applied Physics A* 123/327, 1-9.

Mercuri F., Orazi N., Paoloni S., Cicero C., Zammit U., 2017c. Pulsed Thermography Applied to the Study of Cultural Heritage, *Applied Sciences* 7, 1-19.

Mercuri F., Buonora P., Cicero C., Helas P., Manzari F., Marinelli M., Paoloni S., Pasqualucci A., Pinzari F., Romani M., Terrei A., Verdi O., Verona Rinati G., Zammit U., Orazi N., 2018a. Metastructure of illuminations by infrared thermography, *Journal of Cultural Heritage* 31, 53-62.

Mercuri F., Caruso G., Orazi O., Zammit U., Cicero C., Alessandri O.C., Ferretti M., Paoloni S., 2018b. Interface thermal conductance characterization by infrared thermography: a tool for the study of insertions in bronze ancient Statuary, *Infrared Physics & Technology* 90, 31-39.

Mercuri F., Caruso G., Orazi N., Zammit U., Ceccarelli S., Cicero C., Vadrucci M., Paoloni S., 2020. Depth-Resolved Analysis of Double-Layered Cultural Heritage Artifacts by Pulsed Thermography, *International Journal of Thermophysics* 41/6, 1-11.

Miles J., Mavrogordato M., Sinclair I., Hinton D., Boardman R., Earl G., 2016. The use of computed tomography for the study of archaeological coins, *Journal of Archaeological Science* 6, 35-41.

Mital G., Dobránsky J., Ružbarský J., Olejárova Š., 2019. Application of Laser Profilometry to Evaluation of Surface of the Workpiece Machined by Abrasive Waterjet Technology, *Applied Science* 9/2134, 1-14.

Montani I., Sapin E., Sylvestre R., Marquis R., 2012. Analysis of Roman pottery *graffiti* by high resolution capture and 3D laser profilometry, *Journal of Archaeological Science* 39, 3349-3353.

Monteiro L.R., Guillermo L.H., Rivera L.A., Di Beneditto A.P.M., 2004. Geometric methods combining contour and landmark information in the statistical analysis of biological shape, *Proceedings of the Third Brazilian Symposium on Mathematical and Computational Biology*, 336-355.

Morello R., De Capua C., 2016. Thermography for non-invasive diagnosis of conservation state of archaeological discoveries, 6th Symposium on *Environmental Instrumentation and Measurements*, 26-29.

Morita M.M., Novoa F.D., Bilmes G.M., 2019. Reflectance transformation imaging. First applications in cultural heritage in Argentina, *Journal of Archaeological Science* 26, 1-5.

Morris C., Peatfield A., O'Neill B., 2018. 'Figures in 3D': Digital Perspectives on Cretan Bronze Age Figurines, *Open Archaeology* 4, 50-61.

Munaro M., Wai Yan So E., Tonello S., Menegatti E., 2015. Efficient completeness inspection using real-time 3D color reconstruction with a dual-laser triangulation system, *Integrated Imaging and Vision Techniques for Industrial Inspection*, 201-225.

Mytum H., Peterson J.R., 2018. The Application of Reflectance Transformation Imaging (RTI) in Historical Archaeology, *Historical Archaeology* 52, 489-503.

Neiß M., Sholts S.B., Wärmländer S.K.T.S., 2016. New applications of 3D modeling in artefact analysis: three case studies of Viking Age brooches, *Archaeological and Anthropological Science* 8, 651-662.

Nguyen H., Maclagan S.J., Nguyen T.D., Nguyen T., Flemons P., Andrews K., Ritchie E.G., Phung D., 2017. Animal Recognition and Identification with Deep Convolutional Neural Network for Automated Wildlife Monitoring, *International Conference on Data Science and Advanced Analytics*, 40-49.

Nocerino E., Rieke-Zapp D.H., Trinkl E., Rosenbauer R., Farella E.M., Morabito D., Remondino F., 2018. Mapping VIS and UVL imagery on 3D geometry for non-invasive, non-contact analysis of a vase, *The International Archives of the Photogrammetry, Remote Sensing and Spatial Information Sciences,* XLII-2, 773-780.

Omar T., Nehdi M.L., 2016. Data acquisition technologies for construction progress tracking, *Automation in Construction* 70, 143-155.

Orazi N., 2020. The study of artistic bronzes by infrared thermography: A review, *Journal of Cultural Heritage* 42, 280-289.

Orazi N., Mercuri F., Zammit U., Paoloni S., Marinelli M., Giuffredi A., Salerno C.S., 2015. Thermographic analysis of bronze sculptures, *Studies in Conservation*, 1-9.

Orazi N., Paoloni S., Zammit U., Cicero C., Ferretti M., Caruso G., Colacicchi Alessandri O., Paris R., Mercuri F., 2018. Thermographic Investigation of Bronze Artefacts: Characterization of Structure Elements and Casting Faults in Masterpieces of the Bronze Statuary of Rome, *International Journal of Thermophysics* 39/141, 1-10.

Orazi N., Mercuri F., Zammit U., Cicero C., Colacicchi Alessandri O., Brinkmann V., Caruso G., Ferretti M., Paoloni S., 2019. The Boxer at Rest and the Hellenistic Prince: A comparative thermographic study, *Journal of Archaeological Science* 24, 115-121.

Page M.J., Boust C., Mélard N., Robcis D., Obein G., 2016. 3D surface acquisition: comparison of two microtopographic equipments when measuring materials of cultural heritage, *Commission Internationale de L'Eclairage*, 111-120.

Pan R., Tang Z., Xu S., Da W., 2017. Normals and texture fusion for enhancing orthogonal projections of 3D models, *Journal of Cultural Heritage* 23, 33-39.

Papadopoulos C., Hamilakis Y., Kyparissi-Apostolika N., Díaz-Guardamino M., 2019. Digital Sensoriality: The Neolithic Figurines from Koutroulou Magoula, Greece, *Cambridge Archaeological Journal* 29/4, 625-652.

Papantoniou G., Loizides F., Lanitis A., Michaelides D., 2012. Digitization, Restoration and Visualization of Terracotta Figurines from the 'House of Orpheus', Nea Paphos, Cyprus, *EuroMed*, 543-550.

Pavel C., Constantin F., Suciu C.I., Bugoi R., 2012. X-ray tomographic examinations of Teleac, Cicău and Apulum rattles, *Proceedings of the 39th International Symposium for Archaeometry*, 193-197.

Pavel C., Suciu C., Constantin F., Bugoi R., 2013. X-ray computed tomography investigations of Cucuteni ceramics statuettes, *Documenta Praehistorica* XL, 323-332.

Pedergnana A., Ollé A., Evans A.A., 2020. A new combined approach using confocal and scanning electron microscopy to image surface modifications on quartzite, *Journal of Archaeological Science* 30, 1-14.

Peng F., Lin S.C., Guo J., Wang H., Gao X., 2017. The Application of SfM Photogrammetry Software for Extracting Artifact Provenience from Paleolithic Excavation Surfaces, *Journal of Field Archaeology* 42/4, 326-336.

Perea A., Gutiérrez-Neira C., Climent-Font A., 2018. Archaeometric Investigation of a Hellenistic Golden Funerary Belt: a Case Study, *Mediterranean Archaeology and Archaeometry* 18/3, 1-16.

Perez S.I., Bernal V., Gonzalez P.N., 2006. Differences between sliding semi-landmark methods in geometric morphometrics, with an application to human craniofacial and dental variation, *Journal of Anatomy* 208, 769-784.

Pérez-Rodríguez L., Jovani R., Stevens M., 2017. Shape matters: animal colour patterns as signals of individual quality, *Proceedings Royal Society B*, 1-10.

Periverzoc F., Ilieş H.T., 2012. 3D Imaging for Hand Gesture Recognition: Exploring the Software-Hardware Interaction of Current Technologies, *3D Research* 3, 1-15.

Pintus R., Dulecha T., Jaspe A., Giachetti A., Ciortan I., Gobbetti E., 2018. Objective and Subjective Evaluation of Virtual Relighting from Reflectance Transformation Imaging Data, *EUROGRAPHICS-Workshop on Graphics and Cultural Heritage*, 87-96.

Pires H., Fonte J., Gonçalves-Seco L., Santos M.J.C., Sousa O., 2014. Morphological Residual Model. A Tool For Enhancing Epigraphic Readings of Highly Erosioned Surfaces, in: Orlandi S., Santucci R., Casarosa V., Liuzzo P.M. (eds.), *Information Technology for Epigraphy and Cultural Heritage. Proceedings of the First EAGLE International Conference*, Roma: Sapienza Università Editrice, 133-144.

Pires H., Rubio J.M., Arana A.E., 2015. Techniques for revealing 3D hidden archaeological features: morphological residual models as virtual-polynomial texture maps, *The International Archives of Photogrammetry, Remote Sensing and Spatial Information Sciences* XL-5/W4, 415-421.

Pitard G., 2006. *Métrologie et modélisation de l'aspect pour l'inspection qualité des surfaces,* PhD thesis Communauté Université Grenible Alpes (No Publisher).

Pitard G., Le Goïc G., Mansouri A., Favrelière H., Desage S.-F., Samper S., Pillet M., 2017. Discrete Modal Decomposition: a new approach for the reflectance modeling and rendering of real surfaces, *Machine Vision and Application* 28, 607-621.

Pollard A., 2018. A multispectral imaging and 3D modelling project on the Arundel Marbles, in: Kelley K., Wood R.K.L., (eds.), *Digital Imaging of Artefacts: Developments in Methods and Aims*, Summertown: Archeopress, 145-163.

Polly P.D., Motz G.J., 2016. Patterns and Processes in Morphospace: Geometric Morphometrics of three Dimensional Objects, *Virtual Palaeontology* 22, 71-99.

Porter S.T., Huber N., Hoyer C., Floss H., 2016. Portable and low-cost solutions to the imaging of Paleolithic art objects: A comparison of photogrammetry and reflectance transformation imaging, *Journal of Archaeological Science* 10, 859-863.

Pronti L., Romani M., Viviani G., Stani C., Gioia P., Cestelli-Guidi M., 2020. Advanced methods for the analysis of Roman wall paintings: elemental and molecular detection by means of synchrotron FT-IR and SEM micro-imaging spectroscopy, *Rendiconti Lincei. Scienze Fisiche e* Naturali, s.p., https://link.springer.com/article/10.1007/s12210-020-00888-9.

Prossinger H., 2005. Problems with Landmark-Based Morphometrics for Fractal Outlines: The Case of Frontal Sinus Ontogeny, in: Slice D., (ed.), *Modern Morphometrics in Physical Anthropology*, New York: Springer, 167-186.

Quattrini R., Nespeca R., Ruggeri L., 2017. Digital photogrammetry for archaeological artefacts acquisition, *IMEKO-International Conference on Metrology for Archaeology and Cultural Heritage Lecce, Italy, October 23-25,* 643-648.

Radpour R., Fischer C., Kakoulli I., 2019. New Insight into Hellenistic and Roman Cypriot Wall Paintings: An Exploration of Artists' Materials, Production Technology, and Technical Style, *Arts* 8/74, 1-33.

Reh B., Seitz C., Speck S., 2016. Seal Rotation Device – an Automated System for documenting Cylinder Seals, *FH Oberösterreich*, 27-34.

Remondino F., 2014. Photogrammetry: theory, in: Remondino F., Campana S., (eds.), *3D Recording and Modelling in Archaeology and Cultural Heritage. Theory and best practices*, Oxford: Bar Publishing, 65-73.

Reyment R.A., 2010. Morphometrics: An Historical Essay, in: Elewa A.M.T., (ed.), *Morphometrics for Nonmorphometricians*, Berlin: Springer, 9-26.

Riegert D., Konopka K., 2011. Analysis of the structure of archaeological objects-ceramic pottery, *Archives of Metallurgy and Materials* 56/1, 163-170.

Rodriguez J.M., Curtis R.V., Bartlett D.W., 2009. Surface roughness of impression materials and dental stones scanned by non-contacting laser profilometry, *Dental Materials* 25, 500-505.

Rohlf F.J., 1996. Morphometric Spaces, Shape Components and the Effects of Linear Transformations, in: Marcus L.F., Corti M., Loy A., Naylor G.J.P., Slice D.E., (eds.), *Advances in Morphometrics*, Boston: Springer, 117-130.

Rohlf F.J., 1999. Shape Statistics: Procrustes Superimpositions and Tangent Spaces, *Journal of Classification* 16, 197-223.

Rohlf F.J., Corti M., 2000. Use of Two-Block Partial Least-Squares to Study Covariation in Shape, *Systematic Biology* 49/4, 740-753.

Romanengo C., Biasotti S., Falcidieno B., 2020. Recognising decorations in archaeological finds through the analysis of characteristic curves on 3D models, *Pattern Recognition Letters* 131, 405-412.

Richtsmeier J.T., Deleon V.B., Lele S.R., 2002. The Promise of Geometric Morphometrics, *Yearbook of Physical Anthropology* 45, 63-91.

Sansoni G., Trebeschi M., Docchio F., 2009. Stat-of-The-Art and Applications of 3D Imaging Sensors in Industry, Cultural Heritage, Medicine, and Criminal Investigation, *Sensors* 9, 568-601.

Saint A.-C., Cheilakou E., Dritsa V., Koui M., Kostanti K., Christopoulou A., Zezza F., 2018. The Combined Use of Non-Invasive Methods for the Identification of Pigments and the Weathering Damage on Marble Figurines and Statues, in: Koui M., Zezza F., Kouis D., (eds.), *10h International Symposium on the Conservation of Monuments in the Mediterranean Basin. Natural and Anthropogenic Hazards and Sustainable Preservation*, Cham: Springer International Publishing AG, 233-242.

Salvemini F., Sheedy K., Olsen S.R., Avdeev M., Davis J., Luzin V., 2018. A multi-technique investigation of the incuse coinage of Magna Graecia, *Journal of Archaeological Science* 20, 748-755.

Samoun L., Fisichella T., Lingrand D., Malleus L., Precioso F., 2018. An Interactive Content-based 3D Shape Retrieval System for On-Site Cultural Heritage Analysis, *25th IEEE International Conference on Image Processing*, 1043-1047.

Santos M.J.C., Sousa O., Pires H., Fonte J., Gonçalves-Seco L., 2015. Travelling back in time to recapture old texts. The use of Morphological Residual Model (M.R.M.) for epigraphic reading: four case studies (CIL 02, 02395a, CIL 02, 02395c, CIL 02, 02476, CIL 02, 05607), in: Orlandi S., Santucci R., Casarosa V., Liuzzo P.M. (eds.), *Information Technology for Epigraphy and Cultural Heritage. Proceedings of the First EAGLE International Conference*, Roma: Sapienza Università Editrice, 437-454.

Santosh K.C., (ed.), 2018. *Document Image Analysis. Current Trends and Challenges in Graphics Recognition*, Singapore: Springer Nature.

Sarri D., Athanassopoulos E.F., 2020. 3D Modeling Applications to Terracotta Figurines from Plakomenos Greece, in: Kremers H., (ed.), *Digital Cultural Heritage*, Cham: Springer Nature Switzerland, 169-182.

Sbroscia M., Cestelli-Guidi M., Colao F., Falzone S., Gioia C., Gioia P., Marconi C., Mirabile Gattia D., Loreti E.M., Marinelli M., Missori M., Persia F., Pronti L., Romani

M., Sodo A., Verona-Rinati G., Ricci M.A., Fantoni R., 2020. Multi-analytical non-destructive investigation of pictorial apparatuses of "Villa della Piscina" in Rome, *Microchemical Journal* 153, 1-10.

Scafuri M.P., Rennison B., 2016. Scanning the *H.L. Hunley*: Employing a structured-light scanning system in the archaeological documentation of a unique maritime artifact, *Journal of Archeological Science* 6, 302-309.

Schindler K., Grabner M., Leberl F., 2008. Fast on-site reconstruction and visualization of archaeological finds, in: Altan M.O., (ed.), *New perspectives to save cultural heritage. Proceedings of the 19th international symposium CIPA, September 30 – October 4, 2003*, Istanbul: SIPA, 463-468.

Scudieri F., Mercuri F., Volterri R., 2001. Non-invasive analysis of artistic heritage and archaeological finding by time resolved IR thermography, *Journal of Thermal Analysis and Calorimetry* 66, 307-314.

Selden Jr. R.Z., Perttula T.K., O'Brien M.J., 2014. Advances in Documentation, Digital Curation, Virtual Exhibition, and a Test of 3D Geometric Morphometrics. A Case Study of the Vanderpool Vessels from the Ancestral Caddo Territory, *Advances in Archaeological Practice: A Journal of the Society for American Archaeology* 2/2, 64-79.

Sels S., Verspeek S., Ribbens B., Bogaerts B., Vanlanduit S., Penne R., Steenackers G., 2019. A CAD matching method for 3D thermography of complex objects, *Infrared Physics and Technology* 99, 152-157.

Sfarra S., Ambrosini D., Paoletti A., Paoletti D., Ibarra-Castanedo C., Bendada A.H., Maldague X.P.V., 2010. Quantitative Infrared Thermography (IRT) and Holographic Interferometry (HI): Nondestructive Testing (NDT) for defects detection in the Silicate Ceramics Industry, *Advances in Science and Technology* 68, 102-107.

Sfarra S., Ibarra-Castanedo C., Ambrosini D., Paoletti D., Bendada A., Maldague X., 2014b. Non-Destructive Testing Techniques to Help the Restoration of Frescoes, *Arabian Journal of Science & engineering* 39, 3461-3480.

Sfarra S., Theodorakeas P., Černecký J., Pivarčiová E., Perilli S., Koui M., 2017. Inspecting Marquetries at Different Wavelengths: The Preliminary Numerical Approach as Aid for a Wide-Range of Non-destructive Tests, *Journal of Nondestructive Evaluation* 36/6, 1-20.

Shanoer M.M., Abed F.M., 2018. Evaluate 3D laser point clouds registration for cultural heritage documentation, *The Egyptian Journal of Remote Sensing and Space Sciences* 21, 295-304.

Sirikham A., Zhao Y., Liu H., Xu Y., Williams S., Mehnen J., 2020. Three-dimensional subsurface defect shape reconstruction and visualization by pulsed thermography, *Infrared Physics and Technology* 104, 1-10.

Slice D., 2005. Modern Morphometrics in: Slice D., (ed.), *Modern Morphometrics in Physical Anthropology*, New York: Kluwer Academic/Plenum Publishers, 1-46.

Slice D., 2007. Geometric Morphometrics, *Annual Review of Anthropology* 36, 261-281.

Song K., Hu S., Wen X., Yan Y., 2016. Fast 3D shape measurement using Fourier transform profilometry without phase unwrapping, *Optics and Lasers in Engineering* 84, 74-81.

Spangher A., Visintini D., Tucci G., Bonora V., 2017. Geomatic 3D modeling of a statue (also) for structural analysis and risk evaluation: the example of San Giovannino Martelli in Florence, *The International Archives of the Photogrammetry, Remote Sensing and Spatial Information Sciences* XLII-5/W1, 61-68.

Starbuck J.M., 2014. Quantitative Evaluation of the Facial Morphology of a Tolteca Figurine from Mexico using Geometric Morphometric Approaches, *International Journal of Morphology* 32/2, 499-509.

Stemp W.J., Lerner H.J., Kristant E.H., 2018. Testing area-scale fractal complexity (Asfc) and laser scanning confocal microscopy (LSCM) to document and discriminate microwear on experimental quartzite scrapers, *Archaeometry* 60/4, 660-677.

Stemp W.J., Macdonald D.A., Gleason M.A., 2019. Testing imaging confocal microscopy, laser scanning confocal microscopy, and focus variation microscopy for microscale measurement of edge cross-sections and calculation of edge curvature on stone tools: Preliminary results, *Journal of Archaeological Science* 24, 513-525.

Stemp W.J., Stemp M., 2001. UBM Laser Profilometry and Lithic Use-Wear Analysis: A Variable Length Scale Investigation of Surface Topography, *Journal of Archaeological Science* 28, 81-88.

Stivanello M.E., Stemmer M.R., 2019. Combining Stereo and Fourier Transform Profilometry for 3D Scanning in Dynamic Environments, *Journal of Control, Automation and Electrical Systems* 30, 688-699.

Su X., Zhang Q., 2010. Dynamic 3-D shape measurement method: A review, *Optics and Lasers in Engineering* 48, 191-204.

Szzentmiklósi L., Maróti B., Kis Z., Kasztovszky Z., 2018. Integration of neutron-based elemental analysis and imaging methods and applications to cultural heritage research, *Journal of Archaeological Science* 20, 476-482.

Szilágyi V., Kis Z., Szentmiklósi L., 2016. Neutron Imaging for Archaeometry, *Archeimetrial Muhely* 13/3, 157-172.

Tatsuta H., Takahashi K.H., Sakamaki Y., 2018. Geometric morphometrics in entomology: Basics and applications, *Entomological Science* 21, 164-184.

Tavukçuoğlu A., Caner-Saltik E.N., Akoğlu K.G., Işikoğlu M., Caner E., 2011. In Situ Examination of Nemrut Dağ Sandstone and Limestone Statues by NDT Methods, *Congrès SFIIC "Jardins de Pierres"*, 204-213.

Tavukçuoğlu A., 2018. Non-Destructive Testing for Building Diagnostics and Monitoring: Experience Achieved with Case Studies, *MATEC-Web of Conference* 149, 1-8.

Tokovinine A., Estrada Belli F., 2017. From stucco to digital: Topometric documentation of Classic Maya facades at Homul, *Digital Applications in Archaeology and Cultural Heritage* 6, 18-28.

Torrente M., Biasotti S., Falcidieno B., 2016. Feature curve identification in archaeological fragments using an extension of the Hough transform, *IMATI* 16/9, 1-19.

Townsend A., Senin N., Blunt L., Leach R.K., Taylor J.S., 2016. Surface texture metrology for metal additive manufacturing: a review, *Precision Engineering* 46, 34-47.

Triolo P.A.M., Spingardi M., Costa G.A., Locardi F., 2019. Practical application of visible-induced luminescence and use of parasitic IR reflectance as relative spatial reference in Egyptian artifacts, *Archaeological and Anthropological Sciences* 11, 5001-5008.

Tsatsouli K., Nikolaou E., 2017. The ancient Demetrias figurines: new insights on pigments and decoration techniques used on Hellenistic clay figurines, *Science é Technologyy of Archaeological Research* 3/2, 341-357.

Vargiolu R., Zahouani H., Blot J.-Y., 2005. Analyse de la topography des pièces de monnaie du San Pedro de Alcantara, *Revista Portuguesa de Argqueologia* 8/1, 433-458.

Van der Perre A., Hameeuw H., Boschloos V., Delvaux L., Proesmans M., Vandermeulen B., Van Gool L., Watteeuw L., 2016. Toward a combined use of IR, UV and 3D-imaging for the study of small inscribed and illuminated artefacts, in: Homem P.D., (ed.), *Lights On… Cultural Heritage and Museums!,* Porto: U.Porto, 163-192.

Verhoeven G., 2018. Multispectral and Hyperspectral Imaging, in: López Varela S., (ed.), *The encyclopedia of archaeological sciences*, Hoboken: John Wiley & Sons, 1-4.

Vogl C., 1993. Theoretical enhancements of finite-element scaling analysis (FESA) methodology, *Systematic Biology* 42/3, 341-355.

Wang Z., 2020. Review of real-time three-dimensional shape measurement techniques, *Measurement* 156, 2-15.

Watteeuw L., Hameeuw H., Vandermeulen B., Van der Perre A., Boschloos V., Delvaux L., Proesmans M., Van Bos M., Van Gool L., 2016. Light, shadows and surface characteristics: the multispectral Portable Light Dome, *Applied Physics A* 122/976, 1-7.

Webb E.K., 2017. Reflected infrared and 3D imaging for object documentation, *Journal of the American Institute for Conservation*, 1-14.

Wen C.-M., Sfarra S., Gargiulo G., Yao Y., 2019. Edge-Group Sparse Principal Component Thermography for Defect Detection in an Ancient Marquetry Sample, *Proceedings* 27/34, 1-5.

Willomitzer F., (ed.) 2019. *Single-Shot 3D Sensing Close to Physical Limits and Information Limits*, Doctoral thesis University Erlagen-Nürnberg, Switzerland: Springer Nature.

Winemiller T.L., Ochoa-Winemiller V., Ludwig J., 2018. Assessing surface correspondence and trade of Maya figurines and moulds using multi-stripe laser technology and metrology, *Archaeometry* 60, 1002-1017.

White A.J.R., Sun H., Swanson W.H., Lee B.B., 2002. An Examination of Physiological Mechanisms Underlying the Frequency-Doubling Illusion, *Investigative ophthalmology & Visual Science* 43/11, 3590-3599.

Wu Y.-C., Cao Y.-P., Huang Z.-F., Lu M.-T., Chen D.-L., 2012. Improved composite Fourier transform profilometry, *Optics & Laser Technology* 44, 2037-2042.

Yao Y., Sfarra S., Lag[uela S., Ibarra-Castanedo C., Wu J.-Y., Maldague X.P.V., Ambrosini D., 2018. Active thermography testing and data analysis for the state of conservation of panel paintings, *International Journal of Thermal sciences* 126, 143-151.

Yousefi B., Sfarra S., Ibarra-Castanedo C., Maldague X.P.V., 2017. Comparative analysis on thermal non-destructive testing imagery applying Candid Covariance-Free Incremental Principal Component Thermography (CCIPCT), *Infrared Physics & Technology* 85, 163-169.

Zányi E., Schroer C., Mudge M., Chalmers A., 2007. Lighting and Byzantine glass tesserae, *EVA Londen Conference*, 22.1-22.8.

Zhang H., Sfarra S., Osman A., Ibarra-Castanedo, Maldague X.P.V., 2019. Robotized Line-Scan Thermographic Mid-Wave Infrared Vision for Artwork Inspection: A Study on Famous Mock-Ups, in: Osman A., Moropoulou A., (eds.), *Nondestructive Evaluation and Monitoring Technologies, Documentation*, Diagnosis and Preservation of Cultural Heritage, Cham: Springer Nature Switzerland, 64-74.

Zhang L., João da Fonseca M., Ferreira A., 2004. Survey on 3D Shape Descriptors, *DecorAR*, 1-28.

Živčák J., Madarász L., Hudák R., Rudas I.J., (eds.), 2013. *Methodology, Models and Algorithms in Thermographic Diagnostics*, Springer: Heidelberg.

Zuo C., Feng S., Huang L., Tao T., Yin W., Chen Q., 2018. Phase shifting algorithms for fringe projection profilometry: A review, *Optics and Lasers in Engineering* 109, 23-59.

Internet:

Cox Thermal imaging cameras 2015. *Infrared Thermography*, Consulted on 12 February 2020 with http://coxcamera.com/technology/infrared-thermography/.

Cultural Heritage Imaging 2020. *Reflectance transformation imaging (RTI)*, Consulted on 22 April 2020 with http://culturalheritageimaging.org/Technologies/RTI/.

Fischer H., 2019. *X-Ray Fluorescence Spectroscpy (XRF)-Basics,* Consulted on 7 May 2020 with https://xrf-spectroscopy.com/.

Föll H., 2015. *Types of Luminescence*, Consulted on 22 May 2020 with https://www.tf.uni-kiel.de/matwis/amat/admat_en/index.html.

Konstantakopoulos Y., 2002. *Wavelength*, Consulted on 4 May 2020 with http://light.physics.auth.gr/enc/wavelength_en.html.

Lumen Learning 2017. *Trigonometric Functions and the Unit Circle*, Consulted on 16 May 2020 with https://courses.lumenlearning.com/boundless-algebra/chapter/trigonometric-functions-and-the-unit-circle/.

MathWorks 2020, *Train Deep Learning Network to Classify New Images*, Consulted on 24 May 2020 with https://www.mathworks.com/help/deeplearning/ug/train-deep-learning-network-to-classify-new-images.html.

Pierce R., 2018. *Graphs of Sine, Cosine and Tangent*, Consulted on 13 May 2020 with https://www.mathsisfun.com/algebra/trig-sin-cos-tan-graphs.html.

Pohl H., 2019. *What is the difference between fluorescence, phosphorescence and luminescence?*, Consulted on 4 May 2020 with https://www.enzolifesciences.com/sciencecenter/technotes/2019/december/what-is-the-difference-between-fluorescence-phosphorescence-and-luminescence?/.

Zaboli M., 2019. *Reflection, Refraction, Diffraction and Absorption*, Consulted on 4 May 2020 with http://packetassurance.com/reflection-refraction-diffraction-and-absorption/.

Zygo Corporation 2018. *MX™ Surface Texture Parameters*, Consulted on 5 February 2020 with https://www.zygo.com/?/mailer/SurfaceTextureParametersHandbook.htm.

X. Attachments

1. Summary table

	Scientific techniques				
	Two-point registration	**Procrustes superimposition**	**Generalized resistant-fit**	**Finite-element scaling analysis**	**Thin-plate splines**
Material	All kind	All kind	All kind	All kind	All kind
Type of information	Geometry	Geometry	Geometry	Geometry	Geometry
Sample and size	Images + object	Images + object	Images + object	Images + object	Images + object
Contact - destructive	Non-contact Non-destructive	Non-contact Non-destructive	Non-contact Non-destructive	Non-contact Non-destructive	Non-contact Non-destructive
Theoretical background	Easy	Difficult	Easy	Difficult	Easy
Data-processing	Easy	Moderate	Easy (no need for statistical analysis)	Moderate	Moderate
Ability of measuring complex shapes	Bad (only three points)	Medium	Bad (works with mean values)	Medium	Medium
Accuracy	- Low (only one point used as variable) - images = deformation	- Medium (improved with sliding landmarks) - images = deformation	- Low - images = deformation	- Medium - images = deformation	Medium
Overall Duration	Dependent on processing time	Dependent on processing time and number of landmarks	Dependent on processing time	Dependent on processing time	Dependent on processing time

Safety	Good	Good	Good	Good	Good
Cost (equipment-software)	Low (free software)	Low (free software) GPU (from €1000)	Low (free software)	Low (free software) GPU (from €1000)	Low (free software) GPU (from €1000)
Software accessibility	https://life.bio.sunysb.edu/morph/	https://life.bio.sunysb.edu/morph/	https://life.bio.sunysb.edu/morph/	https://life.bio.sunysb.edu/morph/	https://life.bio.sunysb.edu/morph/
Apparatus	Computer	Computer	Computer	Computer	Computer
Compatibility with other techniques	Yes	Yes	Yes	Yes	Yes

	Scientific techniques				
	Euclidian distance matrix	**Fourier analysis**	**Eigenshape analysis**	**Box-counting method**	**Shape descriptor**
Material	All kind	All kind	All kind	All kind	All kind
Type of information	Geometry	Geometry	Geometry	Geometry	Geometry
Sample and size	Images + object	Images + object	Images + object	Images + object	Images or 3D models
Contact - destructive	Non-contact Non-destructive	Non-contact Non-destructive	Non-contact Non-destructive	Non-contact Non-destructive	Non-contact Non-destructive
Theoretical background	Difficult	Easy	Easy	Easy	Difficult
Data-processing	Moderate	Moderate	Moderate	Easy	Difficult
Ability of measuring complex shapes	Bad	Good	Good	Good	Good
Accuracy	- Medium - images = deformation	- High - Images = deformation	- High - Images = deformation	Medium	High
Overall Duration	Dependent on processing time	Dependent on processing time and number of landmarks	Dependent on processing time	Dependent on processing time	Dependent on processing time
Safety	Good	Good	Good	Good	Good
Cost (equipment-software)	Low (free software)	Low (free software) GPU (from €1000)	Low (free software) GPU (from€1000)	Low (free software)	GPU (from €1000)
Software accessibility	https://life.bio.sunysb.edu/morph/	https://life.bio.sunysb.edu/morph/	https://life.bio.sunysb.edu/morph/	https://life.bio.sunysb.edu/morph/	

Apparatus	Computer	Computer	Computer	Computer	Computer
Compatibility with other techniques	Yes	Yes	Yes	Yes	Yes

	Scientific techniques				
	Machine learning	**IRT**	**Photogrammetry**	**Laser scanning**	**Structured light**
Material	All kind	All kind	Problems with high reflective or dark surface	Problems with high reflective or dark surface	Problems with high reflective or dark surface
Type of information	Geometry + texture + colour	Geometry	Geometry + texture + colour	Geometry + texture	Geometry + texture + colour
Sample and size	Images + object	Object	Images	Object	Object
Contact - destructive	Non-contact Non-destructive	Non-contact and non-destructive	Non-contact and non-destructive	Non-contact and non-destructive	Non-contact and non-destructive
Theoretical background	Difficult	Medium	Easy	Easy	Easy
Data-processing	Difficult	Medium	Difficult	Medium	Medium
Ability of measuring complex shapes	High	High	Medium	High	High
Accuracy	High	High (millimetre)	High (micrometre)	High (micrometre)	High (micrometre)
Overall Duration	Training = days to months After = hours	150 Hz per frame rate	Images: fast Processing: hours to days	Images: hours Processing: fast	Images: fast Processing: hours to days
Safety	Good	High temperature = bad sample	Good	Good	Good
Cost (equipment-software)	High GPU (from €1000)	Camera: > €3000 Software: free (basic) > €3000	Camera: > €500 Software: free (Visual SFM) or license (> $180, Agisoft Photoscan)	Scanner: > €3000 Software: > €1000	Scanner: >€3000 Software: open source or licence

Software accessibility		https://software.labir.eu/	https://www.agisoft.com/	http://www.nextengine.com/products	https://www.opensourceimaging.org/project/structured-light-3d-scanner/
Apparatus	Computer	dSLR (IR camera) + lights	dSLR camera	NextEngine 3D	SmartSCAN
Compatibility with other techniques	Yes	Not specificly	Yes	Yes	Yes

	Scientific techniques			
	Profilometry	**RTI**	**Tomography**	**Multi-and hyper spectral imaging**
Material	All kind	All kind	All kind	Painted objects
Type of information	Geometry + texture	Geometry + texture + colour	Geometry	Colour
Sample and size	Object or model	Images or model	Object	Object
Contact - destructive	Non-contact and Non-destructive	Non-contact and non-destructive	Non-contact and non-destructive	Non-contact and non-destructive
Theoretical background	Medium	Medium	Easy	Easy
Data-processing	Medium	Medium	Medium	NA
Ability of measuring complex shapes	High	High	High	High
Accuracy	High (micrometre)	High	High (submillimetre)	High
Overall Duration	images: 1000 measures per second processing: hours	Images: fast Processing: hour	Images: fast Processing: hour	Images: fast
Safety	Good	Good	Good	Good

Cost (equipment-software)	Microscope: > €5000 Software: licence	Camera: > €500 Software: free	Scanner: > €35 000 Free software	Camera: > €500 Scope: > €11 000
Software accessibility	https://www.digitalsurf.com/software-solutions/profilometry/	http://culturalheritageimaging.org/What_We_Offer/Downloads/	http://www.neutronoptics.com/muhrec.html	
Apparatus	Profilometer	dSLR camera	Scanner	dSLR camera + filters or lights
Compatibility with other techniques	Yes	Yes	Not specifically	Yes